UNIVERSITY OF CALIFORNIA

Los Angeles

Acceleration of Electrons using Relativistic Plasma Waves

A dissertation submitted in partial satisfaction

of the requirements for the degree
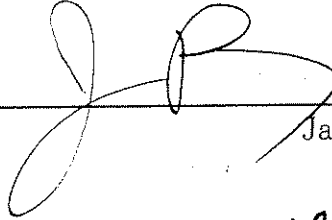
Doctor of Philosophy in Electrical Engineering
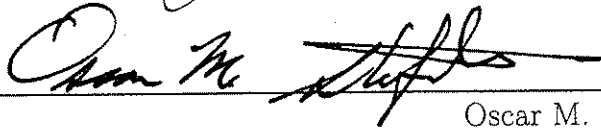
by

Ritesh Narang

2003

The dissertation of Ritesh Narang is approved.
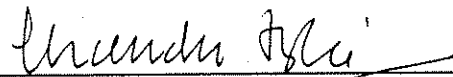
_____
James Rosenzweig

_____
Oscar M. Stafsudd

_____
Warren B. Mori

_____
Chan Joshi, Committee Chair

University of California, Los Angeles

2003

DEDICATION

For my parents, Raj and Gian.

For my sisters, Ektaa and Tina.

For my love, Rashmi.

TABLE OF CONTENTS

LIST OF FIGURES

xi

LIST OF TABLES

ACKNOWLEDGMENTS

VITA

Sep. 23, 1973   Born, Chandigarh, Punjab, India.

1995   B.S., Physics, University of California, Los Angeles.

1998   M.S., Electrical Engineering, University of California,
                 Los Angeles.

1995–2003   Graduate Student Researcher, Electrical Engineering
                 Department, University of California, Los Angeles.

PUBLICATIONS AND PRESENTATIONS

R. Narang, F. S. Tsung, C. Joshi, W. B. Mori, R. A. Fonseca, and L. O. Silva, "2-D Simulations on the Acceleration of Electrons in Preformed Plasma Channels," submitted to Phys. Rev. ST-AB.

F. S. Tsung, R. Narang, C. Joshi, W. B. Mori, R. A. Fonseca, and L. O. Silva, "Near GeV Energy Laser Wakefield Acceleration of Self-Trapped Electrons in a Plasma Channel," submitted to Phys. Rev. Lett.

C. V. Filip, R. Narang, S. Ya. Tochitsky, C. E. Clayton, P. Musumeci, R. B. Yoder, K. A. Marsh, J. B. Rosenzweig, C. Pellegrini, and C. Joshi, "Non-resonant beat-wave excitation of constant phase-velocity, relativistic plasma waves for charged-particle acceleration," submitted to Phys. Rev. E.

S. Ya. Tochitsky, R. Narang, C. V. Filip, C. E. Clayton, P. Musumeci, R. B. Yoder, K. A. Marsh, J. B. Rosenzweig, C. Pellegrini, and C. Joshi, "Enhanced Acceleration of Injected Electrons by Laser Beatwave in a Self-Induced Ion Channel," submitted to Phys. Rev. Lett.

C. V. Filip, S. Ya. Tochitsky, R. Narang, C. E. Clayton, K. A. Marsh, and C. Joshi, "Collinear Thomson scattering diagnostic system for the detection of relativistic waves in low-density plasmas," Rev. of Sci. Inst., **74**, (no.7), July 2003: 3576–78.

S. Ya. Tochitsky, R. Narang, C. V. Filip, C. E. Clayton, P. Musumeci, R. B. Yoder, K. A. Marsh, J. B. Rosenzweig, C. Pellegrini, and C. Joshi, "Acceleration of Injected Electrons in a laser Beatwave Experiment," Proceedings of the 2003 Particle Accelerator Conference, Portland, OR, USA, May 12–16, 2003.

R. Narang, F. S. Tsung, D. F. Gordon, C.Joshi, W. B. Mori, R. A. Fonseca, and L. O. Silva, "2-D and 3-D PIC Simulations of Laser Guiding and Wake-Field Acceleration of Electrons to GeV levels in a Preformed Plasma Channel," paper presented at the 2002 American Physical Society, Division of Plasma Physics, Orlando, FL, USA, November 2002.

R. Narang, F. S. Tsung, D. F. Gordon, C.Joshi, and W. B. Mori, "Guiding of a Multi-Terawatt Femtosecond Laser Pulse through a Preformed Plasma Channel," paper presented at the 32nd Anomalous Absorption Conference, Turtle Bay, Oahu, HI, USA, July 21–26, 2002.

R. Narang, C. V. Filip, S. Ya. Tochitsky, D. F. Gordon, C. E.Clayton, C. Joshi, and W. B. Mori, "Simulations on Beat-wave Excitation of Plasma Waves," paper presented at the 32nd Anomalous Absorption Conference, Turtle Bay, Oahu, HI, USA, July 21–26, 2002.

R. Narang, C. E. Clayton, C. V. Filip, S. Ya. Tochitsky, D. F. Gordon, C. Joshi, and W. B. Mori, "PIC Simulations of Plasma Beat-Wave Acceleration Experiments at UCLA," American Institute Physics Conference Proceedings, no. 647, 2002, p. 213–18. USA.

R. Narang, F. S. Tsung, D. F. Gordon, C.Joshi, and W. B. Mori, "Guiding of a Multi-Terawatt Femtosecond Laser Pulse through a Preformed Plasma Channel," paper presented at the 2002 Advanced Accelerator Concepts Workshop, Oxnard, CA, USA, June 23–28, 2002.

C. V. Filip, S. Y. Tochitsky, R. Narang, C. E. Clayton, K. A. Marsh, C. Joshi, "Interpretation of resonant and non-resonant beat-wave excitation: experiments and simulations, " American Institute of Physics Conference Proceedings, no. 647, 2002, p. 770–85. USA.

C. V. Filip, R. Narang, S. Ya. Tochitsky, C. E. Clayton, K. A. Marsh, and C. Joshi, "Optical Kerr switching technique for the production of a picosecond, multiwavelength CO_2 laser pulse," Applied Optics, June 20, 2002, **41**, (no.18):3743–47.

R. Narang, C. V. Filip, S. Ya. Tochitsky, D. F. Gordon, C. E. Clayton, K. A. Marsh, and C. Joshi, "Characteristics of plasmas produced by double beat

wave interaction in the Neptune facility at UCLA, Proceedings of the 2001 Particle Accelerator Conference, IEEE, vol.5, 2001, p. 3996–98, Piscataway, NJ, USA.

R. Narang, C. V. Filip, S. Ya. Tochitsky, C. E. Clayton, and C. Joshi, "A Subharmonic Instability in a Beat Wave Excited Plasma," paper presented at the 21st ICFA Beam Dynamics Workshop on Laser-Beam Interactions, SUNY, Stony Brook, NY, USA, June 11–15, 2001.

S. Ya. Tochitsky, C. V. Filip, R. Narang, C. E. Clayton, K. A. Marsh, and C. Joshi, "Efficient shortening of self-chirped picosecond pulses in a high-power CO_2 amplifier," Optics Letters **26**, 11, p. 813 (2001).

S. Ya. Tochitsky, C. V. Filip, R. Narang, C. E. Clayton, K. A. Marsh, and C. Joshi, "Present status and future prospects of high-power CO_2 laser research," Proceedings of the International Conference on LASERS 2000, STS Press, 2001, p.417–24, McLean, VA, USA.

H. Suk, C. E. Clayton, C. Joshi, T. C. Katsouleas, P. Muggli, R. Narang, C. Pellegrini, and J. B. Rosenzweig, "Plasma source test and simulation results for the underdense plasma lens experiment at the UCLA Neptune Laboratory," IEEE Transactions on Plasma Science, Feb. 2000, vol.28, (no.1):271–77.

S. Ya. Tochitsky, R. Narang, C. V. Filip, B. Blue, C. E. Clayton, K. A. Marsh, and C. Joshi, "Amplification of two-wavelength CO_2 laser pulses to terawatt level," Proceedings of the International Conference on LASERS '99, STS Press, 2000, p. 265–72, McLean, VA, USA.

S. Ya. Tochitsky, R. Narang, C. V. Filip, C. E. Clayton, K. A. Marsh, and C. Joshi, "Generation of 160-ps terawatt-power CO_2 laser pulses," Optics Letters, Dec. 1, 1999, vol.24, (no.23):1717–19.

H. Suk, C. E. Clayton, G. Hairapetian, C. Joshi, M. Loh, P. Muggli, R. Narang, C. Pellegrini, J. B. Rosenzweig, and T. C. Katsouleas, "Underdense plasma lens experiment at the UCLA Neptune Laboratory," Proceedings of the 1999 Particle Accelerator Conference, IEEE, 1999, vol. 5, p. 3708–10, Piscataway, NJ, USA.

R. Narang, S. Ya. Tochitsky, C. E. Clayton, C. V. Filip, and C. Joshi, "Production of picosecond 10.6 μm and 10.3 μm pulses using semiconductor switching," paper presented at the 1998 Advanced Accelerator Concepts, Eighth Workshop, Baltimore, MD, USA, July 6–11, 1998.

H. Suk, C. E. Clayton, R. Narang, P. Muggli, J. B. Rosenzweig, C. Pellegrini, and C. Joshi, "Test results of the plasma source for underdense plasma lens experiments at the UCLA Neptune Lab," Proceedings of the 1998 Advanced Accelerator Concepts, Eighth Workshop, Baltimore, MD, USA, July 6–11, 1998.

Acceleration of Electrons using Relativistic Plasma Waves

by

Ritesh Narang

Doctor of Philosophy in Electrical Engineering

University of California, Los Angeles, 2003

Professor Chan Joshi, Chair

The plasma beat-wave accelerator in the Neptune Laboratory at UCLA uses a $\sim$1 terawatt two-wavelength CO_2 laser pulse to tunnel ionize hydrogen gas at conditions of resonance for driving a relativistic plasma wave. This plasma wave is used as an accelerating structure for an externally injected, $\sim$12 MeV, electron beam from the Neptune Photo-injector. The accelerated electron energy spectrum is measured using an electron spectrometer, consisting of a dipole magnet, and an array of surface barrier detectors and phosphors. Accelerated electrons have been detected out to $\sim$50 MeV using this setup. These experiments are also modeled in 2-D particle-in-cell simulations. These simulations show the self-channeling of the laser beam due to ion motion, which overcomes the defocusing caused by ionization induced refraction, effectively increasing the interaction length between the injected electrons and the plasma wave. Simulations are also performed to study the guiding of shorter (50–500 fs), but more intense, 0.8 μm laser pulses by preformed plasma channels. The three laser acceleration schemes, laser wake-field acceleration, plasma beat-wave acceleration, and self-modulated laser wake-field acceleration, are explored.

CHAPTER 1

Introduction

The laser acceleration of charged particles in plasmas, first discussed by Tajima and Dawson [1], has inspired numerous experimental, theoretical, and computational investigations [2, 3, 4]. The goal of these studies has been to develop plasma-based particle accelerators that utilize the large electric fields produced in laser induced relativistic plasma waves. Conventional RF technology is, at best, able to provide accelerating gradients ~ 150 MeV/m (CTF3, CERN) thereby necessitating accelerators that are sometimes kilometers in length to reach the desired energy levels. Large amplitude relativistic plasma waves provide a means of accelerating particles with gradients as large as 100 GeV/m. In general, the maximum longitudinal electric field attainable by a plasma wave is $E_L \simeq 0.96\sqrt{n_0}$ V/cm, where n_0 is the plasma density in cm^{-3}. This means that for a plasma density of 10^{16} cm^{-3} an accelerating gradient of ~ 10 GeV/cm could be achieved.

In this dissertation, experimental results from the plasma beat-wave acceleration (PBWA) of electrons in the Neptune Laboratory for Advanced Accelerator Research will be the primary subject of discussion. The beat-wave excitation of plasma waves, by a two-wavelength laser pulse, will be discussed in detail later in this chapter. In Chapter 2, the laser system and experimental apparatus will be described and in the subsequent chapters analysis of the electron acceleration experiments will be presented. This work is related to past PBWA experiments in the MARS Laboratory at UCLA [5], but has improved upon a variety

1

of important experimental apparatus, especially key laser and injected electron beam parameters. Modeling of the laboratory parameters through particle-in-cell (PIC) simulations will be discussed and compared to PBWA experimental results in Chapters 4 and 5. In the last chapter, PIC simulations of laser acceleration schemes in preformed plasma channels will be analyzed. That chapter will discuss guiding and electron acceleration in preformed plasma channels for three different acceleration schemes. Chapter 6 contains a summary of the main findings of this thesis.

1.1 Plasma Wave Excitation

Electron plasma waves, also called Langmuir waves, are electrostatic space charge waves where a disturbance causes plasma electrons to oscillate at the plasma frequency. In a cold plasma, these waves have a dispersion relation of $\omega = \omega_p$, where ω_p is $(4\pi n_0 e^2/m)^{1/2}$. These waves are termed relativistic when the oscillations have a phase velocity near the speed of light and have a wave vector given by $k_p = \omega_p/c$. To excite plasma waves it is necessary to create a plasma density perturbation, δn, that has a periodicity which is an integer multiple of $2\pi\omega_p^{-1}$. Associated with this density modulation is a longitudinal electric field that can be used to accelerate particles and has a normalized amplitude given by $\varepsilon_L = \delta n/n_0 = eE_L/mc\omega_p$. Such longitudinal plasma oscillations associated with these density modulations can be excited through the ponderomotive force of a laser pulse,

$$\mathbf{F}_p = -\frac{\omega_p^2}{\omega^2}\nabla\frac{<\mathbf{E}^2>}{8\pi},\tag{1.1}$$

where ω is the laser frequency (or the beat frequency), and $\mathbf{E}$ is the electric field of the laser pulse. The ponderomotive force can be thought of as the gradient of

2

(1) Beat-wave Acceleration (PBWA) Ultra-short laser pulse (LWFA)

Raman scattering of an intense laser pulse (SMLWFA)
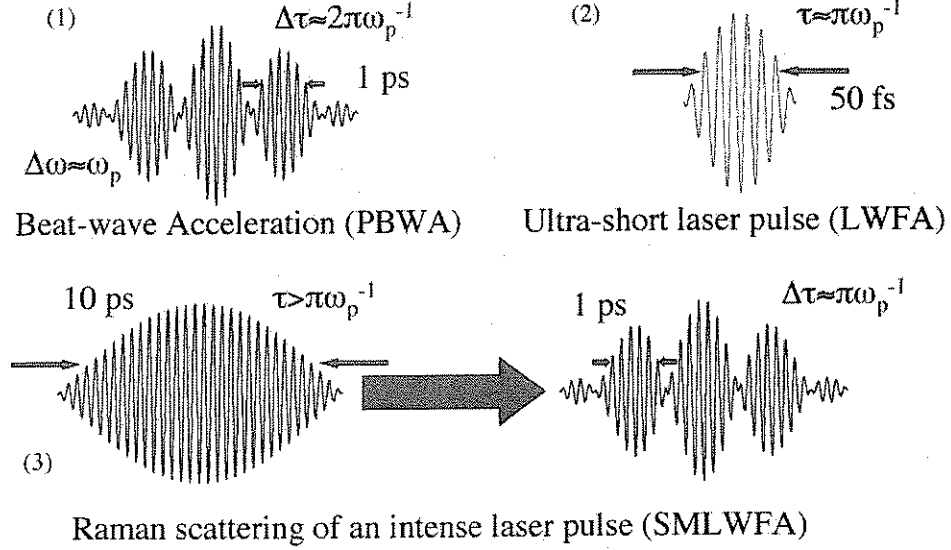
Figure 1.1: Methods of exciting relativistic electron plasma waves using lasers

the light pressure on the plasma, and is a nonlinear force that comes from the $E \times B$ term in the Lorentz force equation [6], where B is the magnetic field of the laser pulse.

There are three primary methods of exciting relativistic electron plasma waves using lasers: (1) beat-wave excitation (PBWA) in which a two-frequency (ω_1, ω_2) laser pulse has a frequency separation $\Delta\omega = \omega_2 - \omega_1 \approx \omega_p$ with a corresponding beat period $\Delta\tau \approx 2\pi\omega_p^{-1}$; (2) resonant laser wake-field excitation (LWFA) where the laser pulse duration is approximately half a plasma period, $\pi\omega_p^{-1}$; and (3) Raman forward scattering of an intense laser pulse (SMLWFA) which self-modulates the intensity of the laser pulse by generating sideband frequencies shifted from the initial laser frequency by $\pm n\omega_p$. Figure 1.1 depicts all three of these excitation schemes. For all of these methods the phase velocity of the plasma waves, v_ϕ, is equal to the group velocity of light in the plasma, v_g^{em},

$$v_\phi = \frac{\omega_p}{k_p} = v_g^{em} = c\left(1 - \frac{\omega_p^2}{\omega^2}\right)^{1/2};$$ (1.2)

3

the dispersion relation for light in a plasma is $\omega^2 = \omega_p^2 + c^2k^2$, where $k = 2\pi/\lambda$ is the laser wave-number and λ is the laser wavelength. The plasma wave relativistic factor $\gamma_\phi = (1 - \frac{v_\phi^2}{c^2})^{-1/2} = \omega/\omega_p$. The value of γ_ϕ is what determines the necessary energy that a particle must have to be trapped and accelerated in phase with the plasma wave. For the experiments that will be discussed later $\gamma_\phi \approx 32$ corresponding to an electron energy of ~16 MeV. Trapped particles in the accelerating phase of the wave have an increasing γ and eventually dephase over a distance related to the mismatch between the velocities of the particles and the wave structure. This dephasing length is given by the expression $L_{deph} = \lambda_p^3/\lambda^2$ [7] where λ_p is the plasma wavelength; the dephasing length is equal to ~40 cm for the PBWA in the Neptune Laboratory and is not a limiting factor in the acceleration process over a 2.5 cm distance.

The maximum amplitude of the longitudinal electric field of the plasma wave is determined by Gauss's Law to be $\varepsilon_0 \cong mc\omega_p/e$. This is known as the cold wave-breaking amplitude, and is the plasma wave amplitude at which electrons in a cold plasma ($v_{th} \approx 0$) move a distance greater than $\lambda_p/2\pi$ over a time equal to one plasma period τ. In general the larger the wave amplitude the more nonlinear effects become important and become apparent in the steepening of waves that approach the $mc\omega_p/e$ amplitude. The sinusoidal oscillations with $\delta n/n_0 = 5\%$ (linear regime) for Figure 1.2(a) and $\delta n/n_0 = 30\%$ (nonlinear regime) for Figure 1.2(b) demonstrate this steepening of the plasma waves. For highly nonlinear oscillations the electrons in the plasma wave can move at relativistic velocities so the maximum wave amplitude attainable becomes $\varepsilon_0^{rel} \cong \frac{mc\omega_p}{e}\sqrt{2}(\gamma_\phi - 1)^{1/2}$. In addition, due to the relativistic increase in the electron mass, there is a nonlinear frequency shift [8] for the plasma wave frequency,

$$\Delta\omega = -\frac{3}{16}\left(\frac{eE}{mc\omega_p}\right)^2 \omega_p \tag{1.3}$$
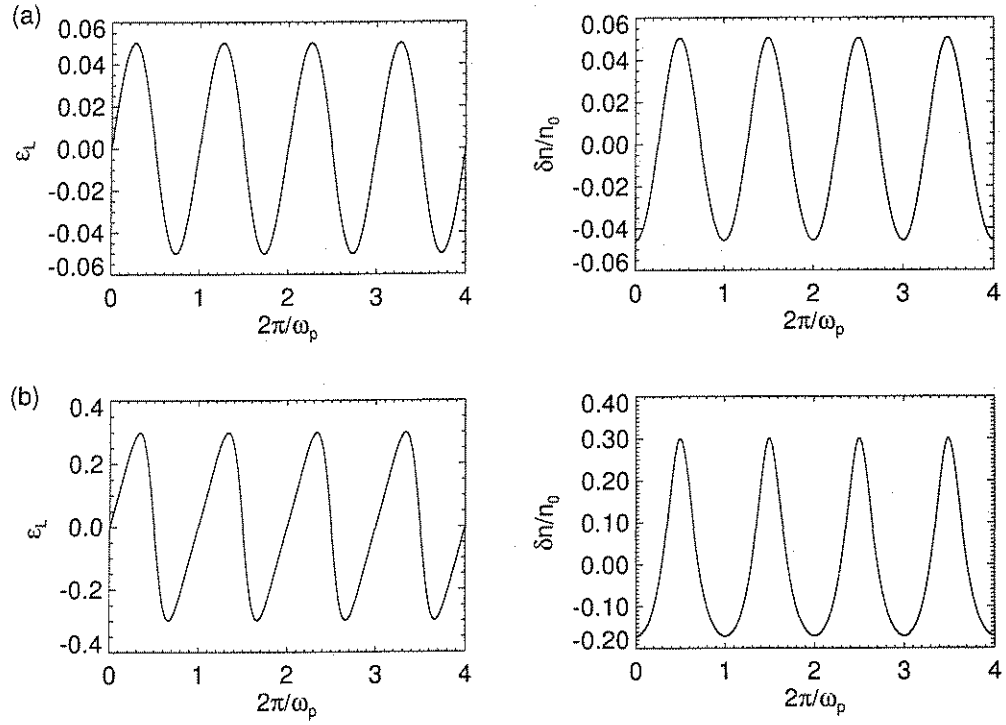
Figure 1.2: Illustration of the steepening of the plasma wave for larger density perturbations where (a) has a 5% wave amplitude (linear regime) and (b) has a 30% amplitude (nonlinear regime).

where E is the amplitude of the electric field of the laser. This means that for large amplitude plasma waves the resonant excitation frequency depends on the amplitude of the electric field of the laser. An important parameter in the driving of plasma waves is the peak of normalized laser vector potential, $\mathbf{a} = e\mathbf{A}/mc^2$, which is also equivalent to

$$\alpha_0 = v_{osc}/c = \frac{eE}{cm\omega} = \left(\frac{2e^2\lambda^2 I}{\pi m^2 c^5}\right)^{1/2} \simeq 8.6 \times 10^{-10}\lambda\sqrt{I}, \tag{1.4}$$

where I is the laser intensity in W/cm^2 and λ is the laser wavelength in microns. The value of α_0 is a way of measuring the strength of the specific laser utilized to excite the plasma waves and is equivalent to the transverse quiver velocity v_{osc}/c that the electrons in the field of the laser achieve.

1.2   Plasma Production by Tunneling Ionization

The plasmas utilized in laser driven, plasma based, particle accelerators are most often created by the laser itself through tunneling ionization of neutral gas [9]. Tunneling ionization happens when the laser field is large enough to allow a bound electron to overcome the Coulomb potential of the atom. Depending on the value of the Keldysh parameter, γ_k, either multi-photon ($\gamma_k \ll 1$) or tunneling ionization ($\gamma_k \gg 1$) occurs. The Keldysh parameter is $\gamma_k = (E_{ion}/2\Phi_{pond})^{1/2}$ where E_{ion} is the ionization potential in eV and where the laser ponderomotive potential in eV is

$$\Phi_{pond} = \frac{e^2 E^2}{4m\omega^2} = 9.33 \times 10^{-14} I\lambda^2. \tag{1.5}$$

For experiments in the Neptune Laboratory hydrogen gas is self-ionized by using the 10 μm CO$_2$ laser where $\gamma_k \approx 0.04$, which means that tunneling is the primary ionization mechanism. In addition collisional ionization can be an issue for pressures >2 torr [10].
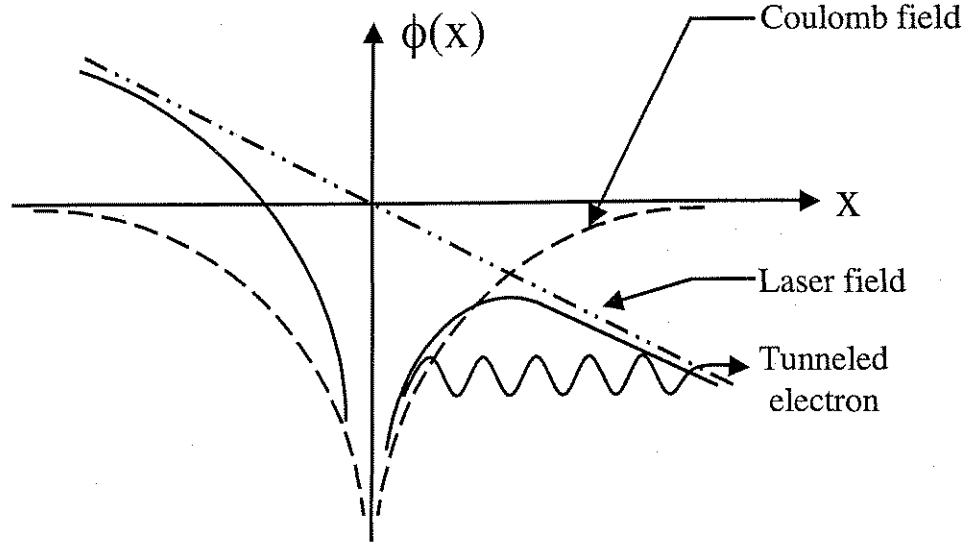
Figure 1.3: Effect of the laser field on the Coulomb potential.

When in the tunneling regime, the probability that an electron tunnels through the atomic potential barrier is given by [11],

$$w(t) = \frac{4me^4}{\hbar^3} \left(\frac{E_{ion} E_a}{E_h E(t)} \right) \exp \left[-\frac{2}{3} \left(\frac{E_{ion}}{E_h} \right)^{3/2} \frac{E_a}{E(t)} \right], \qquad (1.6)$$

where E_a is the atomic unit of electric field which is 5.21×10^{11} V/m, $E(t)$ is the time varying electric field of the laser, and E_h is the ionization potential for hydrogen which is 13.6 eV. The illustration in Figure 1.3 shows the suppression of the Coulomb potential due to presence of a large external electric field, and the tunneling of an electron through this potential. From this probability the plasma density as function of time can be determined using the rate equation,

$$\frac{dn(t)}{dt} = w(t)[n_g - n(t)], \qquad (1.7)$$

where n_g is the neutral gas density.

1.3 Resonant Plasma Waves Driven by Two-Frequency Laser Pulses

Resonant beat-wave excitation of relativistic plasma waves is the method by which electrons have been accelerated in past and present experiments conducted at UCLA [5, 12] and elsewhere [13, 14]. Current experiments in the Neptune Laboratory utilize a two-frequency CO_2 laser pulse from the Neptune laser system [15] with oscillation frequencies $\omega_{1,2} = 2\pi c/\lambda_{1,2}$ where $\lambda_1 = 10.591$ μm (P20) and $\lambda_2 = 10.275$ μm (R16). The frequency separation $\Delta\omega = \omega_2 - \omega_1 = 5.5 \times 10^{12} s^{-1} \approx \omega_p$ implies a plasma density of 9.4×10^{15} cm^{-3} to resonantly drive a relativistic plasma wave with $\lambda_p \approx 340$ μm.

Initially, as a two-frequency laser drives a plasma wave, the amplitude of the wave grows linearly in time with $\varepsilon_L(t) = \frac{1}{4}\alpha_1\alpha_2\omega_p t$, where α_1 and α_2 are the peak of the normalized laser vector potential for the two wavelengths of interest (Equation 1.4). As mentioned before, for large amplitude oscillations the relativistic mass increase of the electrons results in a shift of the driven plasma frequency. Rewriting Equation 1.3 for a two-frequency laser one obtains,

$$\Delta\omega = -\frac{3}{16}\left(\frac{eE_1}{mc\omega_p}\right)\left(\frac{eE_2}{mc\omega_p}\right)\omega_p, \qquad (1.8)$$

where E_1 and E_2 are the electric fields associated with ω_1 and ω_2. Eventually the plasma wave amplitude saturates due to this detuning between the driver at $\Delta\omega$ and the relativistic plasma frequency ω_p, and the amplitude at which the plasma wave saturates is $\varepsilon_L^{max} = (16\alpha_1\alpha_2/3)^{1/3}$ [16]. This value is modified if the beat frequency and the plasma frequency are related by,

$$\Delta\omega = \left(1 - \frac{(9\alpha_1\alpha_2)^{2/3}}{8}\right)\omega_p. \qquad (1.9)$$

Compensation for relativistic detuning is accomplished experimentally by increasing the plasma density, and the resulting amplitude at which the plasma wave

saturates [16]:

$$\varepsilon_L^{max} = 4(\alpha_1\alpha_2/3)^{1/3}, \tag{1.10}$$

is larger by about 60 %. The intensity dependence of the resonant density is demonstrated in experimental results and simulations to be presented later in this dissertation.

1.4 Electron Injection and Phasing

The electrons that are to be accelerated can be injected into the accelerating structure from an external electron beam or be generated by the background plasma itself. For large amplitude plasma waves with amplitudes above the relativistic wave-breaking threshold, ε_0^{rel}, there is a possibility for background plasma electrons that acquire a longitudinal momentum large enough through wave-breaking to be trapped by the wave structure. For high density plasmas ($n_0 \sim 10^{18}$ cm^{-3}) there are enough trapped particles so that injection of an external electron beam may not be necessary. Particle trapping in plasma accelerators is discussed in detail in [17]. In the experiments described in this thesis, the plasma wave amplitude for the beat-wave excited plasma is approximately 10–15% ($n_0 \approx 10^{16}$ cm^{-3}), well below the wave-breaking amplitude, therefore electrons must be externally injected.

CHAPTER 2

Experimental Setup

This chapter on the PBWA experimental setup is divided into four sections: (1) the Neptune laser system, (2) characteristics of the laser and laser ionized plasma at the interaction point (IP), (3) the Neptune photo-injector and linac, and (4) the electron detection systems. In Figure 2.1, a schematic of the laboratory space is presented and shows the size of the laboratory (as a reference the optical table for the CO_2 oscillator cavity is 12 feet in length). A simplified diagram of the entire PBWA experiment is presented in Figure 2.2, illustrating some of the key components in the system.

2.1   The Neptune Laser system

The Neptune laser system consists of the two-wavelength CO_2 laser oscillator, the preamplifier (regenerative amplifier), and the MARS amplifier. In the sections below, the CO_2 laser system, along with the focusing and transport optics to the interaction point (IP) between the plasma wave and the injected electron bunch are described.
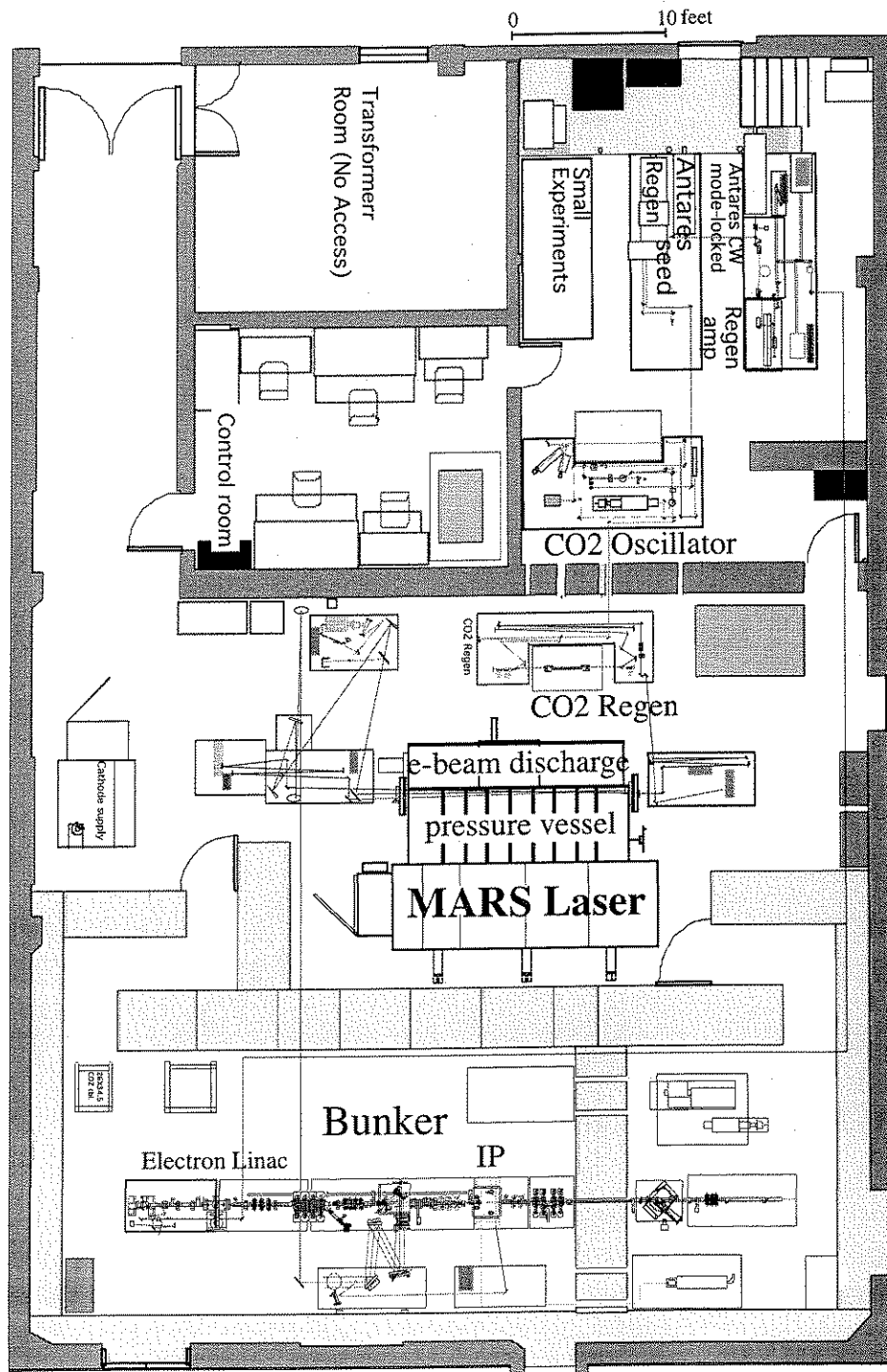
Figure 2.1: Schematic of the Neptune Laboratory for Advanced Accelerator Research.
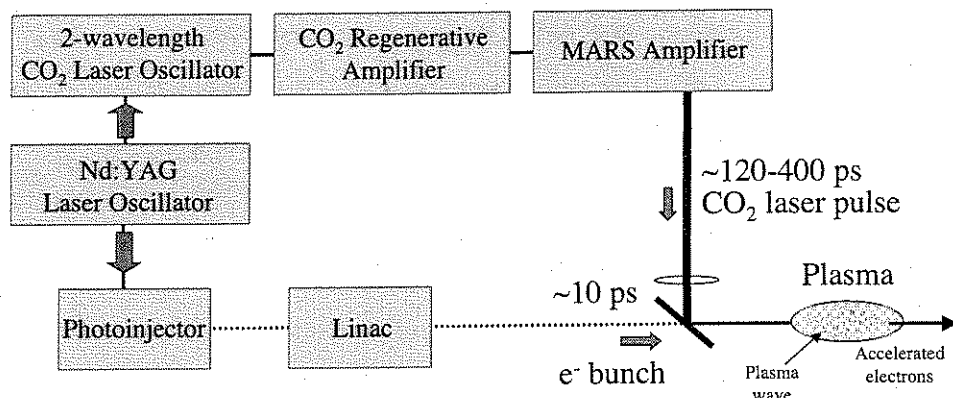
Figure 2.2: A simplified diagram of the PBWA.

2.1.1 Picosecond Two-wavelength CO_2 Laser Oscillator

Short ($\sim$120–400 ps) two-wavelength (10.591 μm and 10.275 μm) laser pulses at $\sim$1 TW levels are needed to excite large amplitude electron plasma-waves. In previous experiments at UCLA, an intracavity absorption cell was used to provide simultaneous two-wavelength operation of a long pulse oscillator, and Optical Free Induction Decay (OFID) produced a pulse length less than 100 ps. However, this system lacked shot to shot stability for the relative amplitudes of the two wavelengths and, more importantly, did not allow synchronization of the formation of the plasma wave with the injected electrons. In the Neptune Laboratory, an intracavity grating with two rear mirrors with two low-pressure seed lasers along with a TEA (transversely excited atmosphere Lumonics HyperEX 400) laser solve the former problem, while semiconductor switching solves the latter. In Figure 2.3, a drawing of the oscillator is presented showing the two low-pressure lasers and the TEA gain medium. To produce comparable amplitudes for the two CO_2 laser lines, it was necessary to make it more favorable for oscillation on the 10.275 μm line (the 10.591 μm line normally has much higher gain than the 10.275 μm line). To do so, the timing of the two seed lasers is

12
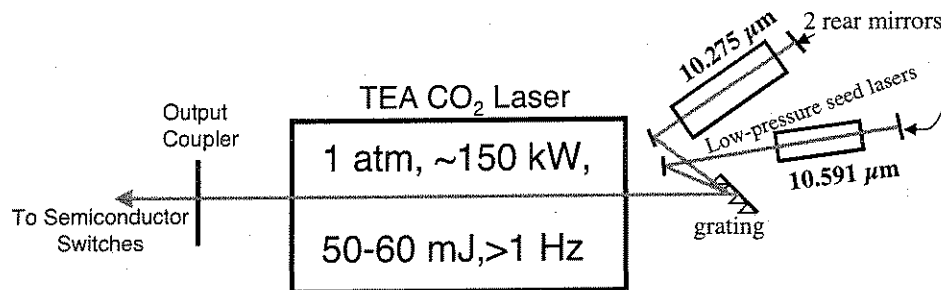
Figure 2.3: Schematic of the Two-Wavelength CO_2 Laser Oscillator Cavity.

adjusted, thereby seeding a larger number of photons into the weaker 10.275 μm line. In this configuration, 1.4 times more radiation on the 10.275 μm line is produced than on the 10.591 μm line; from this point onward the two wavelengths will be referred to 10.3 μm and 10.6 μm, respectively.

Semiconductor switching [18] is employed to produce picosecond CO_2 laser pulses in order to seed a 3–5 atmosphere CO_2 regenerative amplifier which will then produce pulses to be further amplified in the MARS amplifier. This method provides sub-nanosecond CO_2 laser pulses systematically synchronized to the laser providing the gate pulse (one that has a photon energy above the bandgap of the semiconductor). As a result, the laser produced plasma-wave can be synchronized to the injected electrons produced from a photo-cathode, which is driven by frequency quadrupling the same laser that was used to produce the gate pulse for the semiconductor switch. In this case, germanium is used to optically gate p-polarized 10 μm radiation with a $\sim$100 ps laser pulse with a wavelength of 1064 nm originating from a Nd:YAG regenerative amplifier seeded by pulses from a Nd:YAG mode-locked laser oscillator. The Nd:YAG laser system and the synchronization of the laser pulse and electron beam will be described in more detail in section 2.3.

In semiconductor switching, the p-polarized CO_2 laser pulse is incident upon

Before Switches	time → 200 ns
Reflected off Switch #1	500 ps
Transmitted by Switch #1	200 ns
Transmitted by Switch #2	50-500 ps (adjustable)
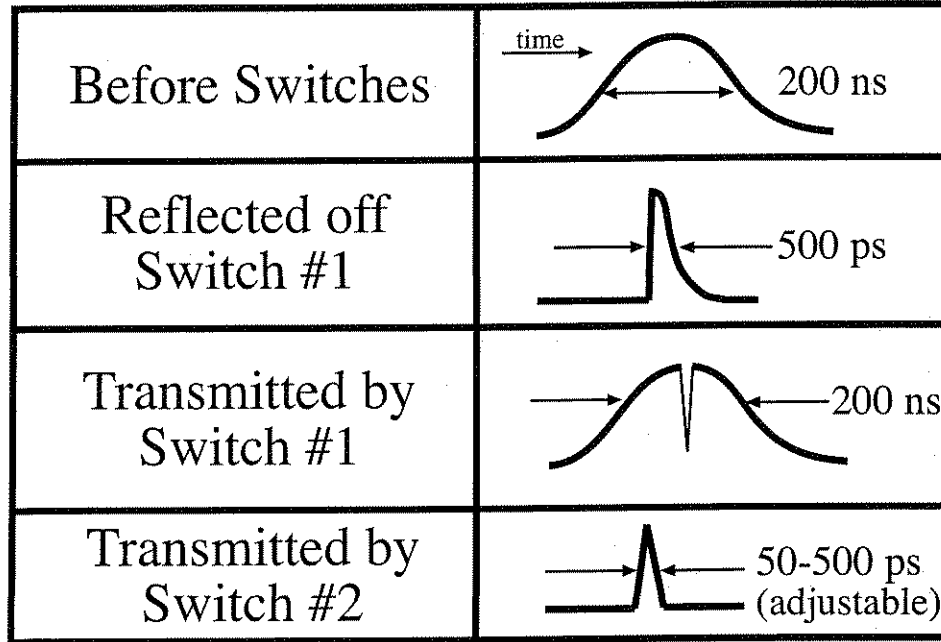
Figure 2.4: Temporal laser pulse shapes produced by semiconductor switching.

a germanium slab at Brewster's angle. Without any 1064 nm radiation, the semiconductor is transparent to the 10 μm pulse; but, when the 1064 nm radiation illuminates the surface of the material, it excites electrons from the valence band to the conduction band. The semiconductor is effectively metallized for the time that the electron density remains above the critical density for the CO_2 laser frequencies. In this case, intrinsic germanium (n-type) is used as the switching material so any gate pulse with a photon energy E_{ph} above 0.67 eV can be used and 1064 nm light is sufficient with $E_{ph} \simeq 1.2$ eV. Semiconductor switches in reflection and transmission are used to produce variable length picosecond laser pulses; the pulse shapes produced by this system are shown in Figure 2.4. More details of the master oscillator system can be found in [18]. The ~100 picosecond laser pulses produced by the oscillator typically with energies from 1–7μJ are next injected into the preamplifier, which is a CO_2 regenerative amplifier.
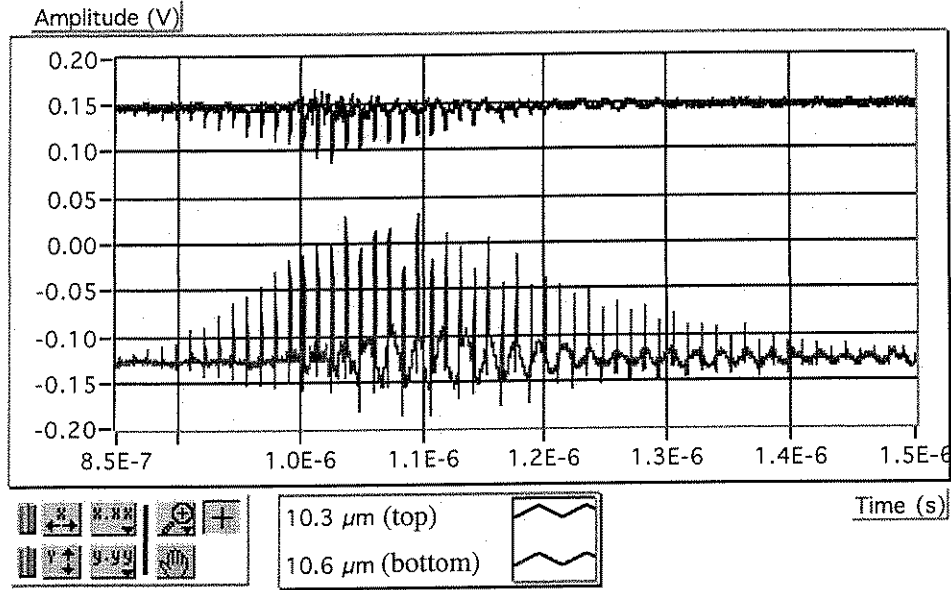
Figure 2.5: Voltage traces of the pulse trains exiting the preamplifier recorded using Hg:Cd:Te detectors.

2.1.2 CO_2 Regenerative Amplifier

The CO_2 regenerative amplifier in the Neptune Laboratory takes input pulses from the two-wavelength oscillator and amplifies them using the injection mode-locking technique [19]. The gain medium utilized is a Lumonics model 280 laser capable of operating between 3–8 atmospheres. For the case of two-wavelength amplification, it is necessary to operate above 6 atmospheres to produce amplified pulses of comparable amplitudes for both CO_2 laser lines; temporal broadening of the laser pulse is not an issue above 3 atmospheres. The beam output from the master oscillator is injected into the cavity of the preamplifier with a spot size w_0=3.2 mm and is not mode matched, so the subsequent beam profile is defined by the size of the regenerative amplifier itself.

Typically the pulse train produced by the regenerative amplifier has $\sim$25 mJ of energy and it exits after a delay of $\sim$250 ns. The output from the regenerative

15

amplifier is a two-wavelength p-polarized pulse train from which a single pulse is extracted by use of a CdTe Pockel's cell. Figure 2.5 is a plot of the two-wavelength pulse train exiting the regenerative amplifier after separation on a diffraction grating (the 10.3 μm signal is inverted). The relative amplitudes of the two lines are not represented in the voltage traces due to differences in the signals incident on the detectors; in general, the line ratio is approximately 3:1 in favor of 10.3 μm line. The Pockel's cell is driven by a laser triggered spark gap at $\sim$22 kV that is triggered by a portion of the Nd:YAG pulse used in semiconductor switching. The switched high voltage pulse is put into a long high voltage cable with a delay of $\sim$250 ns and achieves a voltage of $\sim$11 kV at the Pockel's Cell. This voltage is close to the half-wave voltage of the Pockel's Cell (12 kV) and is sufficient to select a single 2-frequency laser pulse. More detail on the regenerative amplifier can be found in [19].

2.1.3   MARS Laser Amplifier

The MARS amplifier is used to amplify the $\sim$0.5–1 mJ two-wavelength pulses that exit the preamplifier using a 3-pass setup. The MARS amplifier is a large aperture, e-beam controlled discharge amplifier with an SF_6 absorber cell utilized on the second pass to prevent self-oscillation and to preferentially attenuate the 10.6 μm radiation because, just as in the previous stages of the laser system, a higher level of the 10.3 μm radiation is desirable. The pressure vessel of the gain medium is at 2.5 atmospheres to minimize the possible temporal broadening of the laser pulse that may occur during the amplification process. Operation at high pressure broadens the amplifier gain curve thereby allowing amplification of $\sim$100 ps laser pulses. After the first pass, the beam is expanded to prevent damage on the optics, and reaches approximately 5.5" ($\sim$14 cm) after the third

Shot # 10156
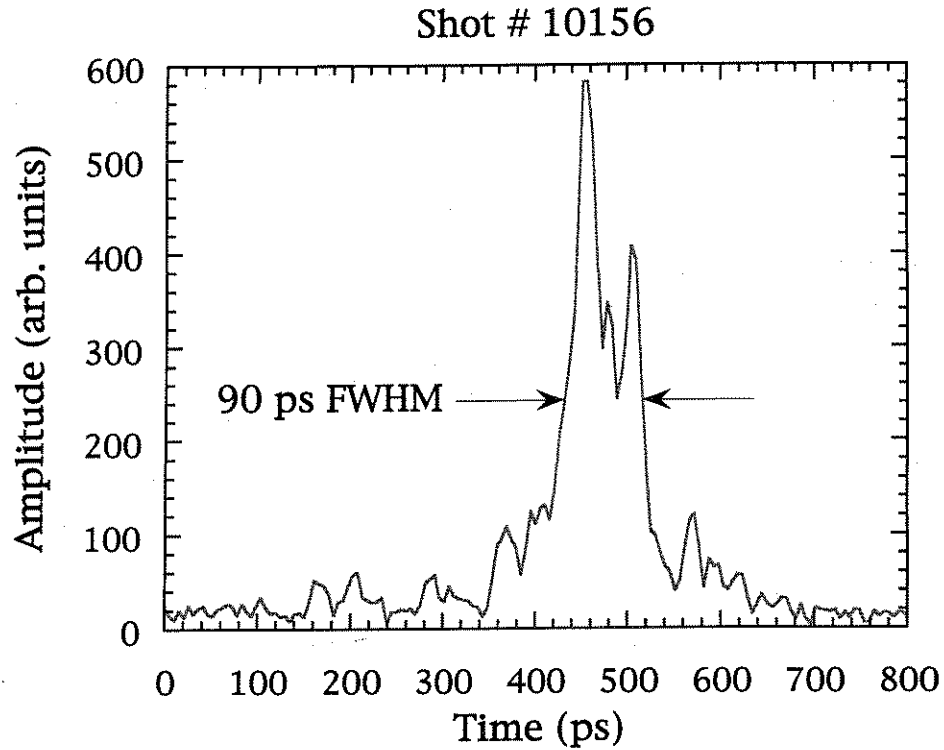
Figure 2.6: Temporal pulse shape of high power CO_2 laser pulse.

pass. The amplified laser pulses produced by the system are typically between 100–400 ps (depending on the seed pulse length), with an energy between 100–200 J. Although shorter pulses can be produced and are discussed in [20], the laser pulse lengths utilized in the experiment are generally ~100 ps or longer. Figure 2.6 is a representative temporal pulse shape of the CO_2 laser pulse produced by taking a line-out of a streak camera image produced by optically mixing of the 10 μm laser pulse with a diode laser pulse [20]. The next section discusses the laser beam profile and important parameters of the laser produced plasmas at the interaction point (IP).
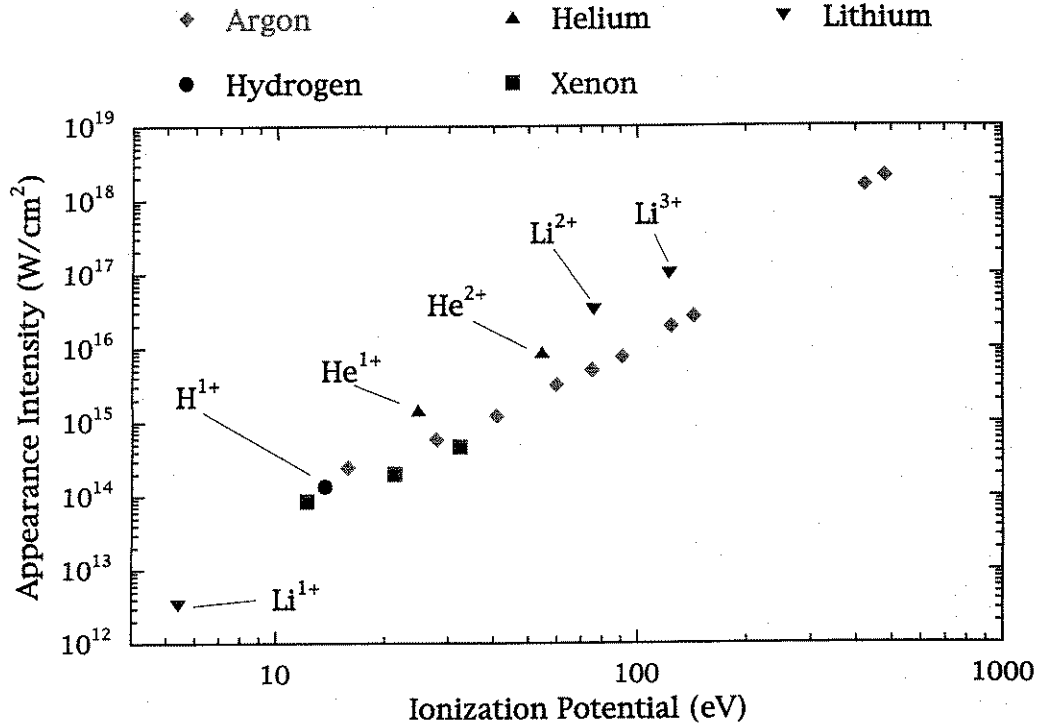
Figure 2.7: Appearance intensity threshold for different gases and different ionization levels.

2.2 Laser Beam at the IP

Utilizing the terawatt CO_2 laser system discussed in the previous sections, uniform tunnel ionized plasmas were produced in hydrogen gas fills (slow gas flow). According to the Barrier Suppression model [21], the appearance intensity threshold for a given gas is given by Equation 2.1:

$$I_{th} = \frac{cE_{ion}^4}{128\pi e^6 Z^2} \approx \frac{4 \times 10^9 E_{ion}^4}{Z^2},$$
(2.1)

where E_{ion} is the ionization potential of the gas and Z is the charge state. For hydrogen, $I_{th} \approx 1.4 \times 10^{14}$ W/cm^2 and in Figure 2.7 the appearance intensity for different gases is plotted versus ionization potential.

18

Focusing Geometry	w_0 (μm)	Intensity (W/cm^2)	$2Z_R$ (mm)	Energy (J)
f/2	$\sim$50	$\sim 10^{15}$	1.6	$\sim$35
f/3	$\sim$80	8×10^{14}	4.0	$\sim$25
f/18	$\sim$200	4×10^{14}	25.0	$\sim$100

Table 2.1: Laser Beam parameters at the IP.

2.2.1 Focusing Geometries

To ionize the gas and to drive the plasma wave, two different focusing schemes were utilized for two different sets acceleration experiments– one using a 40° off-axis parabolic mirror (OAP) with a 15.2 cm focal length (for f/2 and f/3 focusing) and another with a NaCl lens with a focal length of 256.2 cm (for f/18 focusing). Although the acceleration results presented in the next chapter were obtained using f/2 focusing of a $\sim$7.6 cm diameter laser beam, the characterization of focusing using the OAP was done with f/3 focusing and will be discussed here. Table 2.1 presents the typical laser parameters for f/2, f/3, and f/18 focusing geometries at the IP. The setup in the main experimental area in the Bunker is illustrated in Figure 2.8 and shows both focusing schemes. The f/18 beam path has approximately $\sim$100 J of energy while the f/3 path has $\sim$25 J (measured using a large diameter Scientech calorimeter) when both beam-lines are used simultaneously. Two synchronized focusing beam-lines can be produced by using a 2" mirror to split part of the 5.5" laser beam and then using a delay line to match the two distances to the IP. This was done to provide the possibility of attempting laser injection experiments discussed in more detail in [22]. Replacement of the pick-up mirror with a larger optic allowed much larger intensities to be produced for acceleration experiments using the OAP.

In Figure 2.9(a), the low power spatial profile obtained without amplification
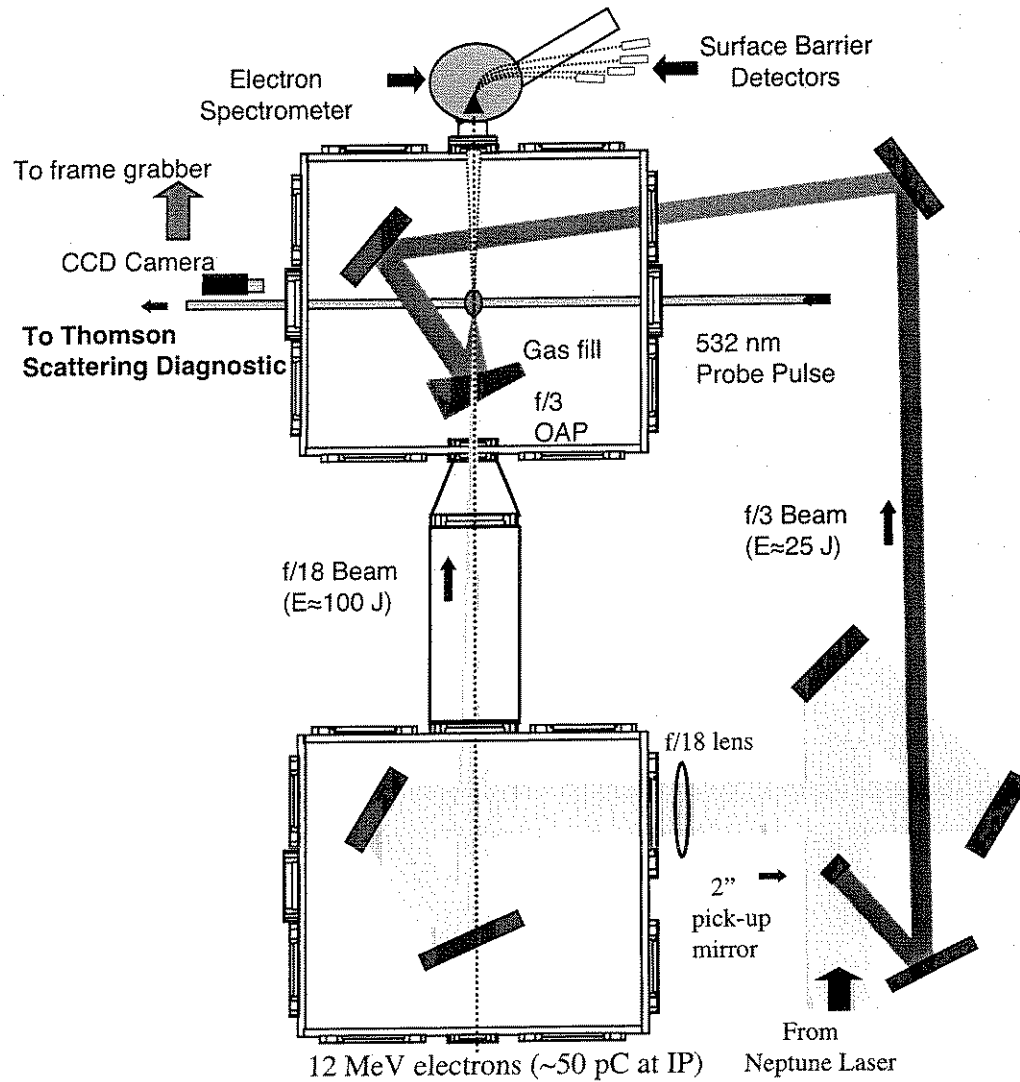
Figure 2.8: Experimental area near the IP showing the f/3 and f/18 focusing geometries and associated diagnostics.

in the MARS amplifier is presented for the f/18 beam at the IP as well as vertical and horizontal lineouts, 2.9(b) and 2.9(c) respectively. This image is obtained by sending the f/18 beam through a beam expanding telescope with $5\times$ magnification and imaging it on to a 128×128 pixel Spiricon pyroelectric camera. The structure around the central part of the f/18 beam profile is due to aberrations caused by the lenses in the expanding telescope, which consisted of bi-convex lenses (using meniscus lenses would have reduced the aberrations). For the f/18 beam path, a spot diameter, $2w_0$, of approximately 400 μm is obtained at the IP. This corresponds to an intensity of 4×10^{14} W/cm^2 ($\alpha_1 = \alpha_2 \simeq 0.12$) for a 120 J, approximately three times the appearance intensity of hydrogen. At this intensity, for a 1:1 line ratio, the electron quiver velocity in the laser field, v_{osc}/c, is $\simeq 0.17$ (Equation 1.4). The pyroelectric camera used has a pixel size of 100 μm, which prevents precise measurement of the f/3 beam size in the same method as the f/18 beam, even with magnification. To measure the f/3 beam size, burns on polaroid film were taken with the beam variably attenuated and then the radii of those burns were fit to a gaussian. Figure 2.10 shows that the spot diameter is approximately 160 μm for f/3 focusing, which corresponds to an intensity of 8×10^{14} W/cm^2 ($\alpha_1 = \alpha_2 \simeq 0.17$) for a 25 J laser pulse, well above the ionization threshold for hydrogen. For the f/2 focusing geometry, the intensity approaches ionization threshold for He^{1+} which is $\approx 1.5\times10^{14}$ W/cm^2 ($E_{ion} = 24.6$ eV for He^{1+}).

To align the beams, two CCD cameras, each with magnification optics to provide a resolution of 40 μm/pixel, viewed sparks produced by focusing the unamplified laser pulse on a graphite probe at the IP. As final verification of the intensity of the laser at the IP, images of the laser ionized plasmas were obtained by viewing plasmas from both f/18 and f/3 beam-lines using an 8-bit 640×480 pixel Cohu CCD camera with optics giving a 100 μm/pixel resolution connected
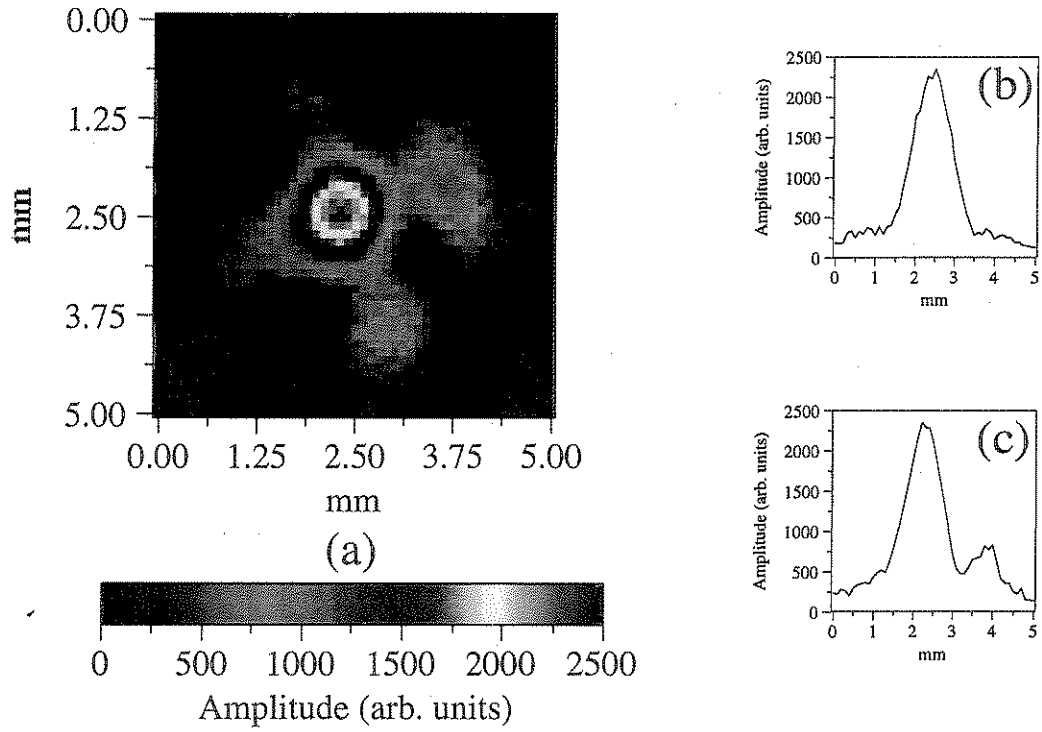
Figure 2.9: Profile of the f/18 beam at the IP with 5× magnification (a) and vertical (b) and horizontal (c) lineouts of the profile (scale on lineouts is also magnified).
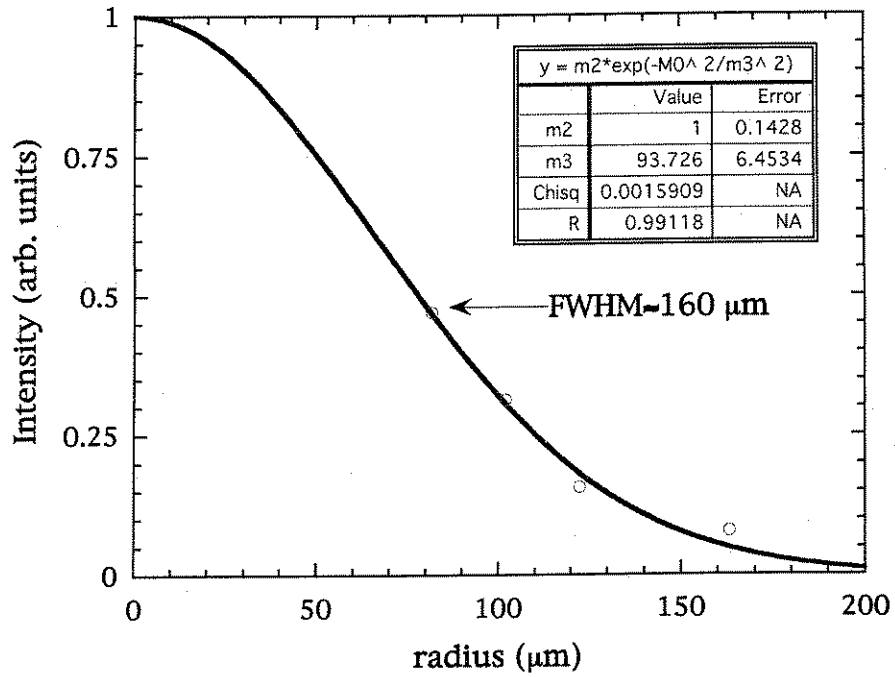
Figure 2.10: The f/3 beam profile with a gaussian fit at the IP.

to a frame-grabber. The physical length of each of the plasmas correlate well with the Rayleigh length of each focusing geometry; the f/3 beam has a Z_R of approximately 2.5 mm, while the f/18 has a Z_R of approximately 2.0 cm. In Figure 2.11(a) and 2.11(b), CCD images of the hydrogen plasma are presented for f/18 and f/3 focusing geometries, respectively. The two laser shots presented are taken at 165 mtorr for the f/18 geometry and 222 mtorr for f/3 focusing, in a hydrogen gas fill. The light that appears vertically at the center of the f/3 plasma image may be due to plasma electrons that are ejected by the large laser intensity produced by this strong focusing geometry.

(a)

Shot# 10614 Plasma at 165 mtorr

(b)

Shot # 10585 at 222 mtorr
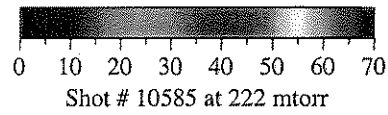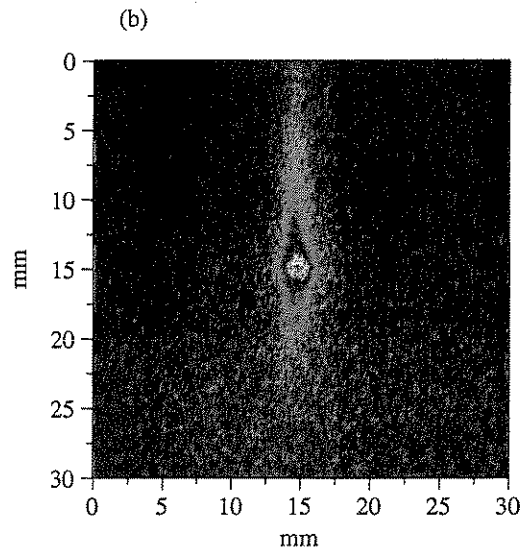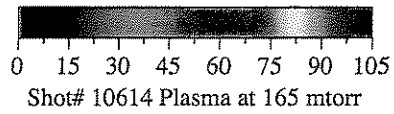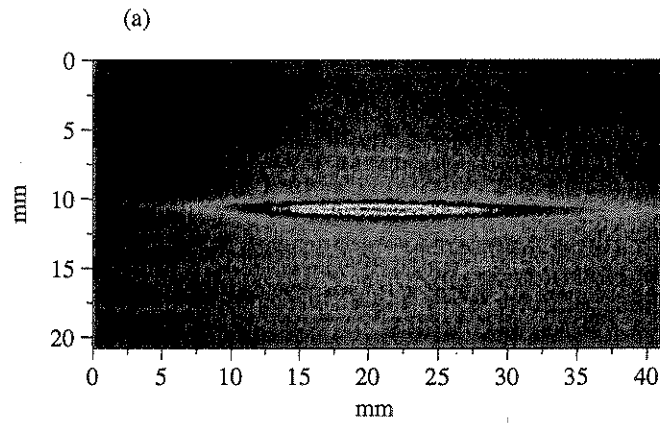
Figure 2.11: In (a) is an f/18 plasma image taken at 165 mtorr and (b) is an f/3 plasma image at 222 mtorr in a hydrogen gas fill.
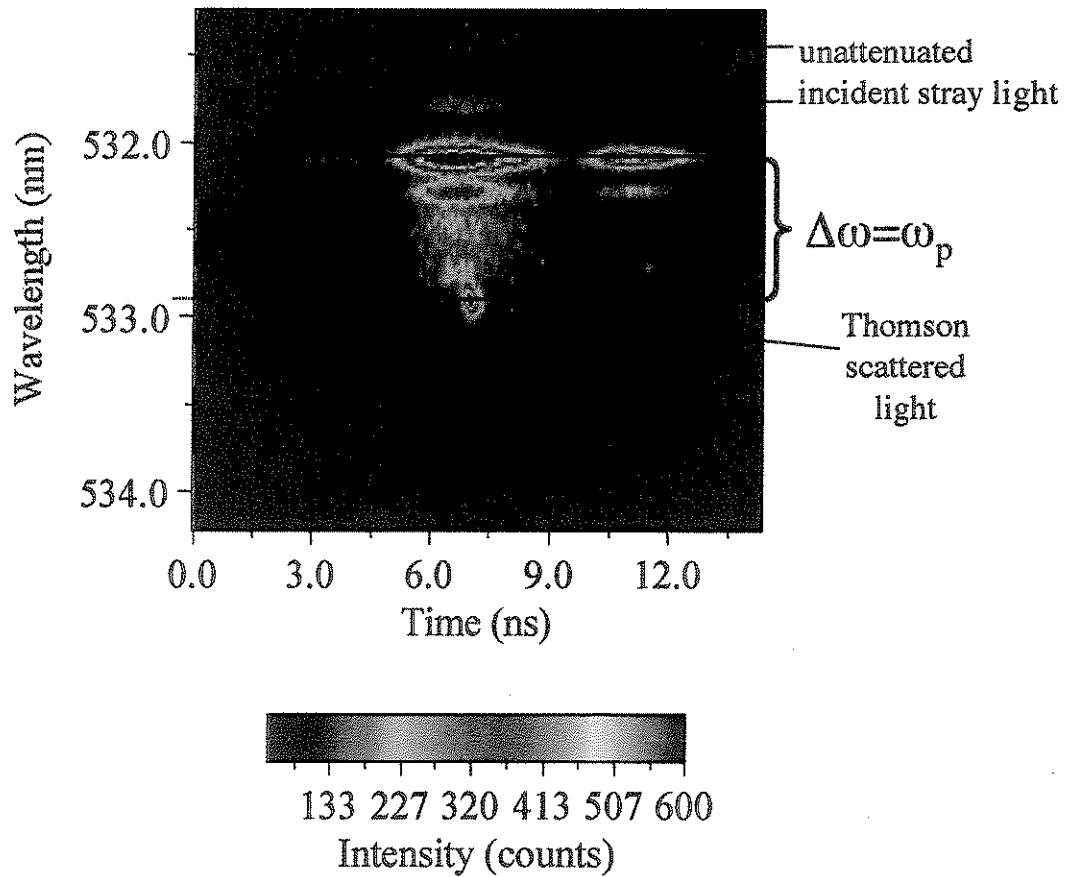
Figure 2.12: The Thomson scattered spectra for the f/2 focused laser beam at resonance in hydrogen.

2.2.2 Thomson Scattering

After ionizing the hydrogen gas, the next step in the experiment was to experimentally determine if indeed a relativistic plasma wave is driven by the beat-wave. In addition to verifying that the plasma wave exists, the amplitude of each plasma wave must be determined. To do so, Thomson scattering of a 532 nm laser beam with a transverse and/or collinear probe of the plasma wave was measured. After probing the plasma wave, the Thomson scattered signal was temporally and spectrally resolved using a streak camera and spectrometer. More details of this setup can be found in [23]. The frequency shift measured by Thomson scattering yields the plasma frequency and at the resonant pressure corresponds to the frequency separation, $\Delta\omega$, of the two laser lines. Figure 2.12 presents the temporally resolved f/1.5 focusing collinear Thomson scattering spectra which has a frequency shift of $\Delta\omega = \omega_p$. The stray light streaks on either side of the probe laser wavelength are due to a filter which is used to attenuate the 532 nm stray light.

2.2.3 Resonant Pressure in Hydrogen

As mentioned earlier, for the two laser wavelengths utilized in the PBWA experiment the resonant frequency corresponds to a density of 9.4×10^{15} cm^{-3} (for $v_{osc}/c \ll 1$). Taking a room temperature of $T = 20°$ C (293 K) in the expression for the pressure, $P = \frac{n_0 k_b T}{2}$ (because hydrogen is diatomic there is a factor of 1/2), one obtains a resonant pressure of $\sim$143 mtorr. As discussed in Chapter 1, the resonant density is related to the laser intensity ($v_{osc}/c \approx 1$) and can be determined using Equation 1.9. For the f/2 case, the resonant pressure was determined by Thomson Scattering to be $\sim$180 mtorr corresponding to $n = 1.2 \times 10^{16}$ cm^{-3}, and using Equation 1.9 it implies an intensity somewhat larger than the

actual intensity; for a 1:1 line-ratio $\alpha_1 = \alpha_2 \simeq 0.4$. For the f/18 geometry, the resonant pressure was $\sim$165 mtorr which corresponds to a density of 1.1×10^{16} cm^{-3}, and for a 1:1 line-ratio it means $\alpha_1 = \alpha_2 \simeq 0.25$. This discrepancy may be due to a reduction of the plasma density in the focal region caused by transverse blow-out of the plasma by the laser pulse. This blow-out is more severe for the f/2 case than for the f/18 case, as will be shown later. Electrons were injected into the accelerating structure after determining the optimum density and wave amplitude produced by the beat-wave for both geometries, using Thomson scattering. In the next section, the Neptune linac system and synchronization of the laser pulse to the electron beam are described.

2.3 The Neptune Linac System

The Neptune linac system consists of an RF photo-injector (photo-cathode electron gun), a linac section, and a transport beam-line. This system is described in more detail in [24].

2.3.1 The Neptune Photo-Injector and Linac System

The RF for the entire system originates from the 38.08 MHz mode-locker of the Nd:YAG oscillator, which is multiplied by 75 to produce 2.856 GHz (S-band). The photo-cathode electron gun is a 1.625 cell, π-mode standing wave cavity and can produce a peak on-axis field gradient of 85 MV/m. The UV illuminating the photo-cathode ($\lambda = 266$ nm) originates from the drive laser which is a 1064 nm mode-locked Nd:YAG laser oscillator producing $\sim$100 ps pulses. The output of the oscillator is matched into a 500 m long, single-mode optical fiber which broadens the laser pulse in time and produces a frequency chirp. The long chirped

Bunch length (ps)	Charge (pC)	ε (mm·mrad)	σ_r (μm)	Energy (MeV)
10	50–100	12	150	~11.0–12.4

Table 2.2: Electron Beam parameters at the IP.

pulse is then amplified in a Nd:YAG regenerative amplifier and then sent to a pair of gratings that compress the pulse down to ~10 ps FWHM (6 ps RMS); this is traditionally referred to as chirped pulse amplification (CPA). The same oscillator pulse goes to another regenerative amplifier to drive the semiconductor switches for the CO_2 laser oscillator. The 1064 nm short 10 ps pulse is then upconverted to 532 nm with a BBO (Beta Barium Borate) doubling crystal and then transported to the bunker where it is doubled again with another BBO crystal to produce ~100 μJ of UV at 266 nm. This 266 nm radiation illuminates the single crystal Cu photo-cathode of the photo-injector and has a quantum efficiency of 5×10^{-5} e$^-$/photon, corresponding to a charge of ~1 nC. The linac section is a 7 and 2/2 cell π-mode standing wave plane-wave-transformer (PWT) and can operate at ~13 MW of RF power corresponding to a peak field of 50 MV/m. The typical electron beam energy after the linac is between ~11.0–12.4 MeV and is measured using the chicane as well as the magnetic spectrometer which is used for measuring the accelerated electron energy spectrum. The electron beam has an energy spread of ~0.35 % with a low energy tail. This energy range of the electron beam corresponds to a $\gamma_\phi \approx 22$–25 which means that the velocity of the electrons is somewhat slower than the phase velocity of the plasma wave which has a γ_ϕ ~32. Although this is not the optimum case for trapping the particles into the plasma wave, the dephasing of particles over the length of the plasma wave structure is negligible.

2.3.2 The Electron Transport Beam-Line

Table 2.2 summarizes important parameters of the electron beam at the IP. The electron beam is transported to the IP down the transport beam-line and through a 1 μm thick Mylar^{TM}window which separates the high vacuum system ($\sim 10^{-7}$ torr) of the RF gun and the coarse vacuum of the CO_2 laser beam transport line. Only $\sim$50–100 pC of charge reaches the interaction point due to scraping of a portion of the beam charge on a lead 1 mm aperture that is part of the Mylar^{TM}window holder. Propagating the electron beam through the Mylar^{TM}also causes significant emittance growth (to $\varepsilon \simeq 12$ mm·mrad) which eventually limits the minimum spot size that is achievable at the IP ($\sigma_r \simeq 150$ μm). Figure 2.13 is a schematic of the electron beam-line transporting the electron beam to the IP. The figure shows the photo-cathode and linac, as well as the transport electron beam optics (there are a series of quadrupole magnet triplets used to focus and direct the beam).

To match the electron beam spot size to the size of the plasma accelerating structure, the entire transport line was modeled using PowerTrace (Trace3D) for a 12.4 MeV beam. The horizontal (solid line) and vertical (dashed line) beam spot sizes gave limitations on the size of the transportation tubes as well as the field requirements to focus the beam at the IP (the window size is 2.5 mm for both x and y in Figure 2.14). Figure 2.14 shows that both the x and y sizes of the beam are minimized at the IP. The transport line that is modeled starts from the electron gun and ends at the IP. This model does not take the Mylar^{TM}window into account, so the spot size at the IP is not the one predicted by the model, due to emittance growth induced by the Mylar^{TM}(the emittance is larger approximately by a factor of three with the window).

To overlap the CO_2 laser beam and the electron beam at the IP, magnified
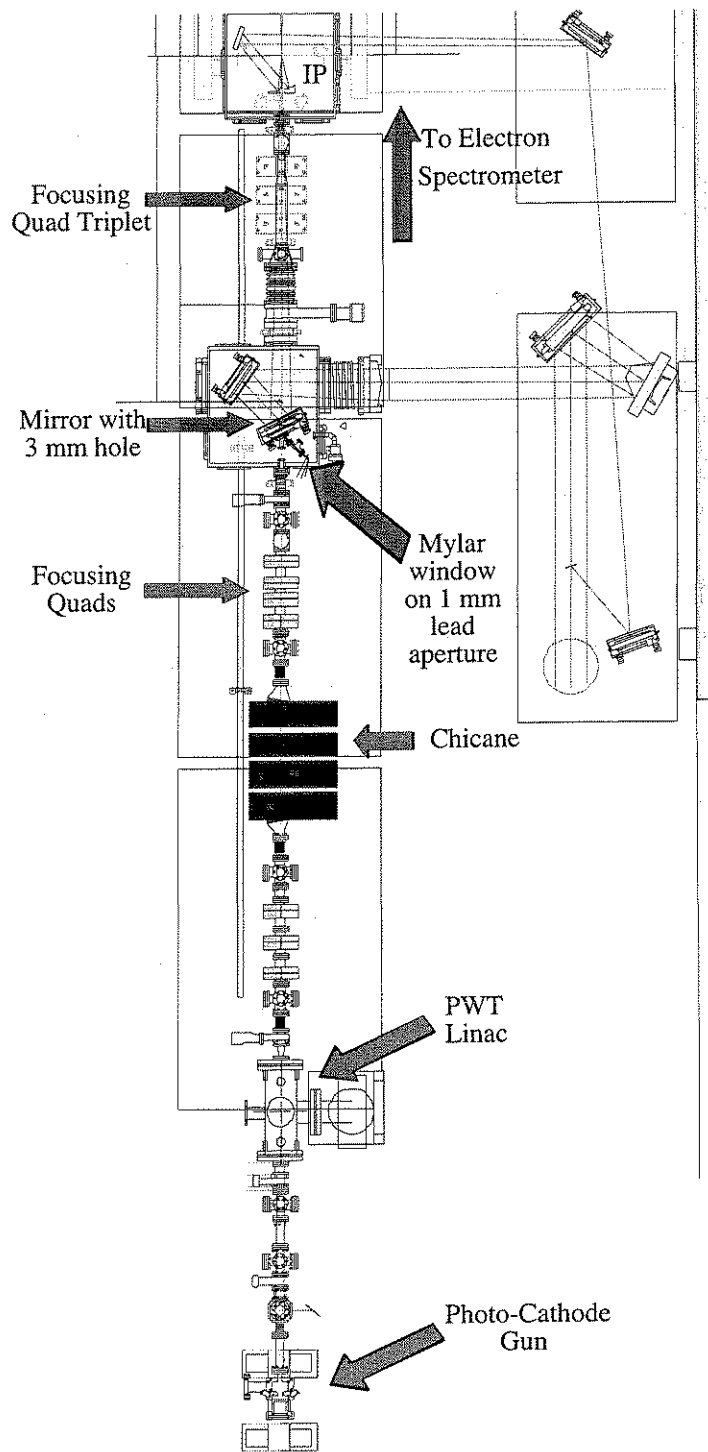
Figure 2.13: Electron Beam Transportation line to the IP.
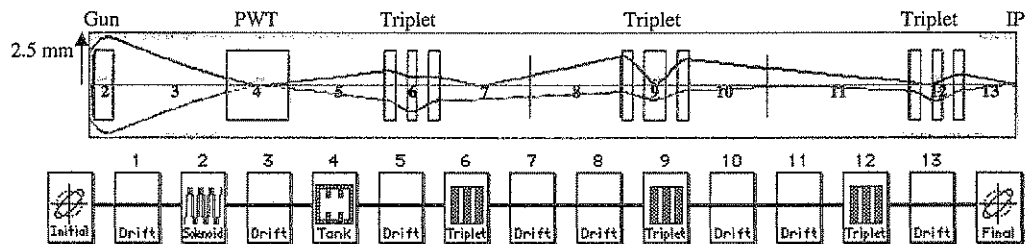
Figure 2.14: Horizontal (red line) and Vertical (blue line) Electron Beam Envelopes obtained using PowerTrace from the electron gun (Initial) to the IP (Final).
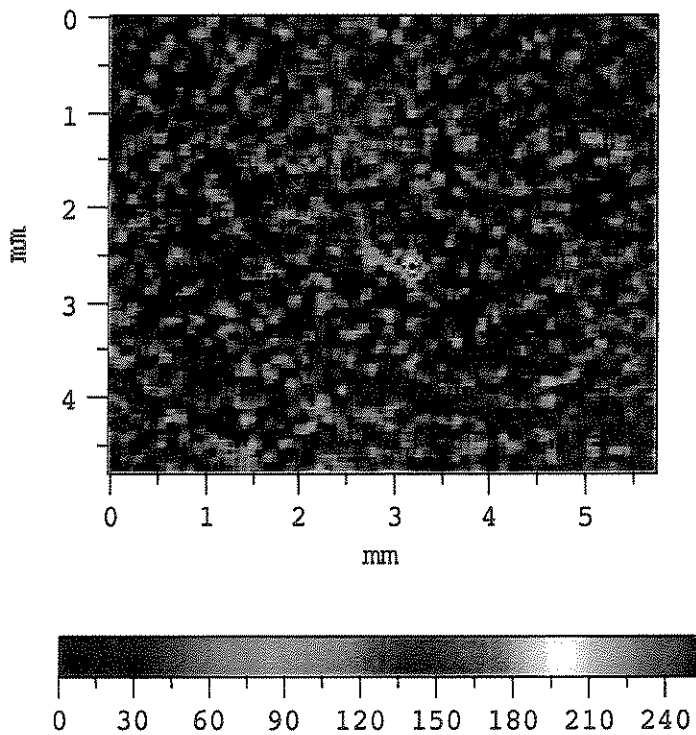
Figure 2.15: Electron beam image at the IP (intensity scale is in arbitrary units).
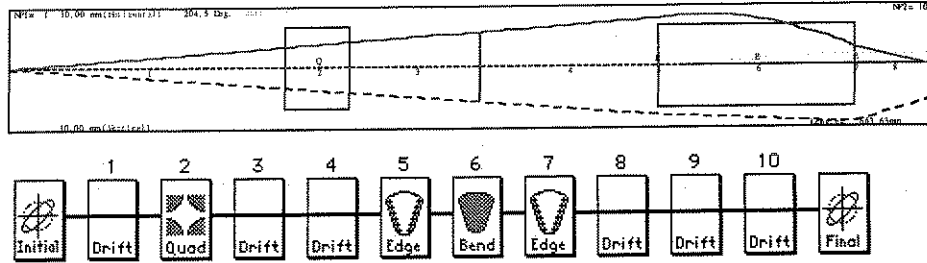
Figure 2.16: Horizontal (solid line) and Vertical (dashed line) Electron Beam Envelopes obtained using PowerTrace for propagation from the IP to the detection plane of the electron spectrometer.

CCD images were used, along with a 3-axis probe assembly that allowed precise positioning of graphite films for the laser beam and phosphor screens for the electron beam. Figure 2.15 is a CCD image of the electron beam hitting a phosphor screen that is a piece of Mylar^{TM}coated with fluorescent paint (the intensity scale for the image has arbitrary units). This image shows that the beam size, σ_r, is $\sim$150 μm for both transverse dimensions.

After the plasma, the electron beam travels through a magnetic spectrometer that images the beam at the exit of the plasma (object plane) onto detectors placed at the exit of the vacuum assembly (near the image plane of the spectrometer) with energy dispersion in the horizontal plane. In Figure 2.16, the electron beam propagation from the IP to the detection plane of the electron spectrometer is plotted. The input emittance used in this model is 4.3 mm·mrad and has taken the effect of the Mylar^{TM}window into account.

CHAPTER 3

Electron Beam Integration with CO_2 Laser System and Electron Acceleration

The first parts of this chapter describe the integration of the laser system and electron beam (spatial and temporal overlapping) as well as the electron detection diagnostics. The rest of this chapter discusses the electron acceleration results obtained from both f/2 and f/18 focusing geometries. With f/2 focusing the acceleration results are influenced by the large transverse fields that negatively affect the acceleration process. The acceleration results with f/18 focusing are limited by the amplitude of the wake-field produced as a result of the relatively large spot size, but demonstrate a significant energy gain out to $\sim$50 MeV over a $\sim$2.5 cm interaction length corresponding to an average gradient of 1.5 GeV/m.

3.1 Synchronization and Integration of the Laser System and Electron Beam System

3.1.1 Nanosecond Synchronization of Electrons and Photons

Figure 3.1 is a schematic that illustrates the overall electronic triggering system and shows that the clocks for the whole system are a master video camera and the mode-locker of the Nd:YAG oscillator. This figure also shows that the signal originating from a master camera is used to synchronize all of the triggers in

33
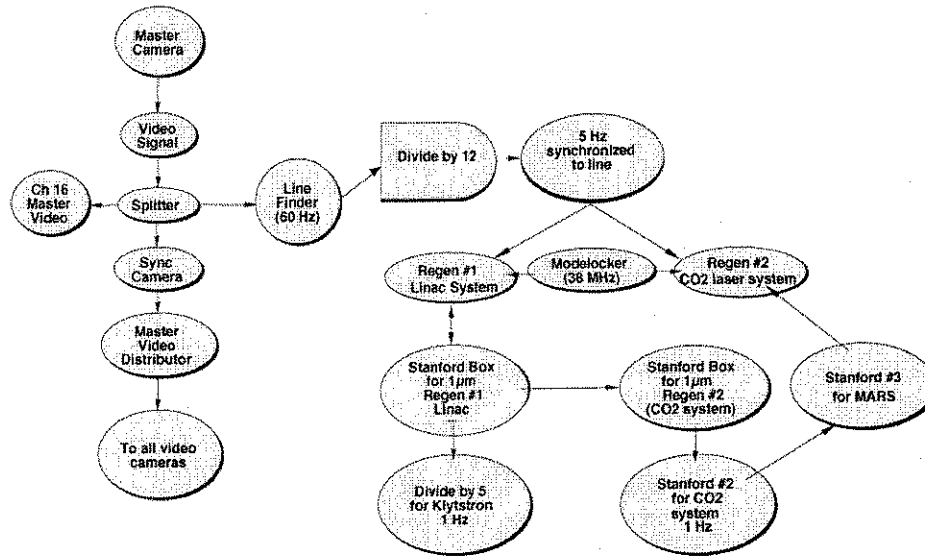
Figure 3.1: A Schematic of the Triggering System.

the experiment to the zero crossing of the AC voltage in the power lines (to ensure that all magnets in the electron beam line are in phase). The 60 Hz trigger signal repetition rate is then divided by a factor of 12 to obtain the 5 Hz repetition rate necessary to trigger the charging and firing of the two 1 μm regenerative amplifiers. Since the firing of the regenerative amplifiers is tied to the 38 MHz mode-locker signal, the whole laser system is synchronized to the zero crossing AC line voltage and the mode-locker signal. The first stage of the optical synchronization process between and the electron bunch and the laser pulse involved using a Hg:Cd:Te detector to look at the signal produced by the low power 10 μm radiation, and a photodiode signal produced by looking at the 532 nm light used to produce the UV on the photo-cathode (the 532 nm light is locked to the electron bunch timing). This allowed nanosecond scale synchronization using both the electronic triggering system and a 7 ns delay line on the 1 μm beam line for semiconductor switching. After timing the two reference signals to within a nanosecond, a second technique for synchronizing

34

the electron bunch and the CO_2 laser pulse within 100 ps at the IP is needed.

3.1.2 Picosecond Synchronization of Electrons and Photons

The picosecond scale synchronization is achieved by overlapping the electron beam and the CO_2 laser pulse on an intrinsic germanium (n-type) sample by using the absorption of the electron beam in the bulk of the germanium. The germanium transmits most of the 10 μm radiation even at normal incidence, but as the electron beam goes through the sample it increases the plasma density inside the sample via collisions with the valance band electrons and eventually the absorption coefficient increases. The general expression for the absorption coefficient is given by Equation 3.1 [25]:

$$K = \frac{16\pi Z^2 n_e n_i e^6 \ln \Lambda(\nu)}{3c\nu^2 (2\pi m_e k_B T)^{3/2}(1 - \nu_p^2/\nu^2)^{1/2}} \tag{3.1}$$

where $\Lambda(\nu)$ is the minimum of $p_{min}v_{th}/\omega_p$ and $p_{min}v_{th}/\omega$ (v_{th} is the electron thermal velocity). In this expression Z is the ion charge, n_i is the ion density, and $p_{min} \cong Ze^2/k_B T$ is the minimum impact parameter for electron-ion collisions (n_e and m_e as usual are the electron density and mass).

In Figure 3.2, the setup for picosecond level synchronization at the IP is shown; a similar setup was used for the f/2 focusing geometry. A cross-correlation trace is obtained using the ratio of the 10 μm radiation transmitted signal (affected by the electron beam) and a reference signal (unaffected by the electron beam) before the germanium slab. To control the CO_2 laser pulse timing, a motorized delay line is used to change the time of arrival of the 1064 nm laser pulse used in semiconductor switching. Another nanosecond scale optical delay line allowed the compensation for nanosecond scale changes in the propagation of the laser pulse. Thus, by variably delaying the arrival time of the low power CO_2 laser pulse relative to the electron bunch a cross-correlation trace is obtained. The cross-correlation traces,

Transmitted Signal

Electron Spectrometer

Surface Barrier Detectors

3-axis probe assembly

Ge slab

Reference Signal in front of lens

E-beam and f/18 beam
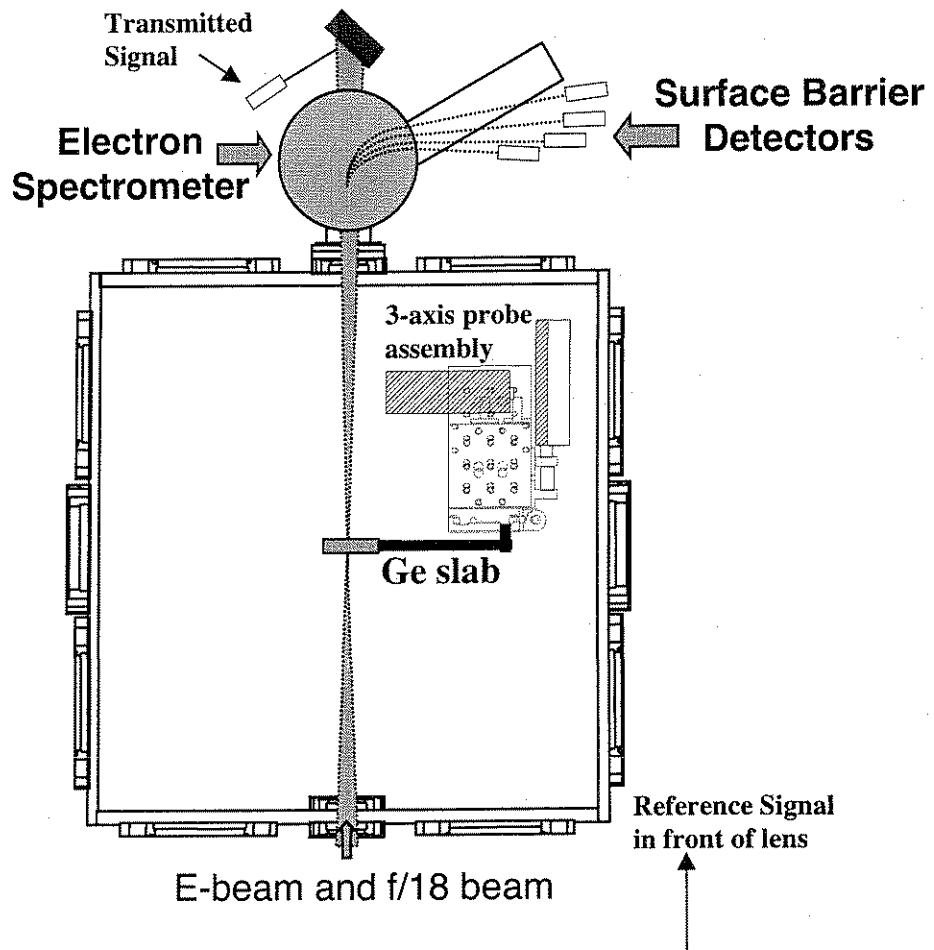
Figure 3.2: Picosecond Synchronization Setup for f/18 Focusing.

shown in Figure 3.3, illustrate the robustness and reproducibility of the setup which gave essentially the same delay settings within ~15 ps over two weeks.

The drawings at the bottom of the figure illustrate the relative timing of the CO_2 laser pulse (long red ellipse) and the electron bunch (shorter blue ellipse). The figure shows that once the laser pulse arrives at the IP before the electron bunch the signal level of the transmitted signal becomes constant. Taking the derivative of curve fit of the data an effective pulse length is obtained for the low-power CO_2 laser pulse (~140 ps FWHM $\gg$ 10 ps for the electron bunch), as well as the delay setting to synchronize with the electron bunch (450 ps on the horizontal scale). To offset the delay introduced by the firing of the MARS amplifier, due to the change in refractive index in an active gain medium, another ~100 ps delay must be added. The final timing between the electron bunch and CO_2 laser pulse was determined by optimizing the accelerated electron energy spectra.

3.2 Electron Spectrometer for the Detection of Accelerated Electrons

The electron spectrometer used for the detection of electrons is a dipole magnet (GMW 5403) powered by a 40 A Sorenson power supply along with a vacuum assembly that allows the electrons to be bent to trajectories from approximately 130°–45° (relative to the incident beam) or 6.5–30 MeV for the Browne & Buechner pole pieces at B=4000 gauss. The spectrometer can be configured to use two different pole pieces that are segments of a circular pole piece. The shape of the segments each have some unique focusing properties. The development and use of this spectrometer is discussed in greater detail in [26]. Both sets of
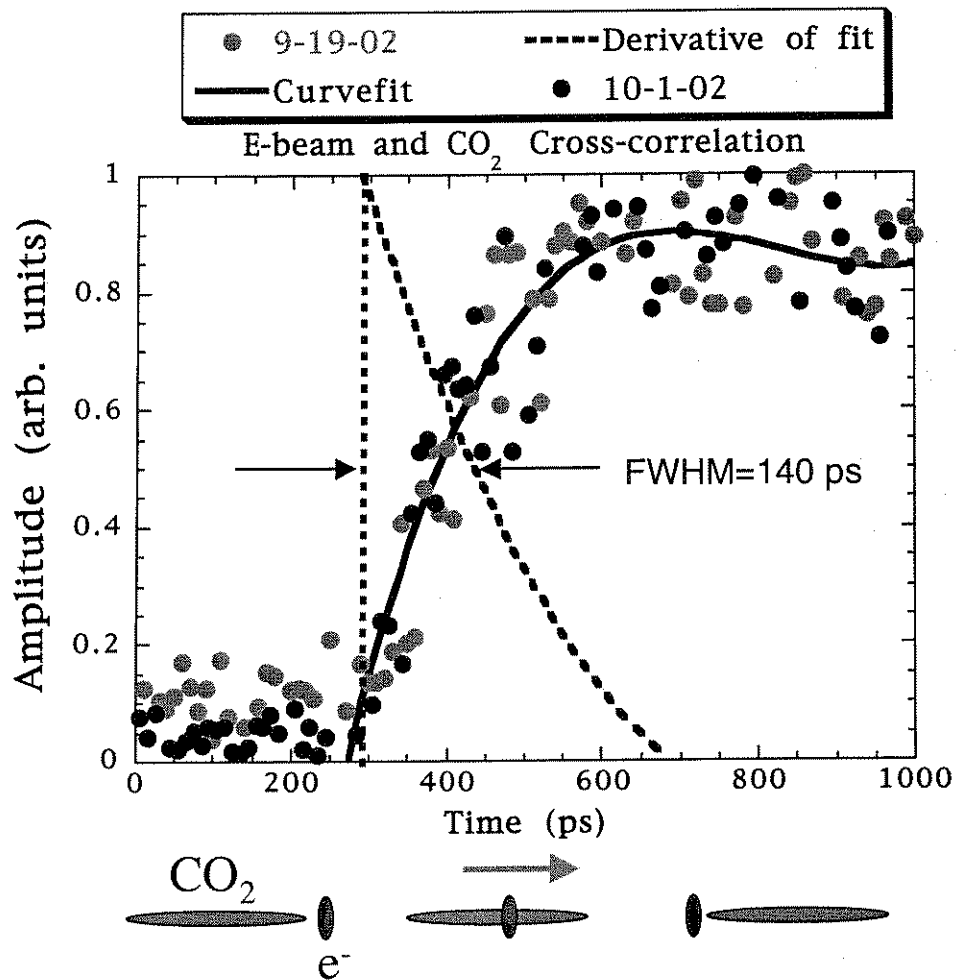
Figure 3.3: Cross-correlation traces obtained between the electron bunch and the CO_2 laser pulse.

pole pieces are used with a pole face rotation of $\sim 11°$, which is measured from the normal of the rear surface of the pole piece and the axis of propagation (see Figure 3.4). This gives more vertical focusing at the exit plane of the vacuum assembly so that the electron beam does not strike the stainless steel edges of the vacuum window near the image plane. The electrons exit the vacuum assembly through a Mylar^{TM} window with a ~ 25 μm thickness and are detected either by biased silicon surface barrier detectors (SBDs) or by a CCD camera looking at the fluorescence of the electrons. The main electron beam (not accelerated) is allowed to exit the vacuum assembly at $\sim 90°$ and strike a weak phosphor (Mylar^{TM} coated with fluorescent paint) before being dumped. The weaker phosphor was primarily used to detect electrons near the electron beam energy injected into the PBWA (E_0); the flux of accelerated electrons is insufficient to produce enough light to allow the detection of electrons at high energies with this phosphor. The accelerated electrons then pass through a 3M TRIMAX phosphor screen (Gadolinium Oxysulfide doped with Terbium, $Gd_2O_2S:Tb$) and cause the screen to fluoresce. The peak fluorescence for this phosphor is near 532 nm (currently available screens are called LANEX and are manufactured by Kodak). The amount of charge striking the phosphor is directly proportional to the light produced; the response is linear for the electron fluxes present in the experiment. This diagnostic is depicted in more detail in Appendix A.

3.2.1 Electron Spectrometer with Switcher Pole Pieces

For the case of f/2 focusing, the electron spectrometer setup uses switcher pole pieces which has more dispersion than the setup with Browne & Buechner pole pieces (approximately 2 times more). In Figure 3.4, the trajectories of the electrons are shown for the switcher pole pieces along with the vacuum assembly and
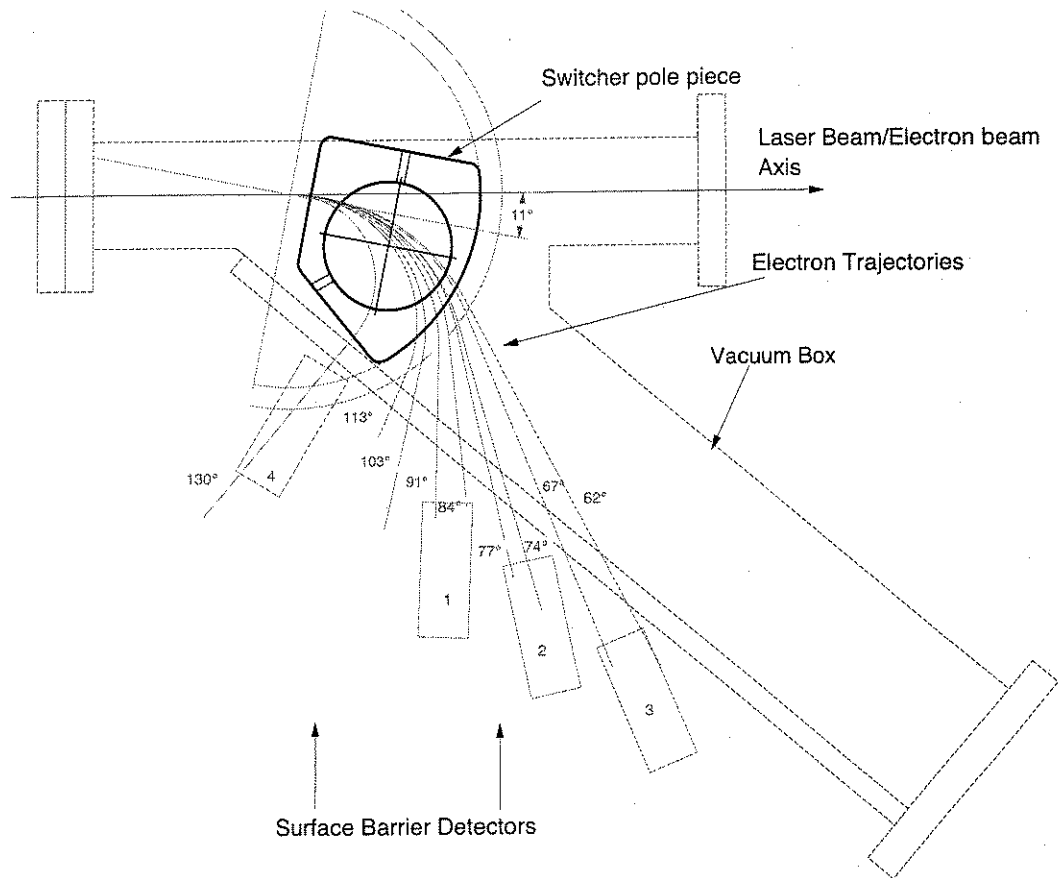
Figure 3.4: A Schematic of the switcher pole pieces with the trajectories of the electrons.
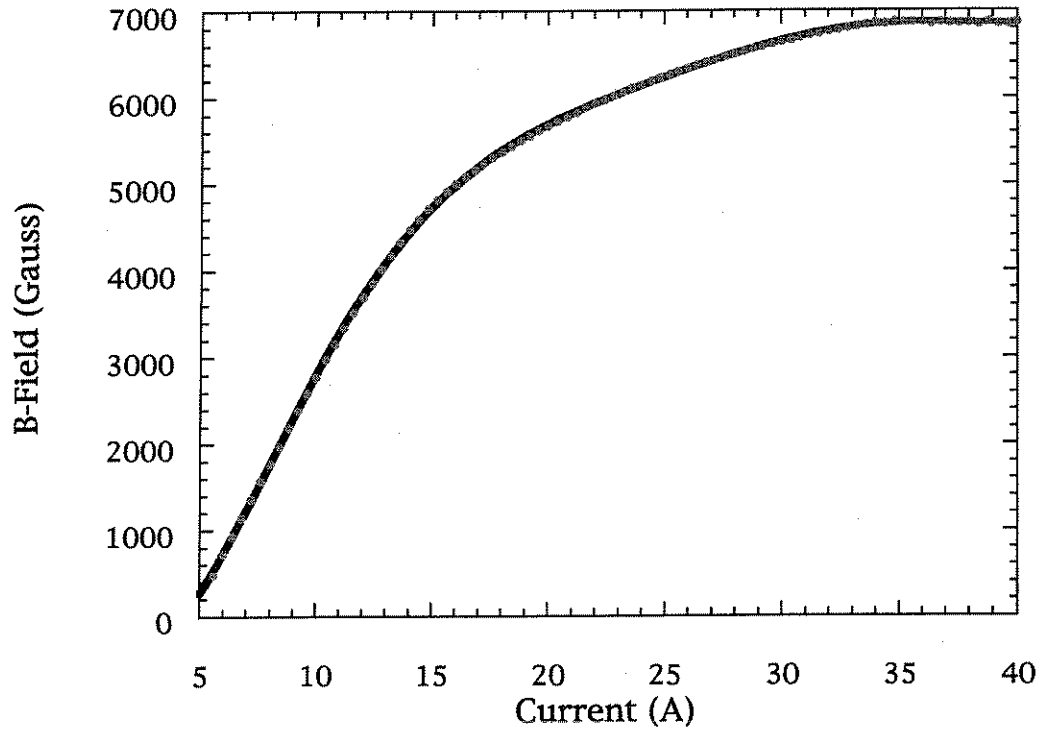
Figure 3.5: A plot of the magnetic field, B (gauss), as a function of the current, I (amperes) using the switcher pole pieces, where the fit to the field is $B(I) = 992.2 - 1073.6I + 280.0I^2 - 23.2I^3 + 0.97I^4 - 2.2 \times 10^{-2}I^5 + 2.5 \times 10^{-4}I^6 - 1.1 \times 10^{-6}I^7$.

image plane of the spectrometer (top view). The gap in the position of the detectors from 90°–115° is to allow a CCD camera and phosphor screen to be used. For the switcher pole piece the field required to bend the electrons a certain angle, θ, is given by:

$$B = \frac{m_e v \gamma \sin \frac{\theta}{2}}{e R_{eff}} \tag{3.2}$$

where R_{eff} is the effective radius of the pole piece, v is the velocity of the electron, and γ is the relativistic factor of the electrons. To achieve the relatively large field requirements to bend the 12.4 MeV electron beam, the nonlinearity in the field amplitude as a function of the power supply current observed with this magnet must be taken into account. In Figure 3.5 the magnetic field versus current, measured using a Hall probe, is plotted and fit to a polynomial function for the switcher configuration. The field saturates because at higher currents the impedance of the coils of the dipole magnet change; it is normally 1.5 ohms. This is partially due to saturation of the magnet iron and also due to an increase in the temperature of the coils of the dipole at higher currents.

The switcher pole piece was used primarily for the f/2 focusing geometry which, due to the relatively small interaction length that it produces, was not expected to produce energy gains beyond ~30 MeV. In Figure 3.6, the energy in each electron trajectory is plotted from Equation 3.2 for a fixed field value of ~4500 Gauss, which is the required magnetic field to bend the 12.4 MeV electron beam 90° for the switcher pole piece.

3.2.2 Electron Spectrometer with Browne & Buechner Pole Pieces

The acceleration experiments with the f/18 focusing geometry produces a long interaction region and utilizes the Browne & Buechner pole pieces to allow for the maximum energy range for the observation of accelerated electrons. In Figure
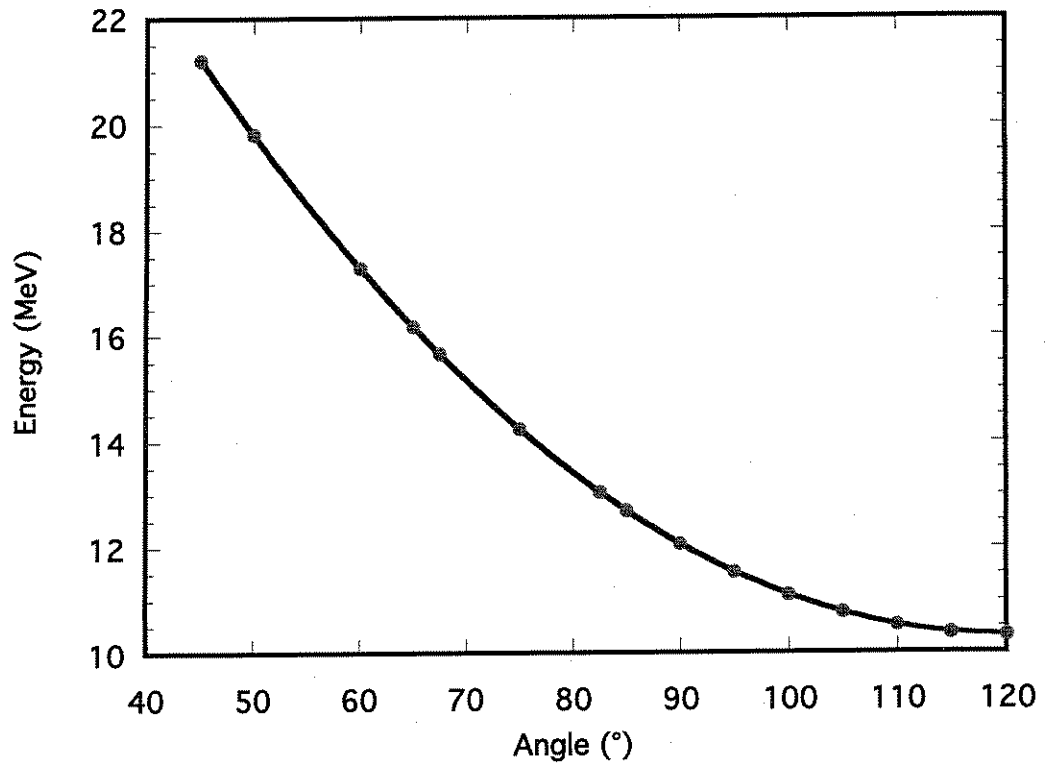
Figure 3.6: A plot of electron energy versus angle of the electron orbit for the switcher pole piece with 12.4 MeV beam on 90° orbit (obtained from Equation 3.2).

3.7, a mechanical drawing and schematic of the trajectories of the electrons is presented for the Browne & Buechner Pole Pieces (top view). The dashed circle in the drawing represents parent pole piece that defines the virtual source for the electron orbits. After the electrons exit the field boundary the trajectory of the electrons follow a path that is equivalent to the electrons originating from this virtual source. The expression for the required magnetic field for this case is:

$$B = \frac{m_e v \gamma \tan \frac{\theta}{2}}{eR_{eff}} \tag{3.3}$$

where the constants in this expression are the same as in Equation 3.2. The change in the expression from sin to tan is due to the difference between the transfer matrix for the switcher and the Browne & Buechner pole pieces. Details about the transfer matrix for different types of deflecting magnets can be found in [27]. In Figure 3.8, the magnetic field versus current is plotted and fit to a polynomial function. In Figure 3.9, the energy in the electron trajectories obtained from Equation 3.3 is plotted for a magnetic field value of ~4000 Gauss which is required to bend the 12.4 MeV electron beam 90° for the Browne & Buechner pole pieces.

Appendix A presents more details describing the silicon surface barrier detector setup as well as information about the CCD camera and phosphor screen diagnostic. There is also a synopsis of the data acquisition system used for collecting SBD and CCD image data at the exit of the electron spectrometer. The description in Appendix A outlines all of the SBD configurations used in both sets of acceleration experiments and the X-ray shielding used.
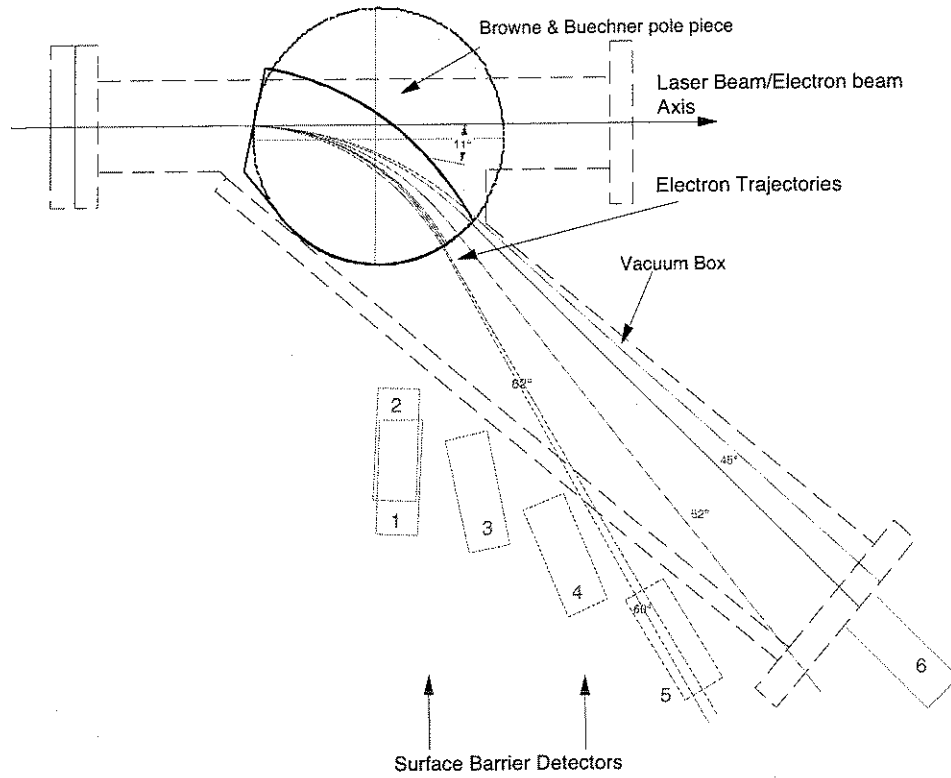
Figure 3.7: A Schematic of the Browne & Buechner pole pieces with the trajectories of the electrons.
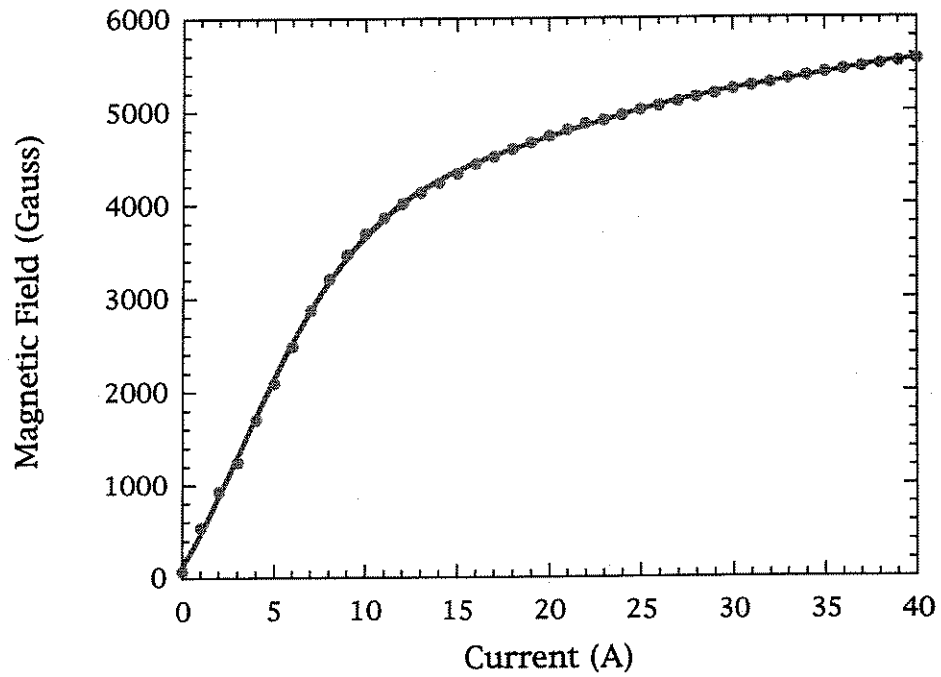
Figure 3.8: A plot of the magnetic field, B (gauss), as a function of the current, I (amperes) using the Browne & Buechner pole pieces, where the fit to the field is $B(I) = 121.6 + 303.4I + 50.5I^2 - 8.3I^3 + 0.50I^4 - 1.6 \times 10^{-2}I^5 + 2.4 \times 10^{-4}I^6 - 1.5 \times 10^{-6}I^7$.
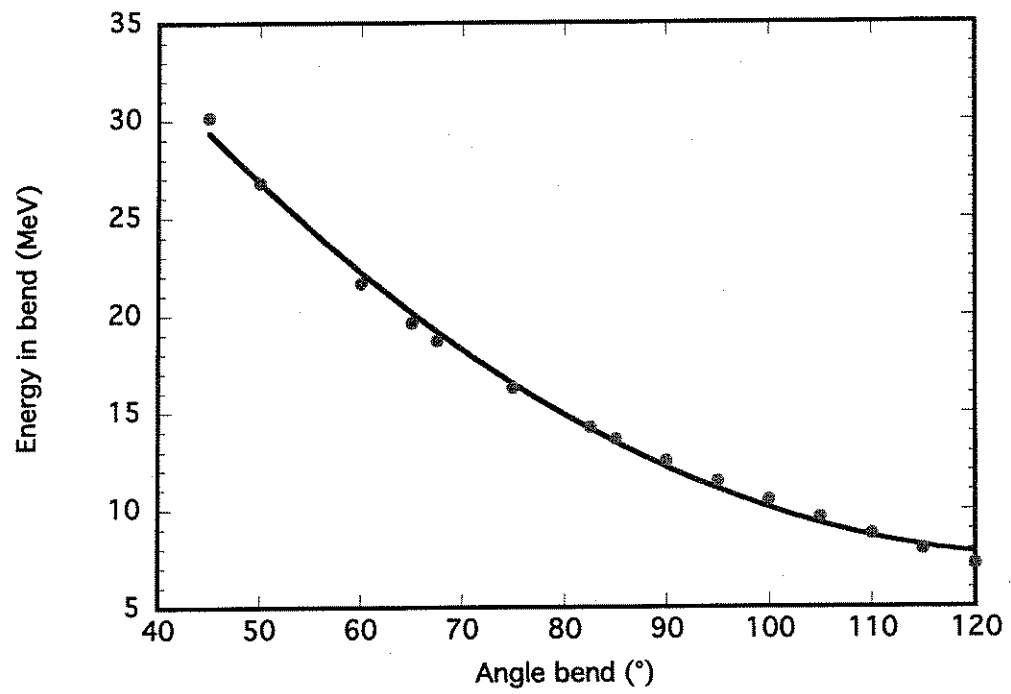
Figure 3.9: A plot of electron energy versus angle of the electron orbit for the Browne & Buechner pole piece with 12.4 MeV beam on 90° orbit.

3.3 Acceleration of Electrons for the f/2 Focusing Geometry

3.3.1 Effect of transverse fields on electron acceleration results

The acceleration results of electrons for the f/2 focusing geometry are greatly complicated by the large transverse electric fields produced in the plasma at the IP. Since the laser beam has a finite transverse extent, the plasma wave is not a plane wave and has radial components. As the electrons are accelerated they are both focused and defocused by the transverse fields of the plasma wave. Also, any misalignment between the laser beam and the electron beam can lead to a severe deflection of the beam as it exits the plasma wave. To reduce the blow-out of the electron beam after the plasma, an aperture was placed along the beam line prior to the location where electrons enter the magnetic field of the dipole magnet. Figure 3.10 shows two 8-bit CCD images of the electron beam as it goes through the $\sim$1 cm diameter circular lead aperture located before the magnet and that has a TRIMAX phosphor on one surface. The picture in Figure 3.10(a) shows that without the plasma the electron beam is fairly round and that a majority of it passes through the hole, but with the laser produced plasma the transverse blow-out of the electron beam deflects a large portion of the electron beam and less electrons pass through the aperture. Other shots show gross, nearly symmetric, defocusing of the electron beam on this screen.

The lead aperture was effective in reducing the beam size through the vacuum assembly of the electron spectrometer since the size of the electron beam must be limited to prevent it from striking any metal surfaces and producing X-rays that would flood the signals on the surface barrier detectors (SBDs). As a result the collection angle for the electrons was limited and meant that only the electrons

within a $\sim 1°$ cone from the IP could be observed at the exit plane of the electron spectrometer (each SBD has a clear aperture of ~ 8 mm).

3.3.2 Accelerated Electron Data for the f/2 Focusing Geometry

The next set of images, in Figure 3.11, are from the 12-bit Star1 CCD camera looking at the two phosphor screens near E_0 exiting near 90° (see Appendix A), Figure 3.11 and illustrate that the large transverse fields at the IP also affect the electron beam at the exit of the electron spectrometer. For this particular set of experiments the incoming beam energy was approximately 11.3 MeV. In the presence of the plasma the brightness of electron beam increases slightly since many of the electrons are deflected vertically downwards for this laser shot, but otherwise no clear signs of electrons being accelerated are observed. Both images show a large number of X-rays striking the surface of CCD camera and the image for the shot with plasma also has some background stray light produced by the laser. The SBD signals, which are used to detect higher energy electrons, could also be affected by the blow-out of the electron beam since a significant number of electrons striking metal surfaces within the vacuum assembly might cause a spurious signal increase due to the sensitivity of the SBDs to X-rays. This makes differentiating X-ray noise on the SBDs from electron signals difficult. In Table 3.1 the settings and sensitivities for the SBDs is presented along with the amount of copper shielding used in front of each detector. The copper shielding provides a filter to absorb any low energy X-rays ($E_{ph} < 50$ KeV) that may strike the detectors. Appendix A describes the attenuation of X-rays and electrons in copper and shows that only the high energy X-rays ($E_{ph} > 100$ KeV) are transmitted by the copper shielding. In the following, the central energy that each SBD is detecting is given relative to the incoming electron beam energy of
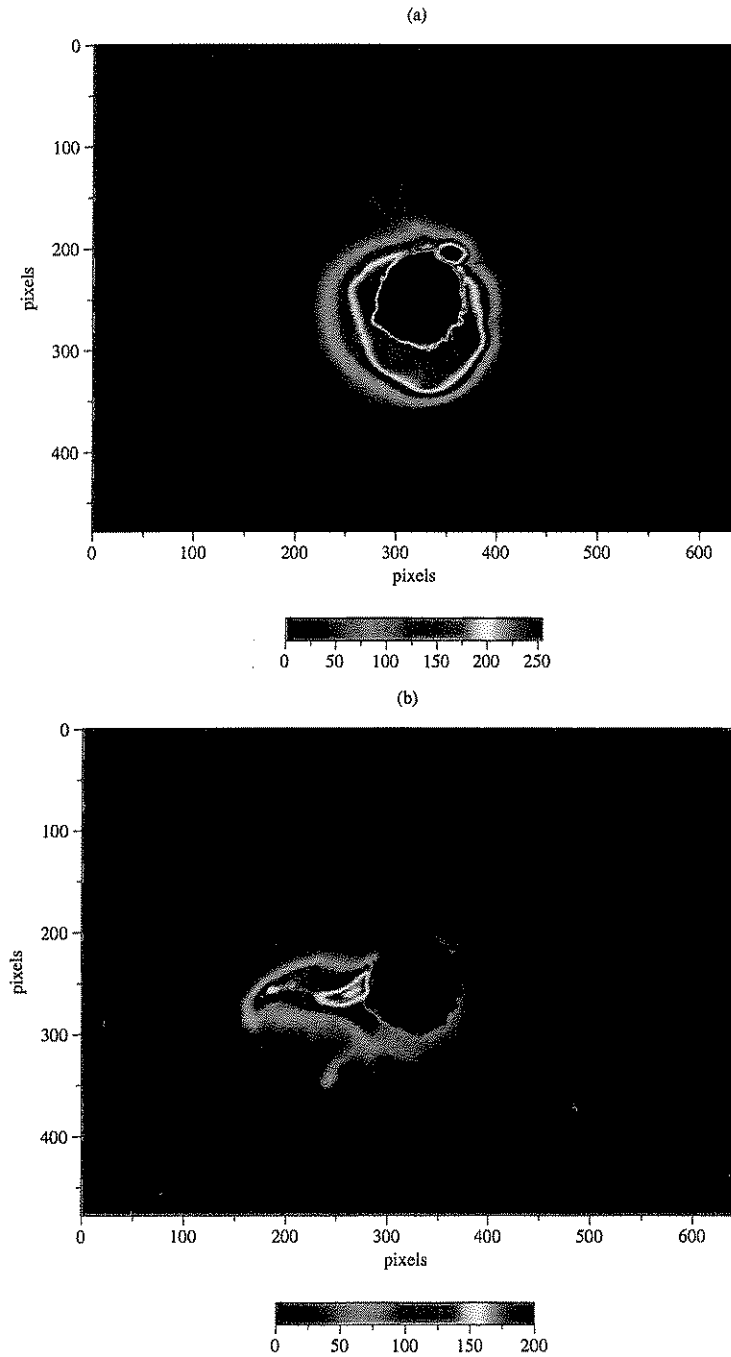
Figure 3.10: Electron beam images on a ∼1 cm lead aperture with a phosphor, (a) without the laser/plasma and (b) with the laser/plasma (MARS shot number 11713).

Detector	mV/e^-	Preamp.	Cu (mm)	MeV (E_0@90°)
1	0.025	113	1.0	11.9
2	0.025	113	1.0	12.7
3	3.57	142	3.0	13.3
4	0.025	113	1.0	8.3

Table 3.1: Surface Barrier Detector Settings for acceleration experiments with f/2 focusing geometry.

~11.3 MeV.

In Figure 3.12 plots of the raw signal on each detector (in mV) for each shot for the f/2 acceleration experiments are shown. The signal levels for the SBDs with the laser fall well within the shot to shot fluctuations of the background signals plotted for electron beam shots without firing the laser. Therefore no accelerated electrons were observed with this focusing geometry. The small collection angle for this set of experiments may be the limiting factor in the detection of accelerated electrons. Although the most energetic electrons would remain on axis with the main electron beam, the accelerated particles that are of interest may be imparted a transverse momentum large enough to prevent their detection. The simulation results presented in the following chapter will give more insight into this effect. The simulations will also illustrate that the transverse fields also cause significant blow-out of plasma and eventually lead to the collapse of the plasma wave, thereby hindering the acceleration process.
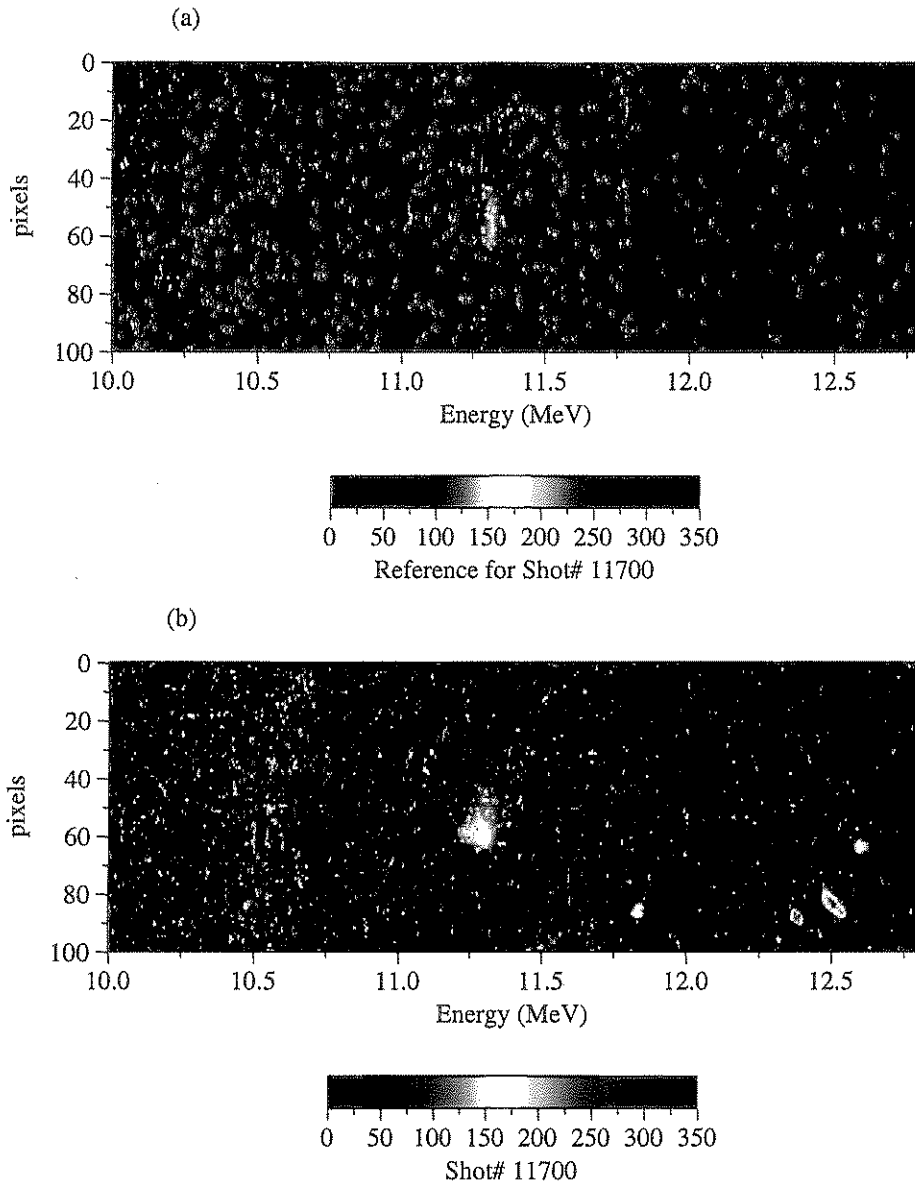
Figure 3.11: 12-bit CCD images of the electron beam near E_0, (a) without the plasma and (b) with the plasma (MARS shot number 11700).
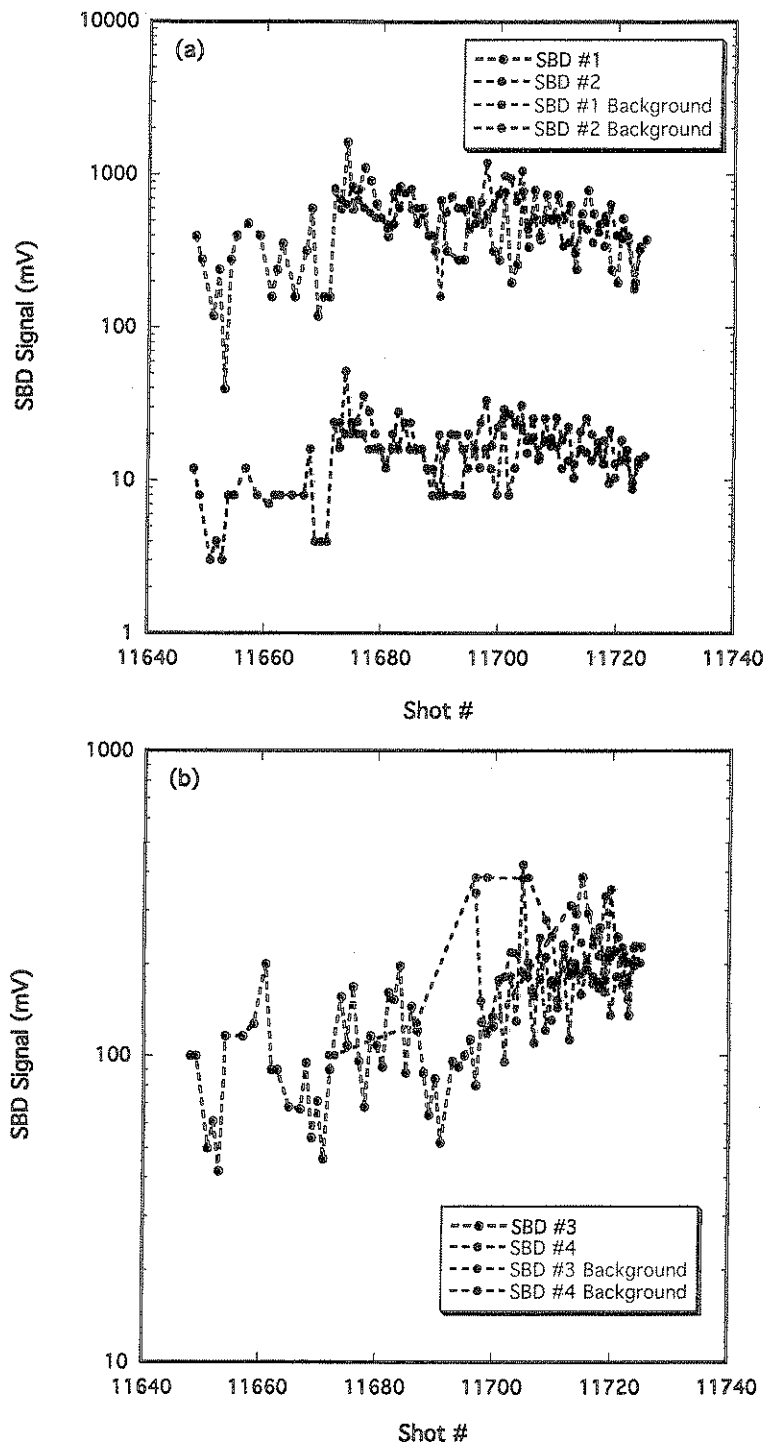
Figure 3.12: SBD data for acceleration experiments for the f/2 focusing geometry.

3.4 Acceleration of Electrons for the f/18 Focusing Geometry

3.4.1 Effect of refraction of the f/18 laser beam by the plasma

The transverse effects that arose in the experiment with the f/2 focusing geometry described in the previous section, were not as large an issue for the experiments with the f/18 focusing geometry. However, the effect of ionization induced refraction did play a significant role in the way the experiments were done as well as in the results that were obtained. This is partly due to the significantly larger spot size of the laser beam at the IP (see Table 2.1) for these experiments, and to the smaller v_{osc}/c which implies smaller transverse electric fields. Figure 3.13 shows images of the plasma along the propagation axis of the CO_2 laser beam. In Figure 3.13, it is clear that high power focus of the laser has shifted and that for higher pressures more of the laser is refracted (the MARS shot numbers for these images are given in Figure 3.14). Figure 3.14 shows the sum of longitudinal lineouts of some of the plasma images in Figure 3.13 which show that the overall length of the plasma is also affected by the amount of refraction taking place. The peak of the laser-field has shifted approximately $2Z_R$ or ~ 2.5 cm upstream with respect to the beam waist in vacuum. This refraction appears to limit the amount of laser power that can be involved in driving the plasma wave especially for shorter pulse durations ~ 120 ps. For the longer laser pulses, ~ 400 ps, the transverse motion of the ions produces a density channel which acts to guide the laser beam. Thus, although the early part of the laser pulse is refracted due to ionization, the later part of the laser pulse can be guided toward the vacuum focus where it can ionize the gas and therefore produce a longer plasma. When a two-frequency ~ 400 ps laser pulse is used, it can produce a longer relativistic
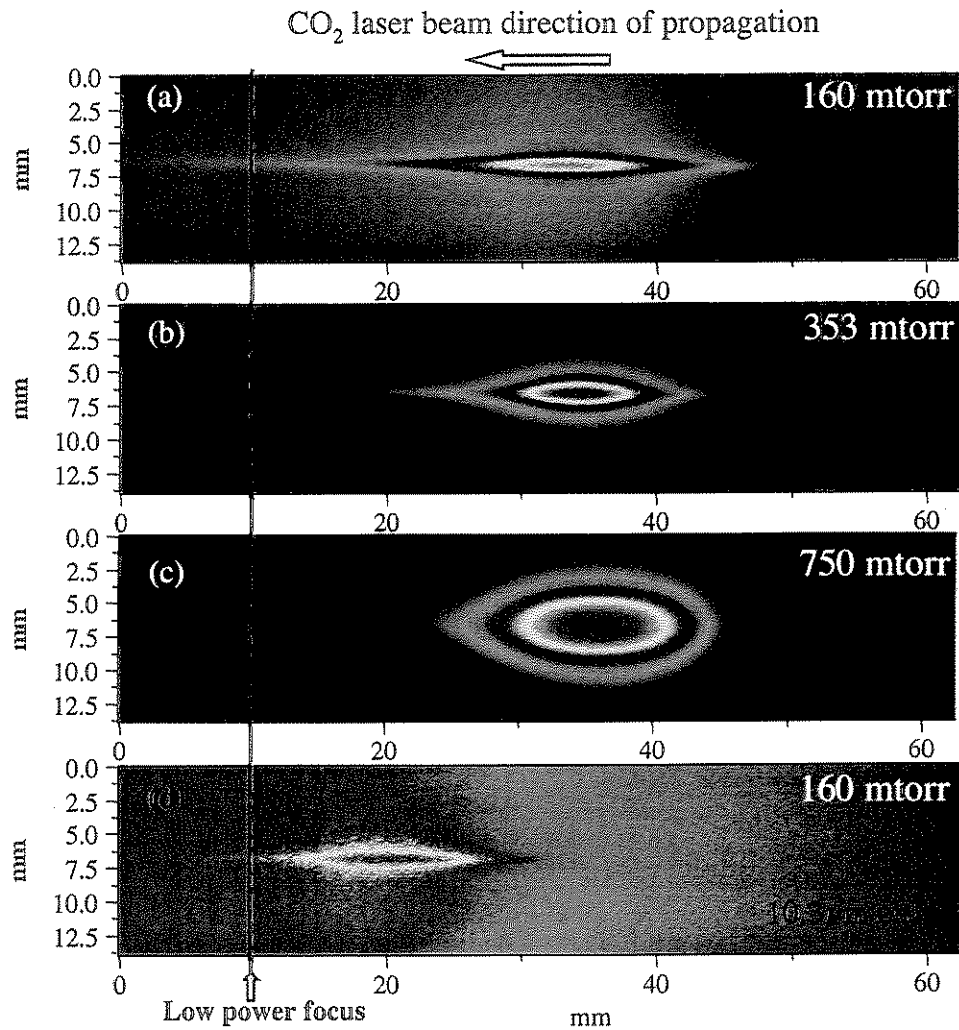
Figure 3.13: Refraction of the laser pulse in hydrogen for f/18 focusing with a two-frequency laser pulse with beat-wave excitation at (a) 160 mtorr, (b) 353 mtorr, (c) 750 mtorr, and (d) at the same pressure as (a) but with a single frequency laser pulse and no beat-wave excitation.
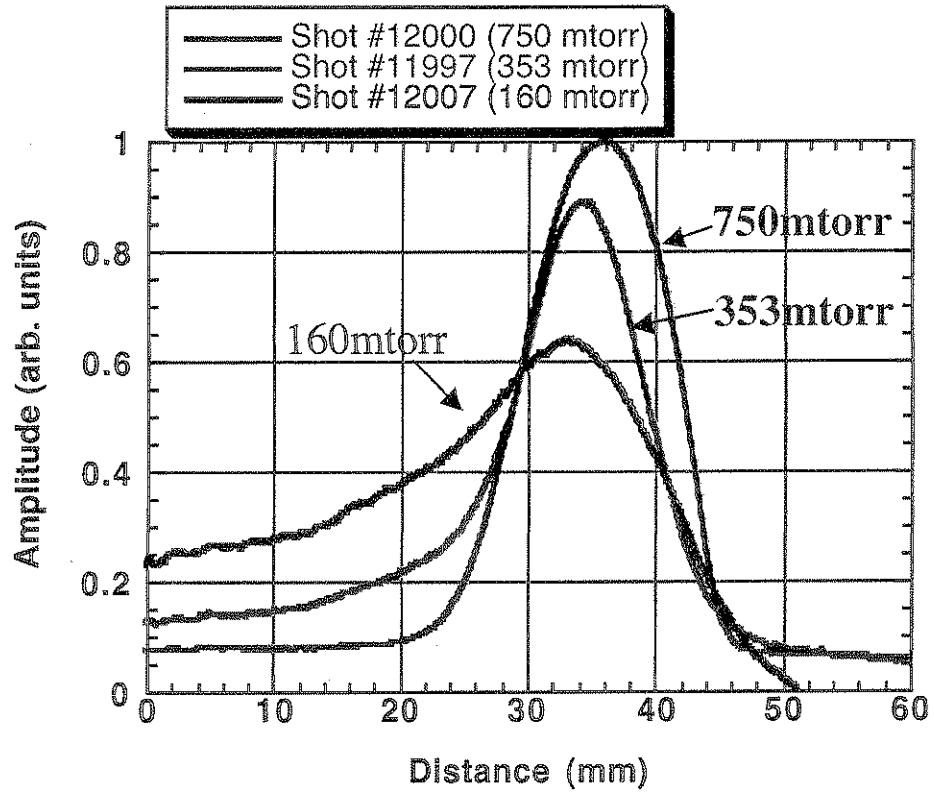
Figure 3.14: Lineouts of plasma images illustrating the refraction of the laser pulse.

plasma wave than can a shorter pulse. This is verified by simulations presented in the next chapter. The acceleration results presented in the next section are for pulses ~400 ps in duration and show accelerated particles out to ~50 MeV (energy gains of up to 38 MeV); the results for the ~120 ps pulses achieved energy gains of only ~10 MeV (not shown here).

3.4.2 Accelerated Electrons Data for the f/18 Focusing Geometry

The experimental results presented for the f/18 focusing geometry were obtained using the Browne & Buechner pole pieces allowing for the collection of electrons in an energy range larger than that for the f/2 acceleration experiment (see Figure 3.9). There are smaller transverse fields associated with this focusing geometry, since the transverse deflections of the beam were significantly reduced, the aperture shown in Figure 3.10 to limit the amount of blow-out of the electron beam was not needed. Also, an additional permanent focusing quadruple magnet was added after the IP to slightly reduce the electron beam size without losing any electrons (compensating for any possible blow-out of electrons). This allowed the collection cone angle to be slightly larger, ~2°, effectively increasing the number of lower energy electrons that could be collected (the higher energy particles propagate closer to the axis of propagation), and also reduced the spurious SBD signals due to X-rays. In Figure 3.15, phosphor images of the accelerated electron spectra near E_0 are presented; E_0 is ~12.4 MeV for this set of experiments. The black dots visible on the left side of the two images indicates the position of the 90° orbit. Note that the X-ray background level in these images is significantly less than the images shown in Figure 3.11. From Figure 3.15 it is also clear that electrons are accelerated and that the main electron beam at E_0 is not significantly perturbed transversely. A calibration of the phosphor allowed for

Det.	mV/e^-	Preamp.	Cu (mm)	MeV(E_0@90°)	MeV(E_0@120°)	θ
1	0.025	113	1.0	Noise Ref.	Noise Ref.	82.5°
2	0.025	113	1.0	14.0	24.5	82.5°
3	3.57	142A	3.0	16.6	28.6	75°
4	0.025	113	1.0	18.2	31.3	70°
5	3.57	142A	1.0	22.0	37.7	60°
6	3.57	142A	2.0	27.4	47.2	48°
7	3.57	142A	2.0	30.0	50.0	46°

Table 3.2: Surface Barrier Detector Settings for acceleration experiments with the f/18 focusing geometry.

the estimation of the number of electrons measured per unit area based on the number of counts within that portion of phosphor. The calibration used is $\sim$230 electrons/mm^2 for 1.0 counts/mm^2. This was also used to calibrate the amplitude of the electron spectrum obtained from the SBD data. Note that electrons at energies higher than $\sim$13.5 MeV are too few to be detected using the sensitivity (compared to the SBDs) phosphor screen.

In Table 3.2 the sensitivities and copper attenuation for each detector are given, along with the energy the detector is centered on. By increasing the field on the dipole magnet higher energy electrons could be detected. In general data was taken with the incoming electrons at E_0 exiting the spectrometer at 90° and then exiting at 120° so that electron with energies as large as 50 MeV could be measured on the last SBD. The gas corresponding to a resonant density ($\Delta\omega=\omega_2-\omega_1=\omega_p$) was determined from the maximum of the Thomson scattering signal [23]. The resonant pressure determined was $\sim$165 mtorr using that method. This was also determined by varying the gas pressure and observing the signal
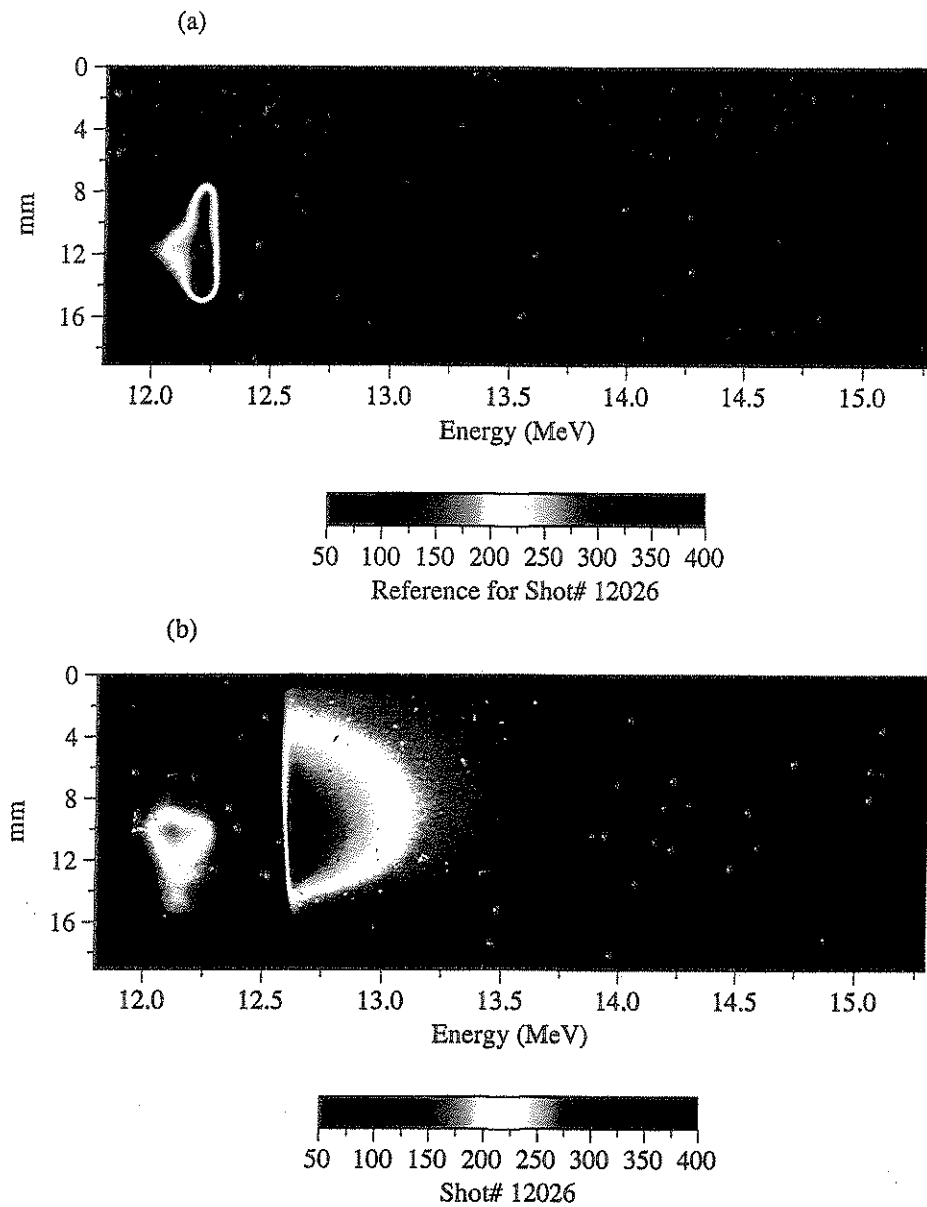
Figure 3.15: 12-bit CCD images of the electron beam near E_0, (a) without the plasma and (b) with the plasma (MARS shot number 12026).
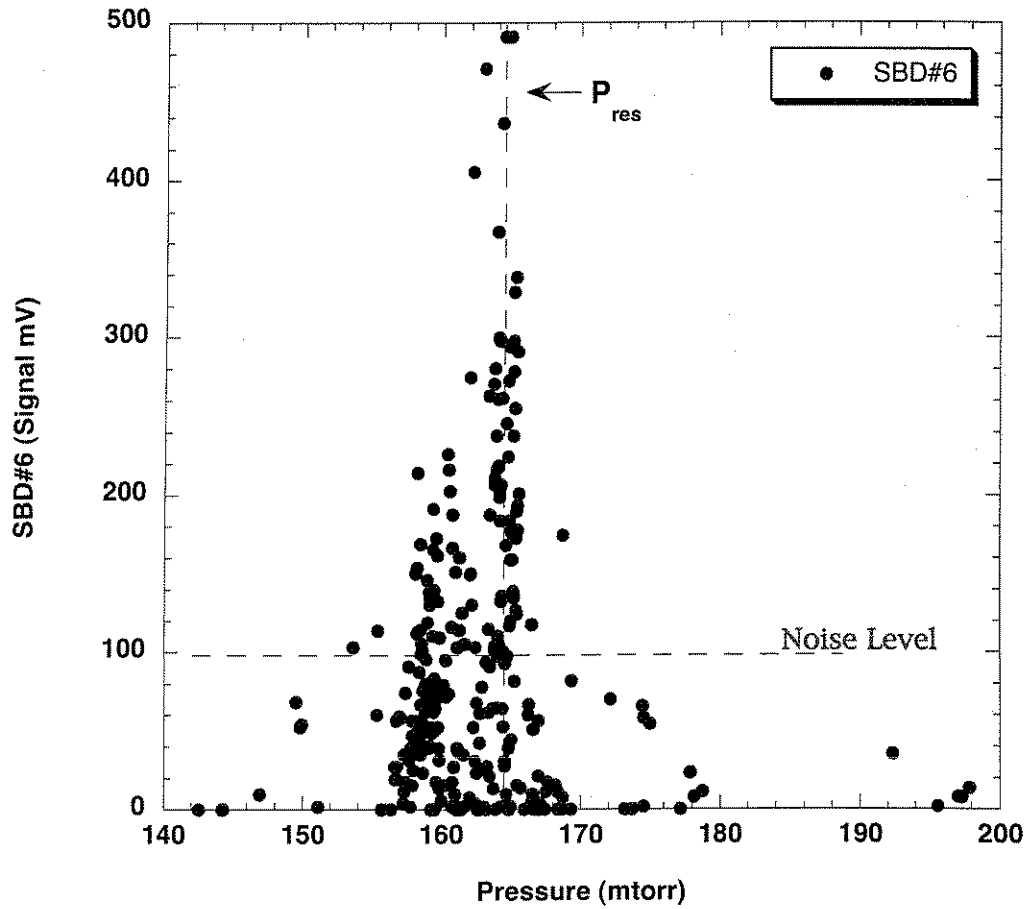
Figure 3.16: Resonant density as determined by the raw SBD signal at E=27.4 MeV.

on an SBD measuring electrons at high energy. The SBD signal as a function of pressure is shown in Figure 3.16, indicating that the resonant pressure is $\sim$164 mtorr, and in good agreement with value determined from Thomson scattering. Figure 3.17 gives single-shot accelerated electron spectra with both field settings (E_0 at 90° and at 120°), and electron data from the phosphor and SBDs. The number of electrons accelerated per MeV is obtained from the detector size and dispersion of the spectrometer as shown in Figure 3.9. The arrows on the plot indicate that on these shots the SBD signal was saturated and that the real signal should be higher the measured values. This spectrum shows that electrons are accelerated out to $\sim$50 MeV over a distance of $\sim$2.5 cm ($2Z_R$). The corresponding accelerating gradient is therefore $\sim$1.5 GeV/m leading to a normalized wave amplitude of 0.15 $mc\omega_p/e$. The simulation results in the next chapter will provide a comparison for these experimental results and are in good agreement.

3.5   Conclusions on Acceleration Results

The acceleration results from both focusing geometries illustrate two common concerns associated laser acceleration of particles: transverse field effects on the accelerated electrons and refraction of the ionizing laser beam. The acceleration results with the f/2 focusing geometry are characterized by the strong transverse fields of the plasma wave, while the results for the f/18 focusing geometry are limited by the refraction effects on the laser intensity and plasma wave amplitude. Any experiment designed to achieve the highest level of acceleration must take both of these effects into account. The advantages of plasma accelerators is that the high field requirements reduce the interaction length needed to achieve large energy gains, but as demonstrated, other effects may limit the acceleration process. For the CO_2 laser driven PBWA case, the relatively small wave amplitude
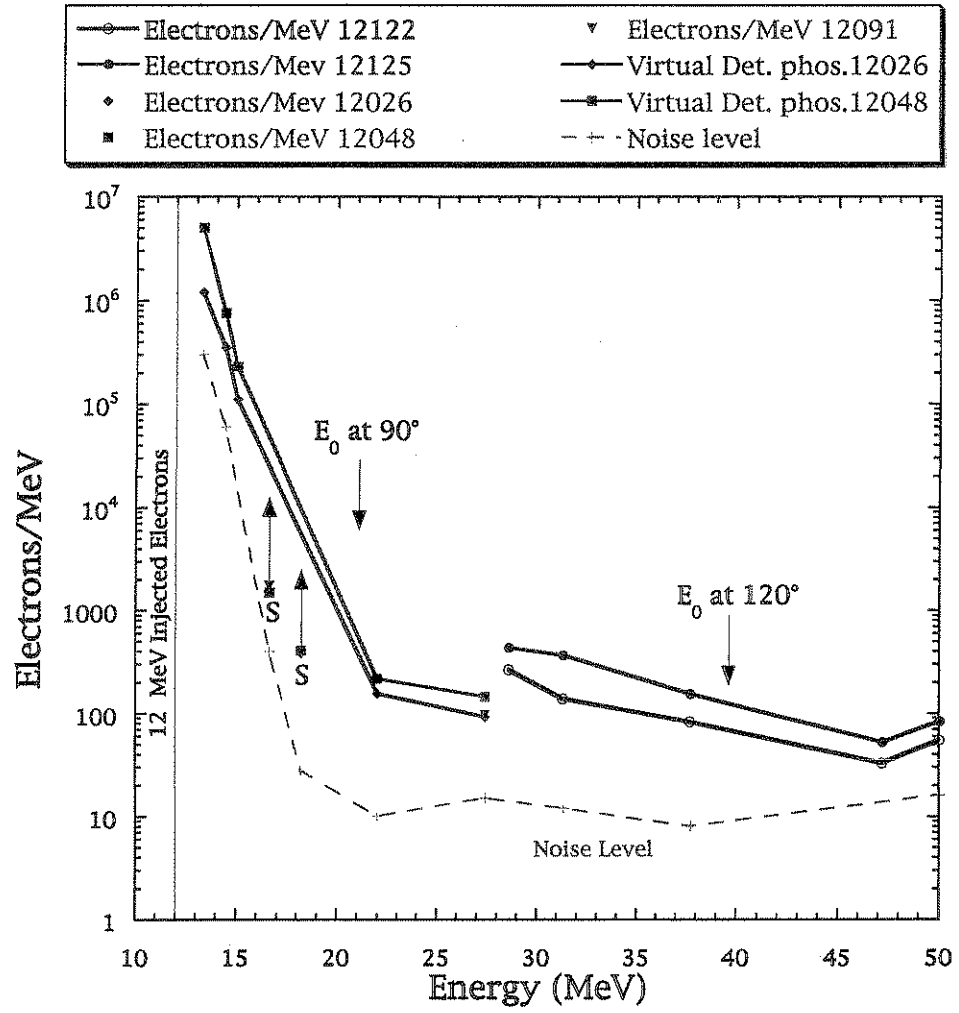
Figure 3.17: Accelerated electron spectrum in Electrons/MeV.

provides a good accelerating structure to inject an external electron beam. Good beam quality is also possible for a 10μm long electron bunch, since $\lambda_p \approx 340$ μm. To produce a large amplitude and uniform accelerating gradient it is generally important to have pulses short enough so that ion motions can be neglected, but long enough to drive a large amplitude wave. For the f/18 focusing geometry long beat-wave excited plasmas were observed >2.5 cm in length, and the energy gain of the injected electrons, $\sim$38 MeV, is the largest produced by a PBWA (corresponding to a gradient of $\sim$1.5 GeV/m). In past experiments the study of ionization induced refraction showed that it played a significant role in the propagation of laser beams [10]. The next chapter will present simulation results that correlate well with the results of and the effects observed in the experiment.

CHAPTER 4

Numerical Simulations of f/2 and f/18 Focusing Geometries for Electron Acceleration

4.1   Introduction

The PBWA experiment in the Neptune Laboratory [28] has been modeled using the particle-in-cell (PIC) code TurboWAVE [4] in a 2-D slab geometry. This code allows 2-D modeling of the experimental parameters present in the lab, and uses a ponderomotive guiding-center model to describe the excitation of the plasma wave. This allows simulating laser pulses hundreds of picoseconds in length without have to explicitly resolve the laser frequency, greatly reducing computation time. TurboWAVE uses ADK theory [29] to model the ionization process which is used for all of the 2-D simulations presented here. The propagation of relativistic electron beams inside of relativistic plasma waves is also simulated using TurboWAVE. The parameters presented in Table 2.2 are taken into consideration in modeling the injection of electrons into the plasma wave. The simulations were done using the IBM SP2 at NERSC (National Energy Research Computing Center). Simulations were performed for conditions present in the laser-plasma acceleration experiments: $\sim$120–400 ps laser pulses for both f/2 and f/18 focusing optics with intensities of $\sim 10^{15}$ W/cm^2 and $\sim 2\times 10^{14}$ W/cm^2, respectively (with the beat-pattern at $\Delta\omega = \omega_2 - \omega_1$ corresponding to 10.275 μm 10.591 μm).

64

In the acceleration experiments the separation of the two laser frequencies was approximately equal to the plasma frequency ($\Delta\omega \approx \omega_p$) and the effects of relativistic detuning resulted in a somewhat higher resonant density (see Chapter 1). From the simulations the normalized relativistic plasma wave amplitude, E_z, can be determined. Determination of the wave amplitude allows the estimation of the magnitude of acceleration expected for electrons that are externally injected into the plasma wave. In general for 1-D theory the longitudinal field gradient is $\sim n_0^{1/2}$ V/cm, where $n_0 = 9.4 \times 10^{15}$ cm^{-3} is the resonant density. The maximum energy gain is given by [1]:

$$W_{max} = E_z \cdot L, \qquad\qquad (4.1)$$

where L is the length over which the accelerating gradient is excited.

Simulations have also been done in 1-D to determine optimum conditions for 2-D simulations. From the 1-D simulation results a plot of the plasma wave amplitude as a function of the background plasma density gives a resonance curve similar to past analytical results [16]. This curve is presented in Figure 4.1 and illustrates that the peak wave amplitude is reached at a density, $n = 1.14n_0$, which is slightly larger than that corresponding to the beat frequency; partly due to relativistic detuning. This value for the resonant density corresponds closely to the resonant pressure shown in Figure 3.16. Simulations performed at densities above resonance, without ion motions included, showed that the response at the driven frequency is significantly smaller than that at resonance. In those cases the forward Raman scattering instability is observed and the plasma wave is modulated at ω_p.

Initially 2-D simulations were done using stationary ions (not presented here), but it was clear from the experimental results that for the larger v_{osc}/c and longer pulse lengths ion motions must be included in the simulations; for both f/2 and
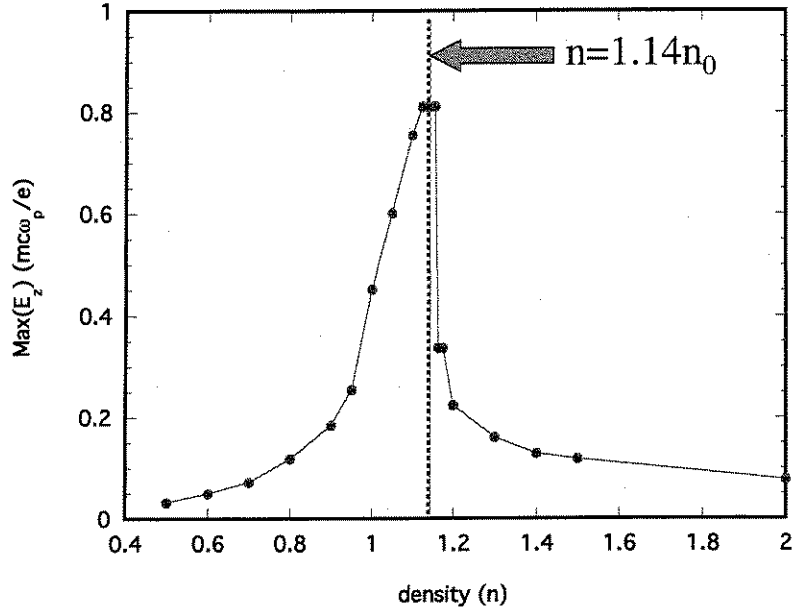
Figure 4.1: Resonance curve for 1-D beat-wave simulations.

Run	$w_0(c/\omega_p)$	$dx(c/\omega_p)$	$dz(c/\omega_p)$	$dt(\omega_p^{-1})$	x×z-cells	Steps	$\alpha_{1,2}$
f/2	1.0	0.1	0.1	0.05	128×1024	10,000	0.3
f/18.1	4.0	0.1	0.05	0.025	256×4096	20,000	0.1
f/18.2	4.0	0.1	0.05	0.025	512×16384	90,000	0.1

Table 4.1: Beat-Wave Simulations for Neptune Parameters

f/18 focusing geometries. When ion motion is included, the Raman scattering instability does not grow as it does when ions are immobile. This is due in part to the fact that as the ions move, the local plasma density changes, thereby suppressing the growth of the instability by detuning the excitation. The reverse situation has also been shown where Raman scattering suppresses plasma blow-out [30, 31]. This situation arises mainly for shorter laser pulses or when v_{osc}/c is $\ll 1.0$, i.e. when ion motions can be neglected.

Table 4.1 gives the relevant parameters for the simulations presented in this

chapter, where runs f/2 and f/18.1 correspond to a total time of $\sim$90.0 ps each ($c/\omega_p \approx 53$ μm and $\alpha_{1,2}$ is normalized to $mc\omega_L/e$) and f/18.2 corresponds to a time of $\sim$400 ps. All of the simulations presented here had 16 particles per cell for each species. A laser rise-time and fall-time of $275\omega_p^{-1}$ ($\sim$50 ps) is used for the f/2 and f/18.1 simulations and the frequency ratios are taken to be ω_1/ω_p=31 (10.591 μm) and ω_2/ω_p=32 (10.275 μm). A rise-time of 80 ps and a hold time of 320 ps was used for the f/18.2 simulation to model the longer pulses that led to the largest electron energy gain of $\sim$38 MeV in the experiment. In all cases the laser propagates in the z-direction with x as the transverse coordinate. The simulation window in the f/18.1 case is twice the length of the f/2 box, therefore the focus is reached on a later time step (the focus is placed at the center of each simulation window). The Rayleigh range, $2Z_R \approx 2\pi w_0^2/\lambda$, is $\sim$1.6 mm for f/2 focusing with a simulation box that is $\sim$5 mm, while for the f/18 cases $2Z_R \approx$2.5 cm. To model the f/18 experiment simulation boxes that were $\sim$1 cm and $\sim$4 cm in length were used for runs f/18.1 and f/18.2 respectively. In the case of the f/18.2 run, test electrons were injected with a relativistic factor of $\gamma \approx 23$ over two successive accelerating buckets in the plasma wave.

4.2   2-D PIC simulation results for the f/2 case

Figures 4.2–4.5 present four important quantities for the f/2 simulation (the laser propagates from left to right in all of the figures presented here). Figure 4.2 shows a plot of the square of the normalized laser vector potential, α^2, and a line-out along the axis of propagation, both in units of $(mc\omega_L/e)^2$. It shows the beat pattern produced by the two laser frequencies and that the focus of the laser beam is at the center of the simulation window. In Figure 4.3, a plot of E_z normalized to the cold wave-breaking amplitude, $mc\omega_p/e$, and a line-out along

67

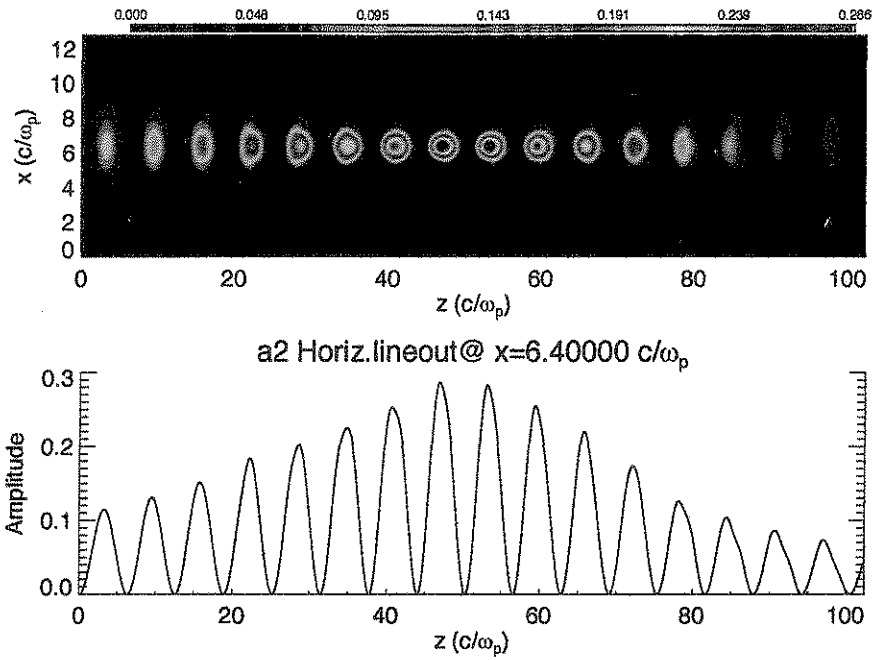Figure 4.2: α^2 and line-out for $t = 50.4$ ps (f/2).
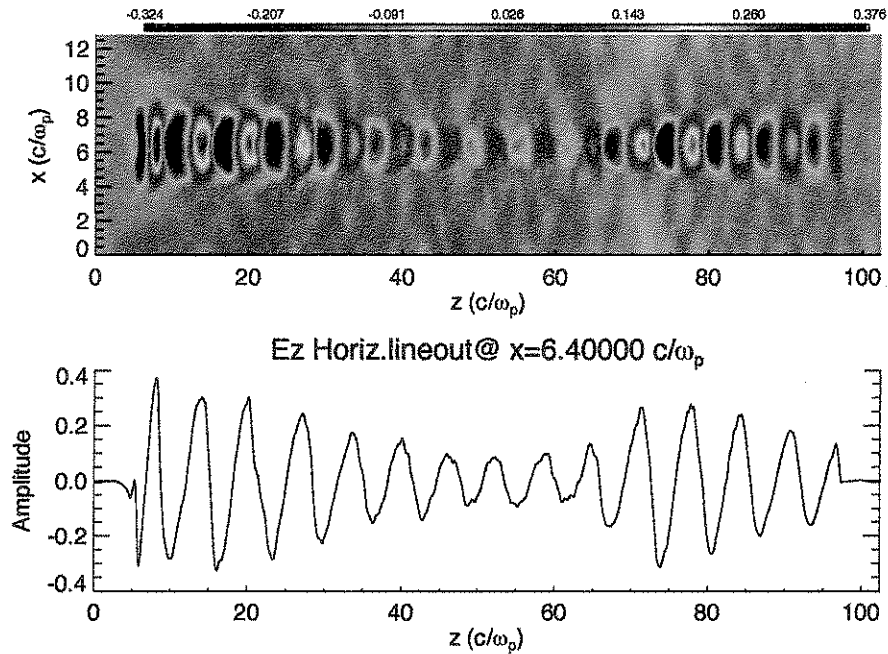

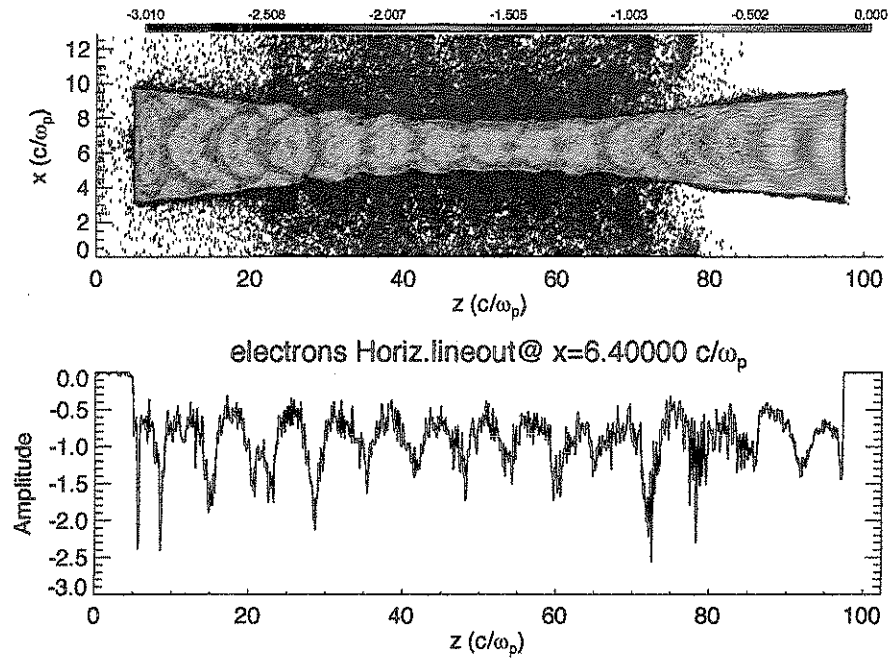Figure 4.3: E_z and line-out for $t = 50.4$ ps (f/2).

68

Figure 4.4: Electron density and line-out for $t = 50.4$ ps (f/2).
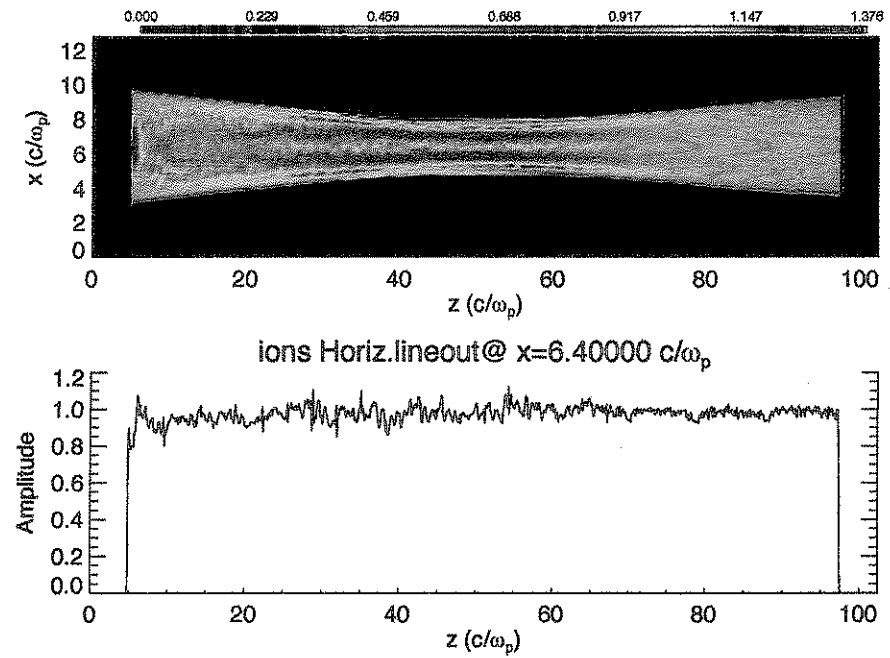
Figure 4.5: Ion density and line-out for $t = 50.4$ ps (f/2).

the axis of propagation after 50.4 ps. The electron plasma density is shown in Figure 4.4 at $t = 50.4$ ps (i.e. half-way into the laser pulse) along with a line-out. These figures illustrate that, although the laser intensity is largest at the focus, there is a weakly driven wake-field at focus and is due to the transverse blow-out of plasma. The spikes in the line-out of Figure 4.4 are due to statistical noise in the simulation and are present in the electron density but not in the overall charge density. The plasma ion density is plotted in Figure 4.5 with a value of 1.0 (it is -1.0 for the electron plasma density) corresponding to a density of 10^{16} cm^{-3}. The gas density chosen in this simulation, as well as the one in the next section, correspond to $n = n_0$. After 50.4 ps the laser has blown-out plasma at the focus to less than 50% of the resonant density, the wave is disrupted, and the amplitude of the wave is reduced near focus. It is clear that the ion plasma density follows the electron plasma density at a slower rate and explains why the ion density is still $\sim$1.0 near the axis in Figure 4.5.

In Figure 4.6, a plot of the maximum on axis wake amplitude as a function of time in the simulation is plotted. Although the peak of the longitudinal field is reached after $\sim$45 ps, this is not reached at the peak of the laser intensity so any electrons interacting with the plasma wave at the focus have a smaller accelerating field exerted on them. This shows that the acceleration process is greatly hindered by the ion motions in this simulation. The decay of the plasma wave also occurs at a faster rate than expected and is attributable to the transverse blow-out of plasma. At the end of the f/2 simulation (t=90.0 ps) the focal region has nearly all of the plasma blown-out, with an excess of ions at the edges of the plasma. The peak wake amplitude achieved in the f/2 focusing is $\sim$0.1 $mc\omega_p/e$ near focus, while it is $\sim$0.35 $mc\omega_p/e$ away from focus (see Figure 4.3). From this amplitude an average accelerating gradient of $\sim$2 GeV/m over a distance of approximately 3 mm can be expected, which implies that a net acceleration of $\sim$6 MeV could be
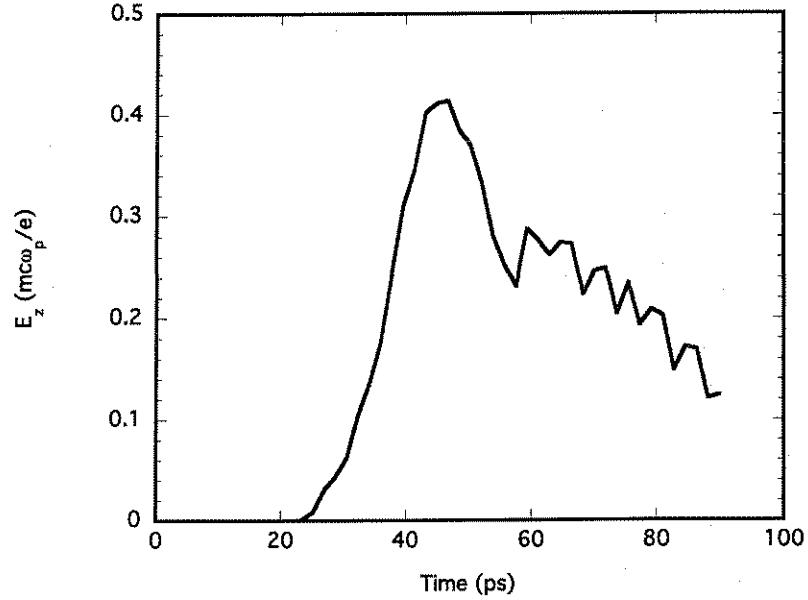
Figure 4.6: Plot of the peak on axis value of $E_z(t)$ versus simulation time (f/2 case).

achieved. This assumes that any transverse field created by the charge separation in the plasma does not perturb the injected electron beam.

4.3 2-D PIC simulation results for the f/18.1 case

Figures 4.7–4.10 illustrate the same four quantities present in the previous section for the f/18.1 case. They show that plasma blow-out is not significant for f/18.1 simulation parameters, where w_0 is ~ 200 μm. The laser spot size is now 4.0 c/ω_p, ion motion does not affect the plasma wave structure and the results are similar when immobile ions are used. The peak wave amplitude achieved is ~ 0.1 $mc\omega_p/e$ which corresponds to an accelerating gradient of 1 GeV/m, and over a 1 cm interaction length ~ 10 MeV acceleration can be expected. Each laser line has an amplitude of $v_{osc}/c = 0.1$ which corresponds to an intensity of $\sim 2 \times 10^{14}$

W/cm^2. The threshold for ionizing hydrogen is 1.47×10^{14} W/cm^2, so the peak wave amplitude may be limited by the laser field amplitude since the time it takes to ionize is long near threshold, and the wave has less time to grow. The position of the best focus appears to move ~ 20 c/ω_p upstream from the vacuum location as the laser beam ionizes the hydrogen (Figure 4.7). This is indicative of the onset of ionization induced refraction which may eventually limit the peak wave amplitude. This effect is very apparent in the experiment (see Figures 3.13 and 3.14) and to model it ideally a larger simulation window must be used as in the f/18.2 simulation.

In Figures 4.9 and 4.10, there is a portion of partially ionized gas at the front of the laser pulse (~ 170 c/ω_p) which is just at the threshold for ionization. The line-out of the electron density also shows the excitation of the plasma wave, while the ion density is constant over the whole length of the plasma. This illustrates that for ~ 100 ps pulses the motion of the ions can be neglected. It will shown that for the longer pulses utilized in the experiment, ion motions play a significant role in allowing for an extended interaction length that is limited in f/18.1 by the refraction of the laser pulse.

In Figure 4.11, the peak on axis wake-field is plotted as a function of simulation time and shows that after ~ 60 ps the amplitude begins to decrease. This gives a window of ~ 40 ps to inject electrons while the wave amplitude is $\sim 80\%$ of its peak value. During that time the electrons would see a relatively large accelerating field for a longer time in comparison to the f/2 case where this time window is only ~ 20 ps (see Figure 4.6). Although the amplitude is larger in the f/2 case the time that the wave lasts is shorter and therefore limits the interaction time and makes synchronization more of an issue. As mentioned above, for this case, an energy gain of ~ 10 MeV could be expected for a 1 cm interaction region.
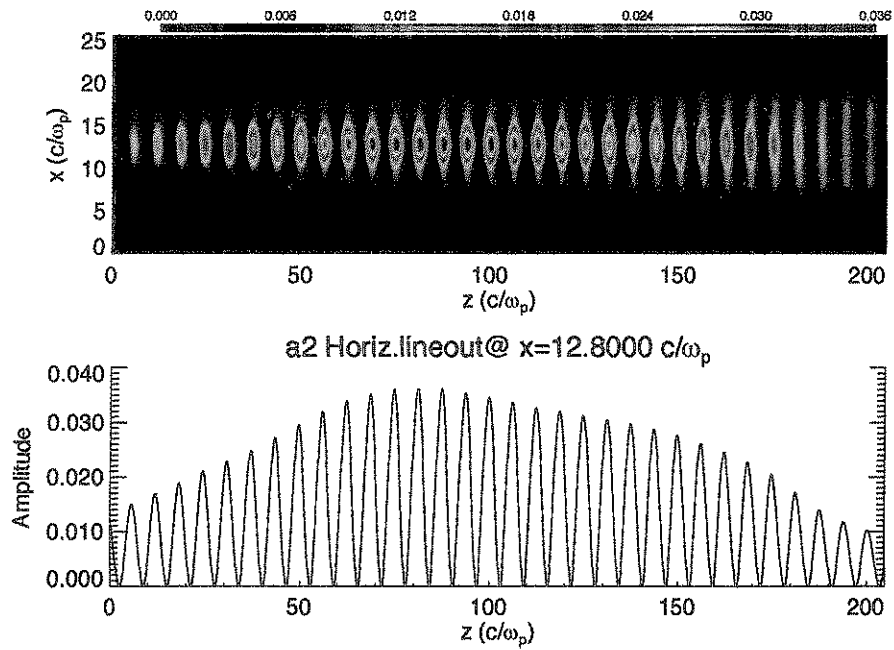
Figure 4.7: α^2 and line-out for $t = 70.2$ ps (f/18.1).
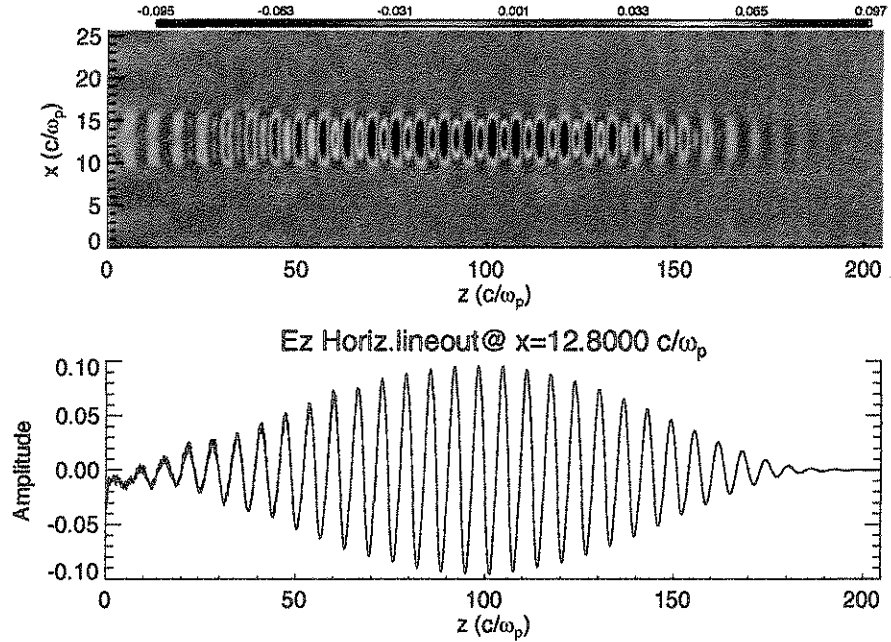
Figure 4.8: E_z and line-out for $t = 70.2$ ps (f/18.1).
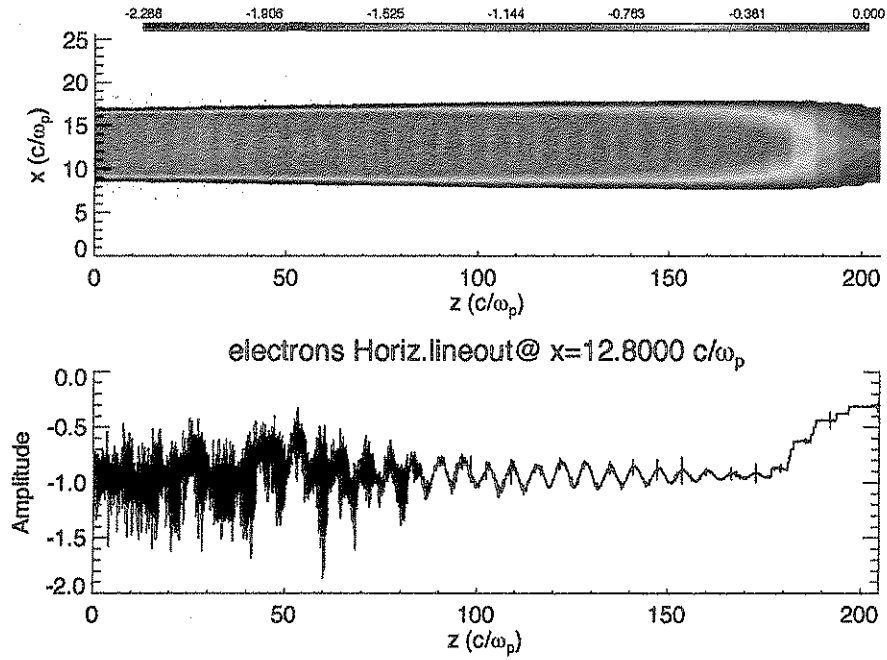
Figure 4.9: Electron density and line-out for $t = 70.2$ ps (f/18.1).

Figure 4.10: Ion density and line-out for $t = 70.2$ ps (f/18.1).
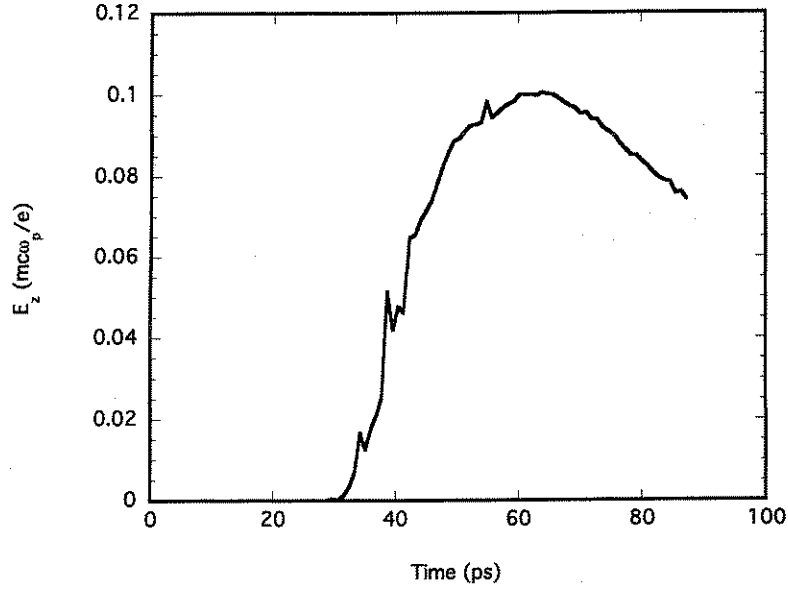
Figure 4.11: Plot of the peak on axis value of $E_z(t)$ versus simulation time (f/18.1 case).

4.4   Comparison of f/2 and f/18.1 cases

The plasma wave structures are quite different for the f/2 and f/18.1 cases and can be attributed to the differences in the transverse fields. In the f/2 case, the plasma wave has a smaller transverse size than the f/18.1 simulation, implying a larger transverse electric field gradient. The f/18.1 simulation has smaller longitudinal fields, and so the transverse fields should also be smaller. In Figures 4.12 and 4.13, the transverse field E_x is presented at 50.4 ps and 70.2 ps for the f/2 and f/18.1 cases, respectively (the line-outs are taken at the center of each simulation window at $z = 50$ c/ω_p and $z = 100$ c/ω_p). These figures show that the amplitude of E_x is 10 times larger for f/2 than for f/18 focusing. For the f/2 case, since E_x is ~ 0.25 $mc\omega_p/e$, the blow-out of electrons can be attributed to the transverse ponderomotive force produced by this field. For the f/2 case the parameter $k_p R$

75
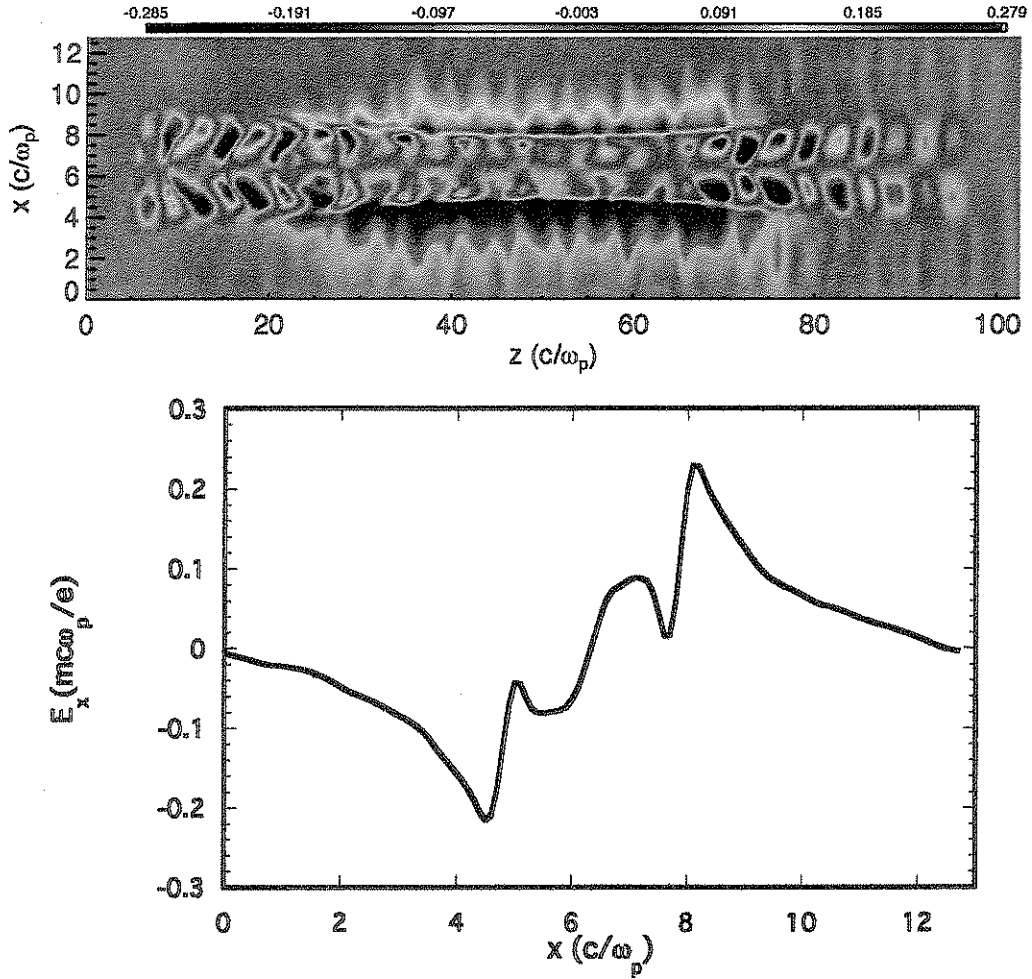
Figure 4.12: E_x for $t = 50.4$ ps and transverse line-out at 50 c/ω_p (f/2).

is $\sim$1 (where R is the transverse dimension) while it is approximately 4 in the f/18.1 case which, according to Fedele *et al.*[32], implies that the ratio of E_x/E_z would be approximately 4 times larger for the f/2 case. This is consistent with the f/18.1 simulation, which gives the electron plasma wave structure for E_z that has been observed in previous 2-D simulations [33]. In the next simulation presented a longer laser pulse is utilized with a $\sim$4 cm long simulation box allowing the observation of ionization induced refraction and the effect it has on the plasma wave.
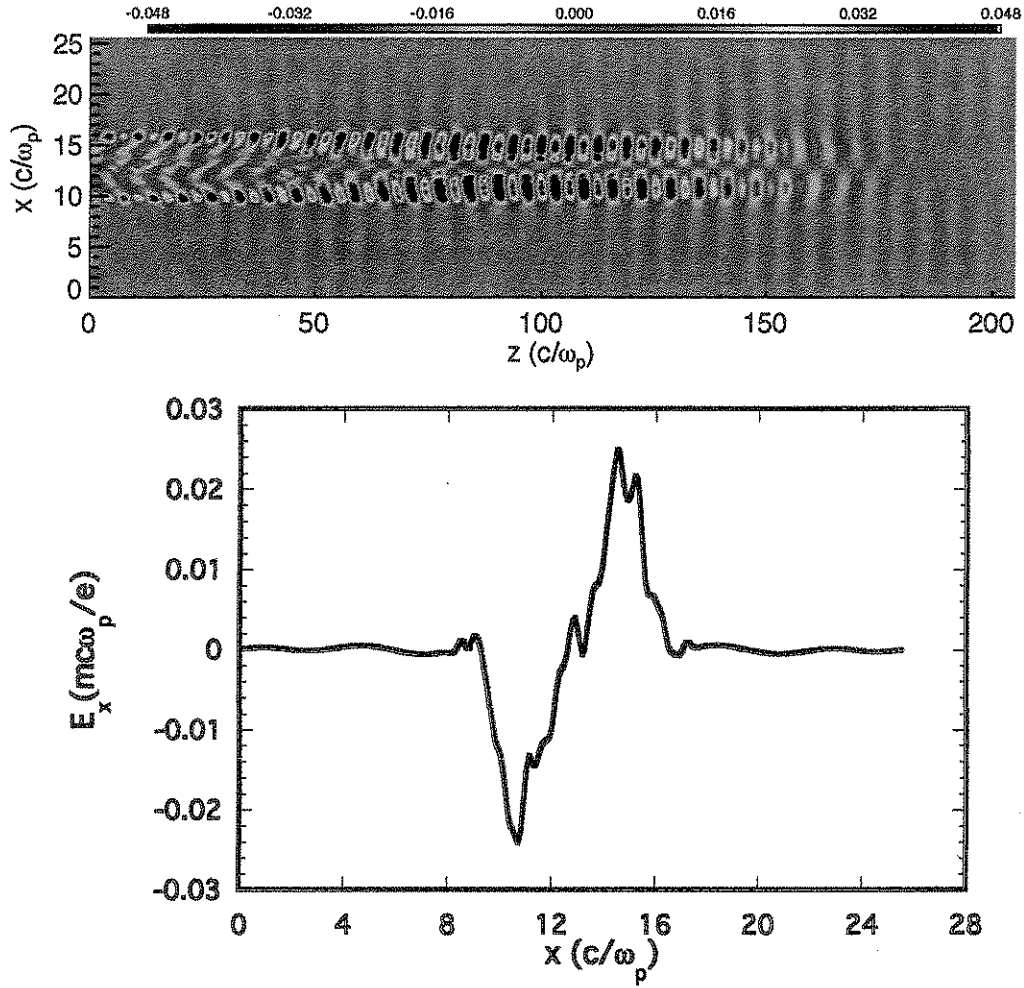
Figure 4.13: E_x for $t = 70.2$ ps and transverse line-out at 100 c/ω_p (f/18.1).

4.5 2-D PIC simulation results for the f/18.2 simulation

The results of the f/18.2 simulation illustrate that the effects of ionization induced refraction play a significant role in the acceleration process. The maximum wave amplitude is reached at the center of the simulation window at $t \approx 50$ ps for the f/2 case and $t \approx 70$ ps for the f/18.1 run, but for the f/18.2 case the peak is approximately 1 cm upstream from the vacuum focus which is at the center of the simulation box. The initial gas density in this simulation is actually set to be 10% larger than the resonant value, which is close to the experimental value used and that led to the highest observed energy gain (see Chapter 3). In Figures 4.14–4.17, the same four quantities shown in the previous set of simulations are presented for a simulation time of 135 ps. At this time that the peak of the laser pulse has entered the simulation window and the laser beam has reached a focus at ~ 200 c/ω_p. The plasma wave is maximum just before this point and reaches a peak value of $\sim 0.3mc\omega_p/e$, but saturates and decays after this point. At this time both the electrons density and ion density plots in Figures 4.16 and 4.17 show no signs of plasma blow-out. As the simulation progresses plasma blow-out, caused by ion motion, eventually leads to the formation of an ion channel that guides the laser beam. This effectively increases the length of the plasma and compensates for the refraction due to ionization. Figures 4.18–4.33 for various simulation times from t=180 ps to 274.5 ps, show the progress of α^2, E_z, the electron plasma density, and the ion plasma density. Although the region of ionization approaches the end of the simulation window, there is still significant refraction of the laser away from the axis of propagation. The same four plots are given in Figures 4.34–4.37 for t=400 ps, and show the formation of the plasma channel nearly to the end of the simulation box, which allows the laser intensity to be large enough to drive a plasma wave at that point.
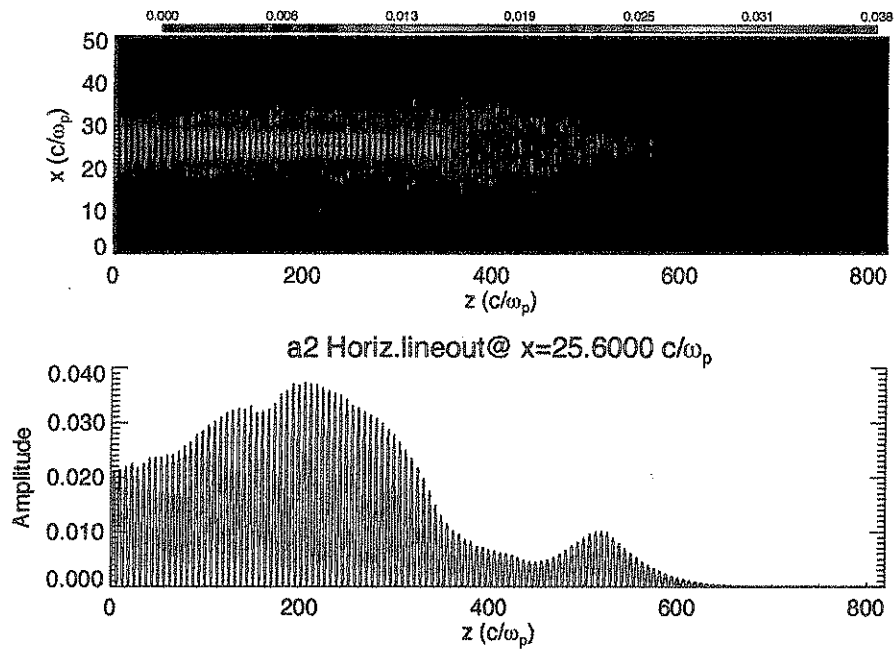
Figure 4.14: α^2 and line-out for $t =135$ ps (f/18.2).


Figure 4.15: E_z and line-out for $t =135$ ps (f/18.2).

Figure 4.16: Electron density and line-out for $t = 135$ ps (f/18.2).

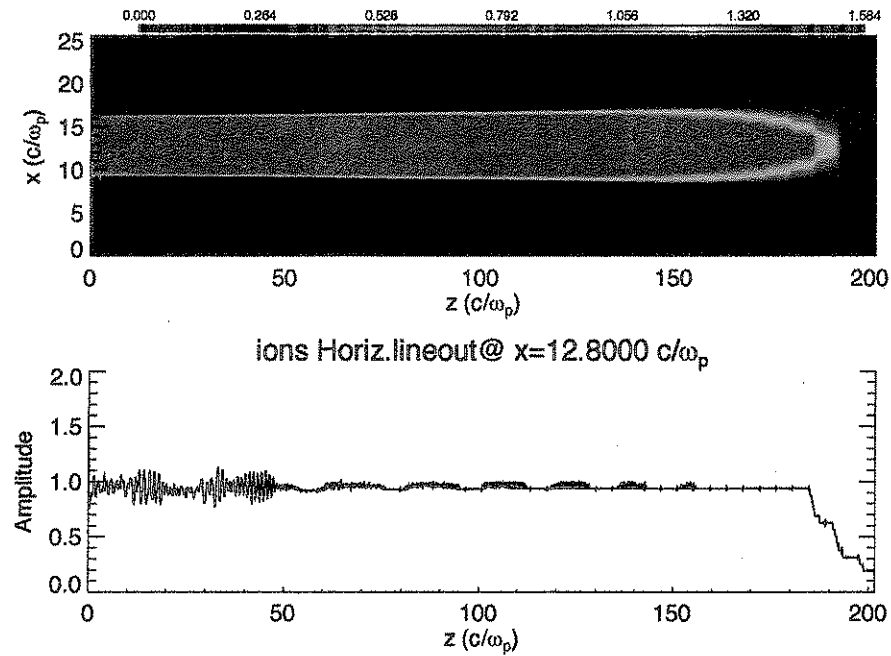Figure 4.17: Ion density and line-out for $t = 135$ ps (f/18.2).

a2 Horiz.lineout@ x=25.6000 c/ω$_p$

Figure 4.18: α^2 and line-out for $t =$180 ps (f/18.2).

Ez Horiz.lineout@ x=25.6000 c/ω$_p$
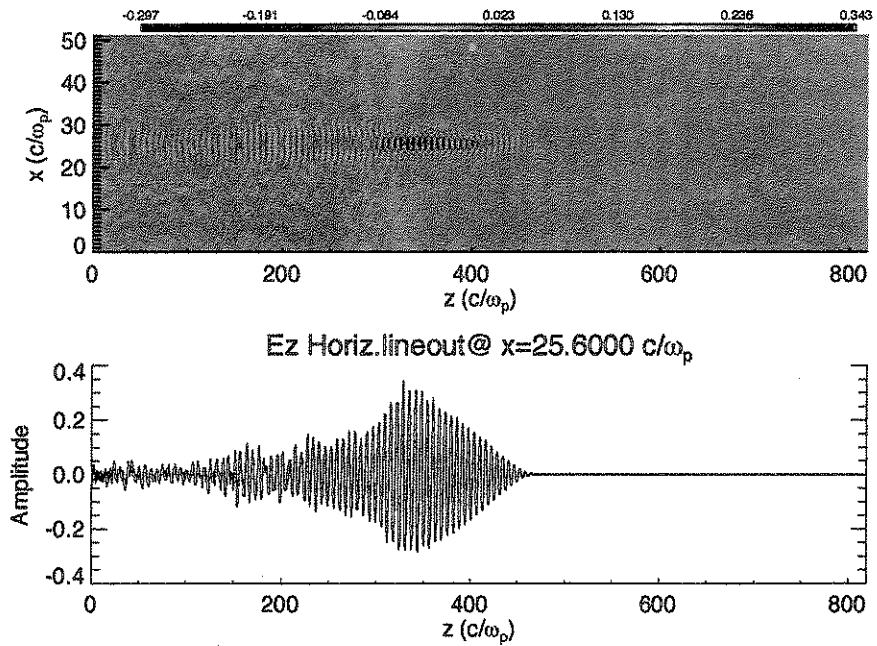
Figure 4.19: E_z and line-out for $t =$180 ps (f/18.2).

Figure 4.20: Electron density and line-out for $t = 180$ ps (f/18.2).

Figure 4.21: Ion density and line-out for $t = 180$ ps (f/18.2).

Figure 4.22: α^2 and line-out for $t = 211.5$ ps (f/18.2).

Figure 4.23: E_z and line-out for $t = 211.5$ ps (f/18.2).

83

Figure 4.24: Electron density and line-out for $t = 211.5$ ps (f/18.2).

Figure 4.25: Ion density and line-out for $t = 211.5$ ps (f/18.2).

84

To get an estimate of the electron acceleration an electron beam is injected on axis into the f/18.2 simulation with $\gamma \approx 23$, neglecting the emittance of the beam. This injected electron bunch has a transverse spot size of $\sigma_x = 1.25$ c/ω_p and a length corresponding to $\sigma_z = 1.25$ c/ω_p (to cover two successive accelerating buckets). The transverse size of the beam is taken to be smaller than the experimental value, to limit any beam loading effects. This electron bunch is injected at $t = 130.5$ ps in the simulation and exits after a time of approximately 144 ps or $\sim$4 cm, corresponding to the length of the simulation window. There are approximately 1500 electrons in the beam representing the 50–100 pC that is present in the actual electron beam.

Figures 4.38–4.42 show the position of this electron bunch as it propagates in the simulation box, along with the line-outs of the longitudinal field E_z at those times. They illustrate that the injection time for this electron bunch is slightly after the peak of E_z in the simulation. The largest plasma wave amplitude is reached at locations where the density is near resonance, and as shown in the previous set of figures, the plasma blow-out causes this region to move later in the simulation box. Since the overall energy gain is a product of the interaction length and the longitudinal electric field, injecting at earlier times would have reduced the interaction region since the relativistic injected electrons would pass the region of peak plasma wave amplitude more quickly. In Figure 4.41, at a simulation time of 238.5 ps, the electron bunch has passed through the plasma wave and propagates through neutral gas. This electron bunch has exited the plasma wave and does not experience any more energy gain, but the phase space distribution of the accelerated electrons is modified significantly after it has exited the plasma (see Figures 4.43 and 4.44).

A second electron bunch ($\gamma \approx 23$ and $\sigma_x = \sigma_z = 1.25$ c/ω_p) was injected at $t = 216$
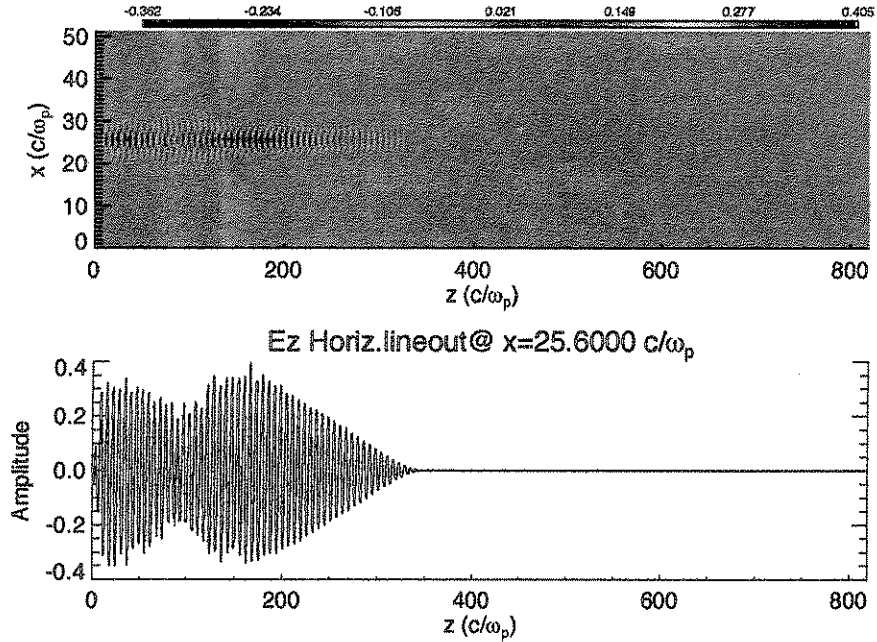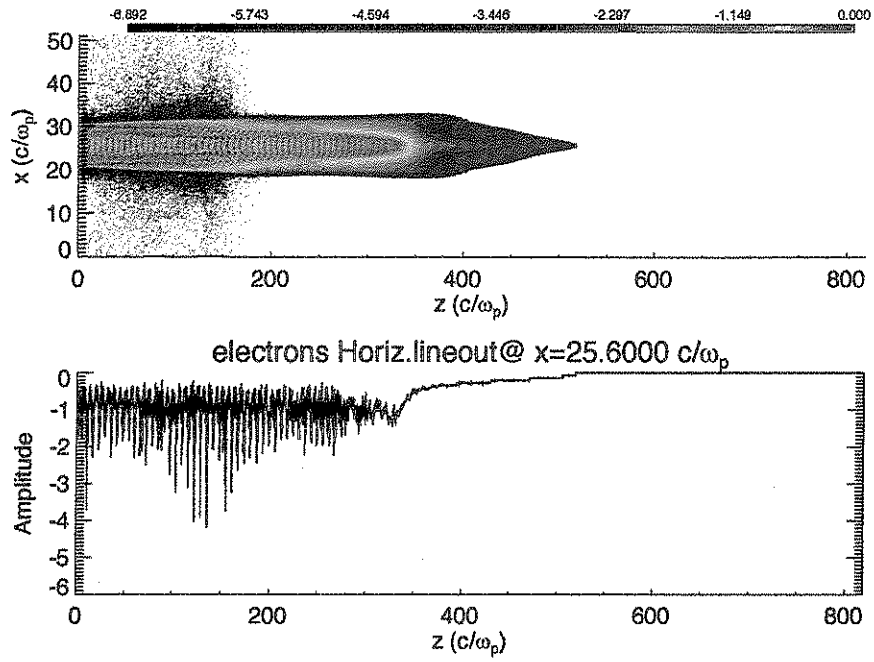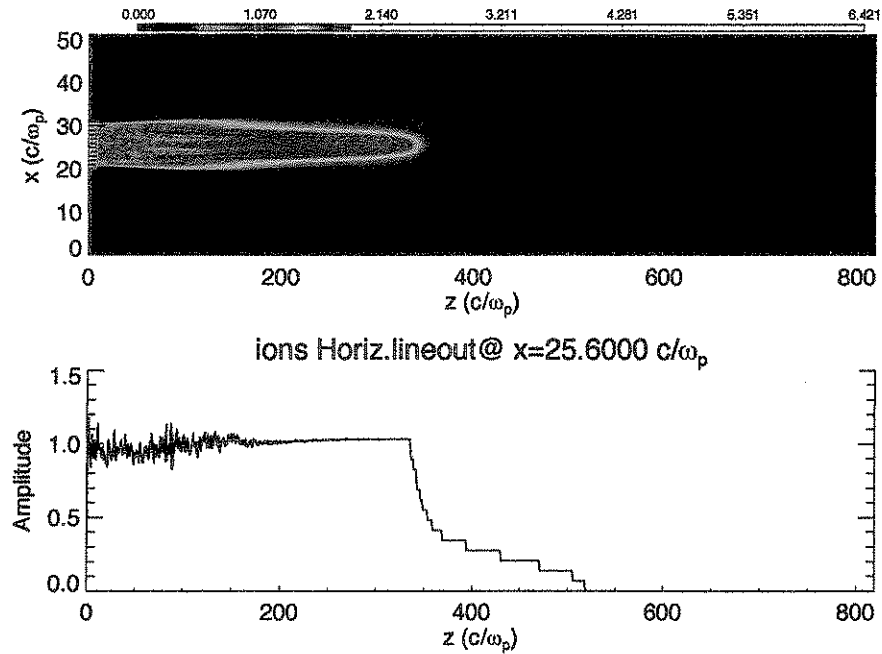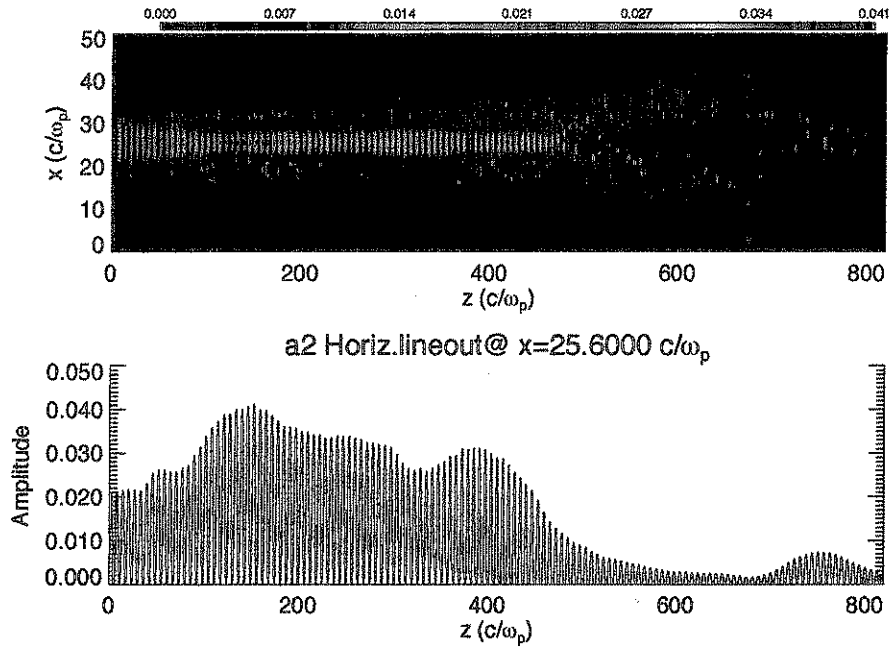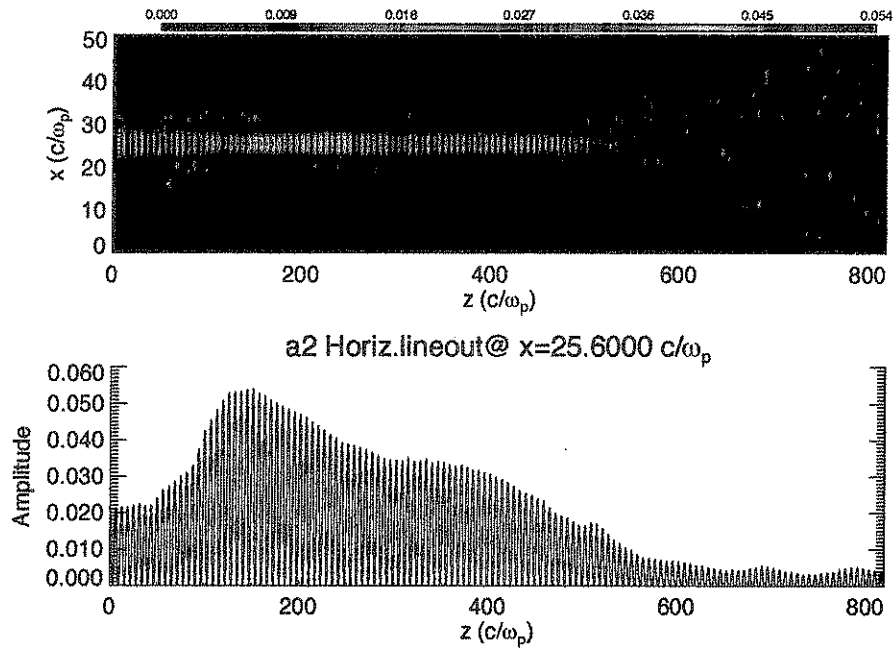
Figure 4.26: α^2 and line-out for $t = 238.5$ ps (f/18.2).
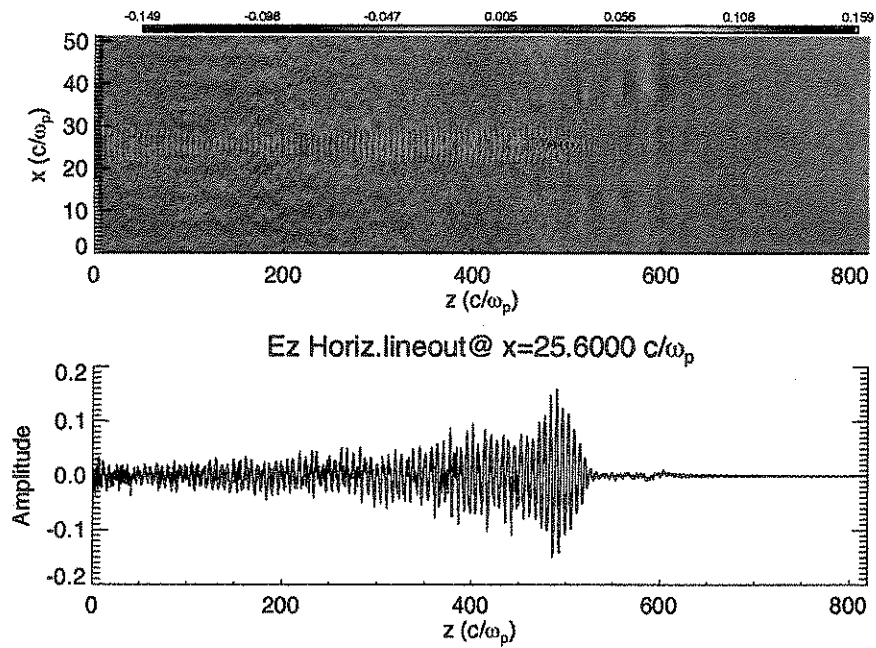
Figure 4.27: E_z and line-out for $t = 238.5$ ps (f/18.2).

electrons Horiz.lineout@ x=25.6000 c/ω_p
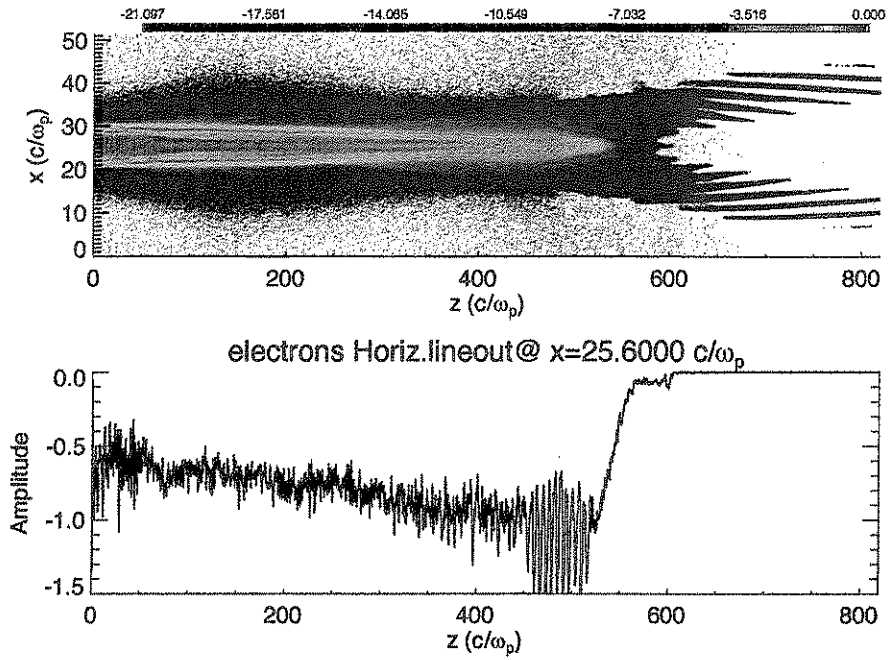
Figure 4.28: Electron density and line-out for t =238.5 ps (f/18.2).

ions Horiz.lineout@ x=25.6000 c/ω_p
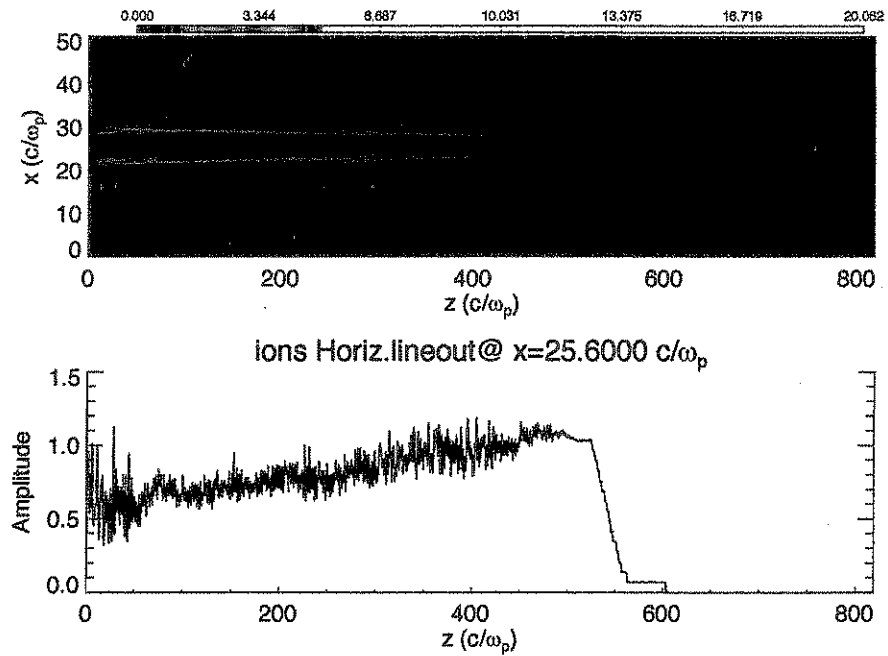
Figure 4.29: Ion density and line-out for t =238.5 ps (f/18.2).

a2 Horiz.lineout@ x=25.6000 c/ω$_p$

Figure 4.30: α^2 and line-out for $t = 274.5$ ps (f/18.2).

Ez Horiz.lineout@ x=25.6000 c/ω$_p$
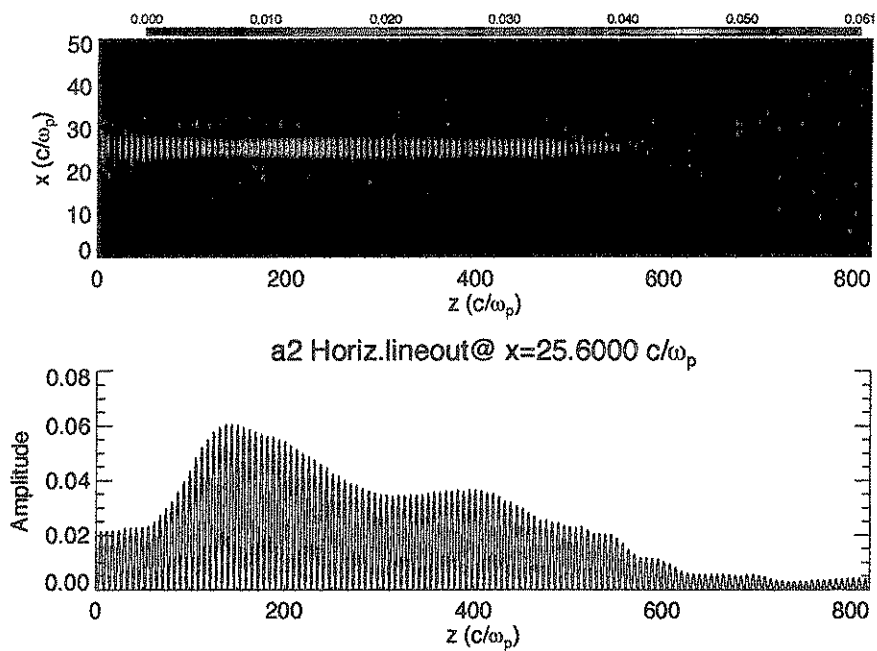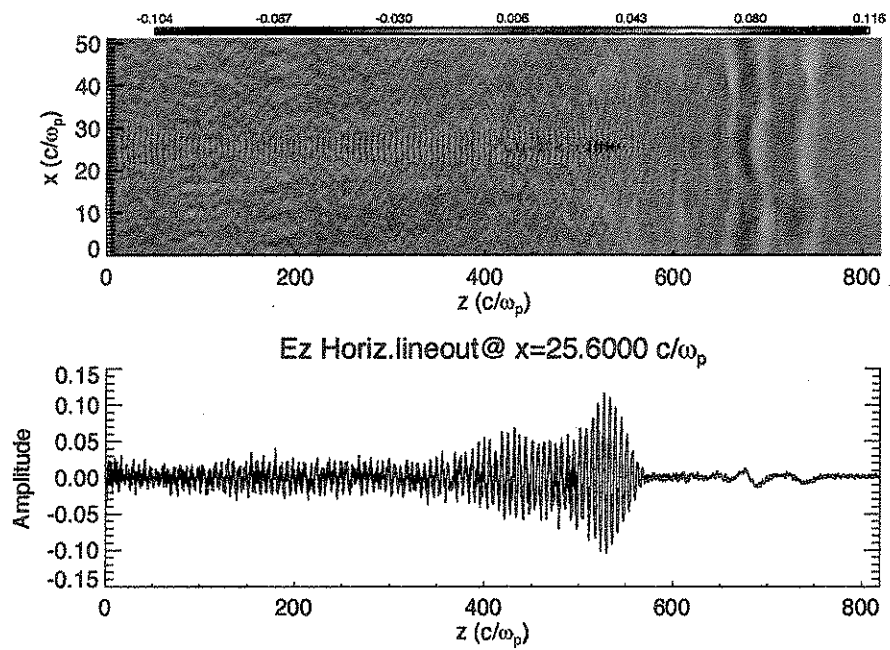
Figure 4.31: E_z and line-out for $t = 274.5$ ps (f/18.2).
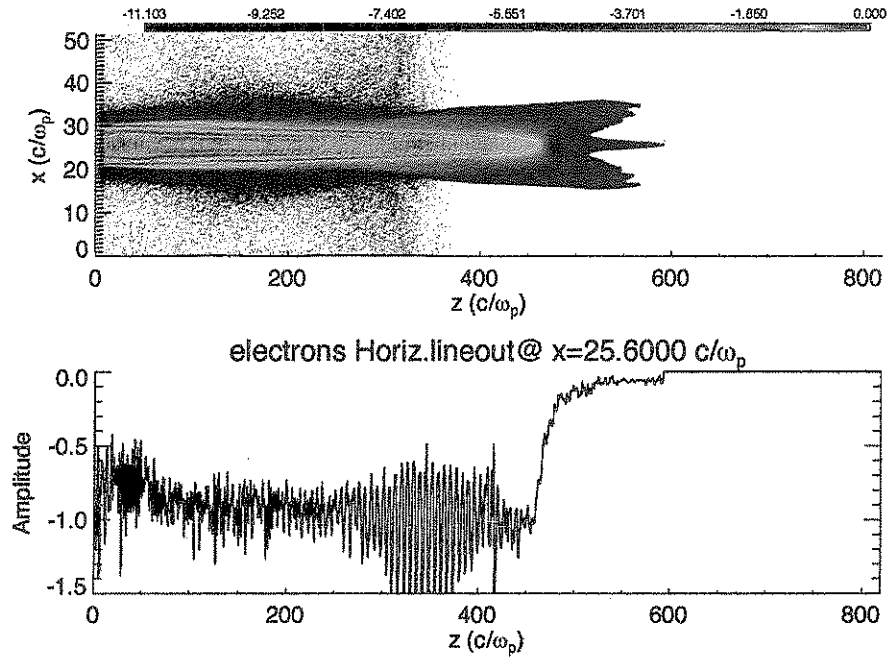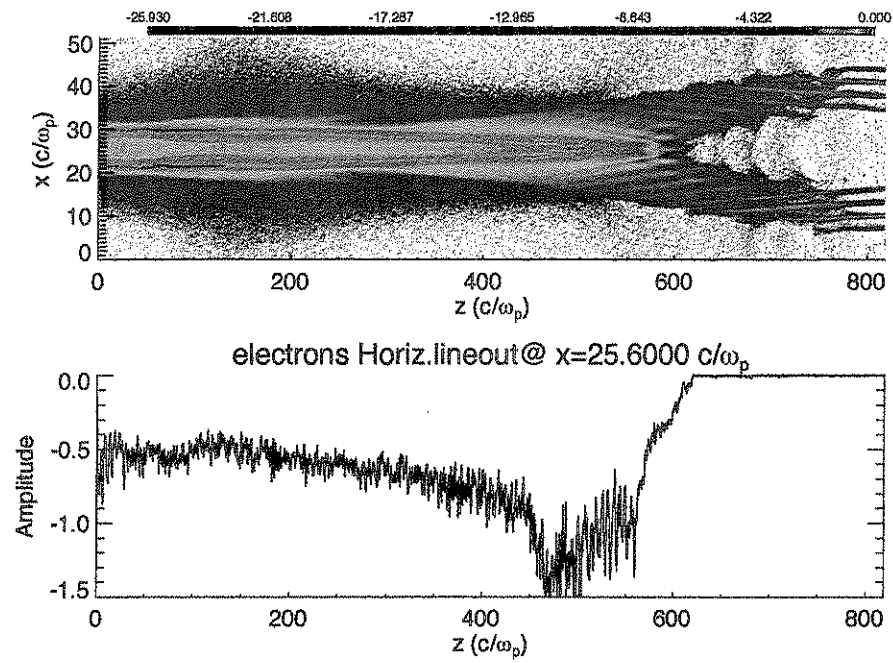
Figure 4.32: Electron density and line-out for $t =274.5$ ps (f/18.2).
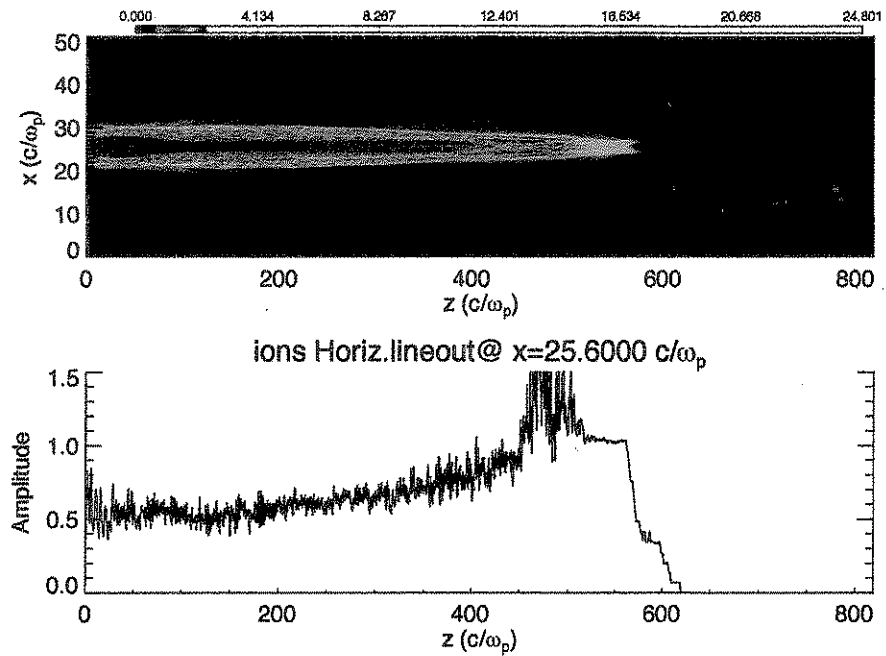
Figure 4.33: Ion density and line-out for $t =274.5$ ps (f/18.2).
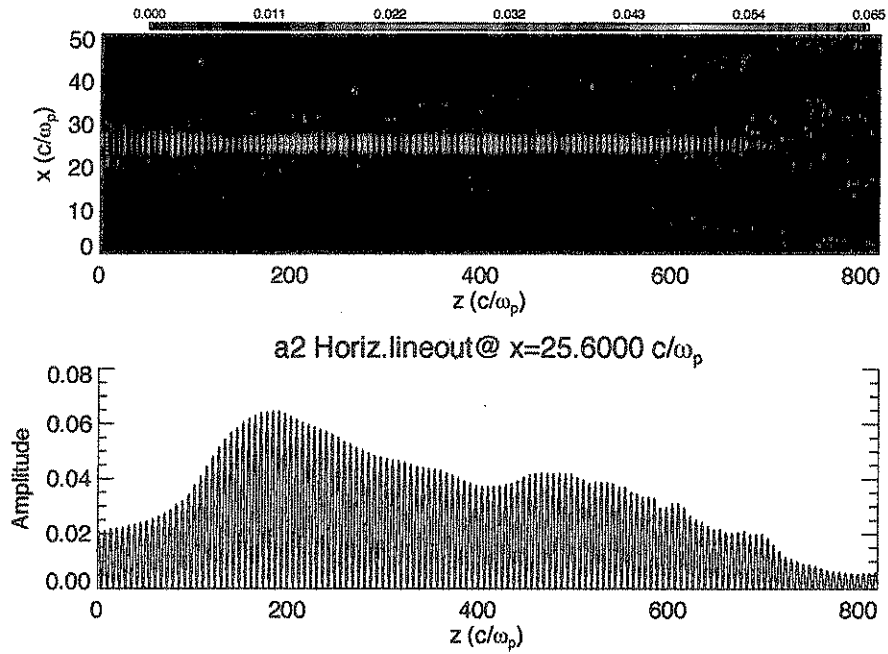
Figure 4.34: α^2 and line-out for $t = 400$ ps (f/18.2).
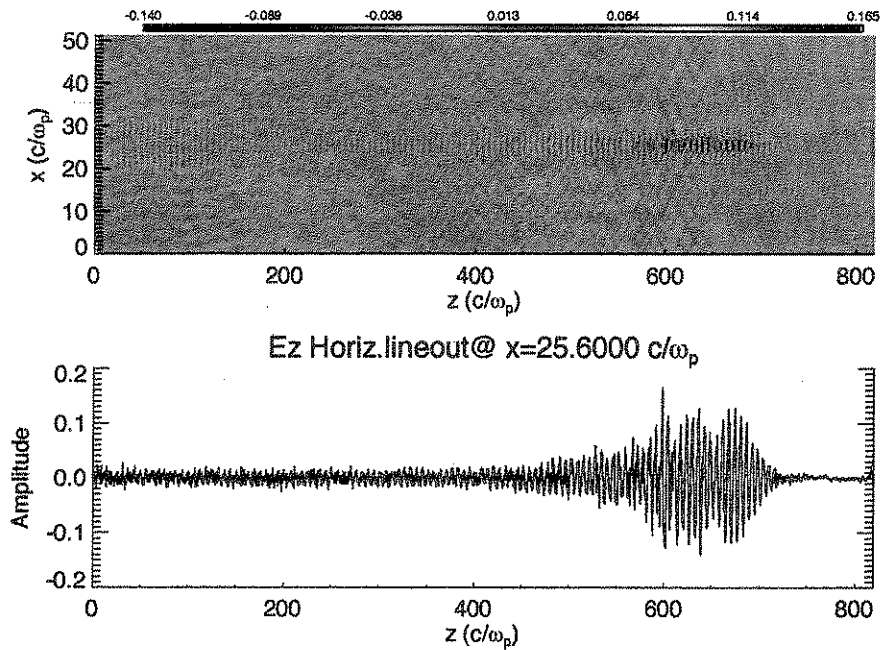
Figure 4.35: E_z and line-out for $t = 400$ ps (f/18.2).

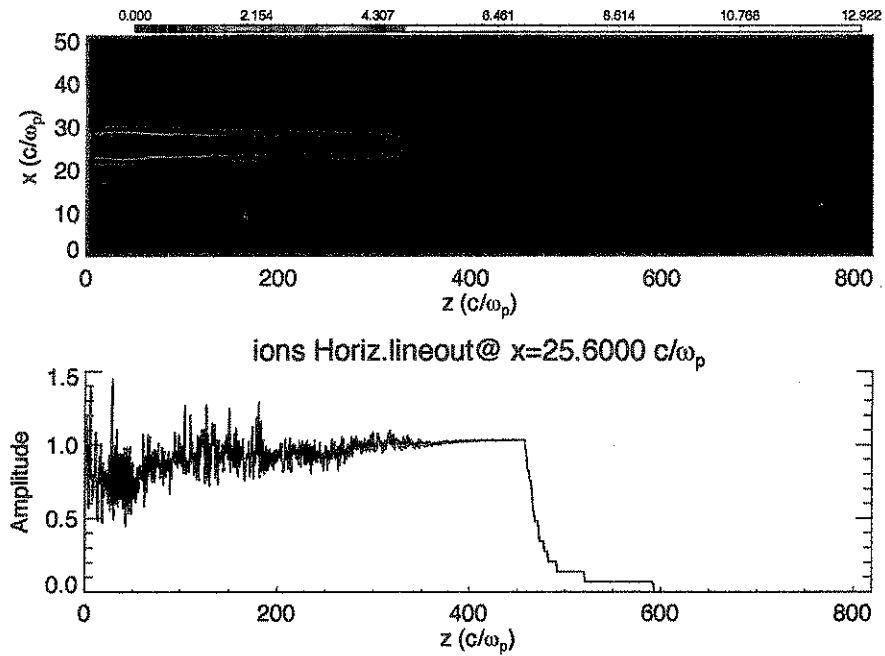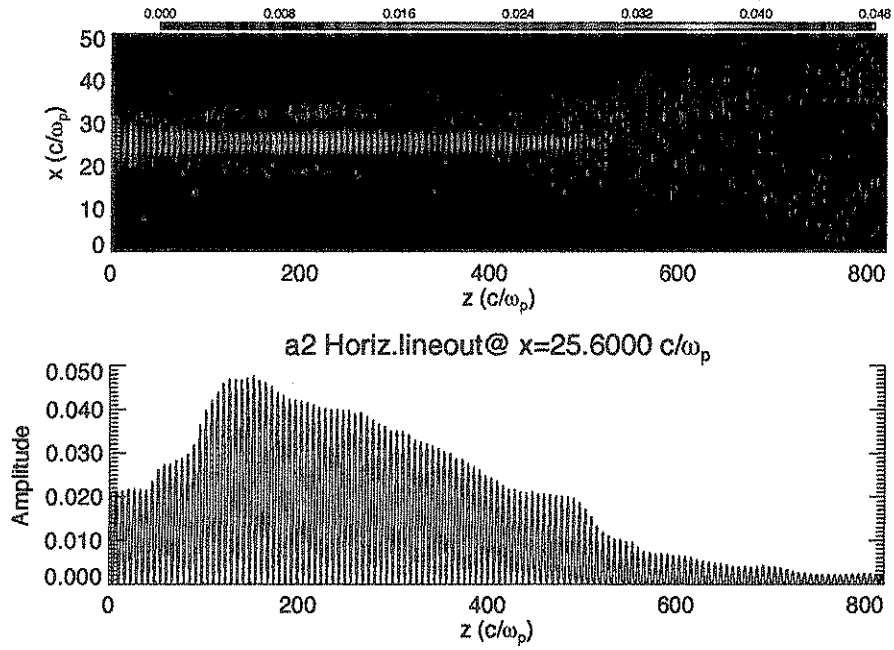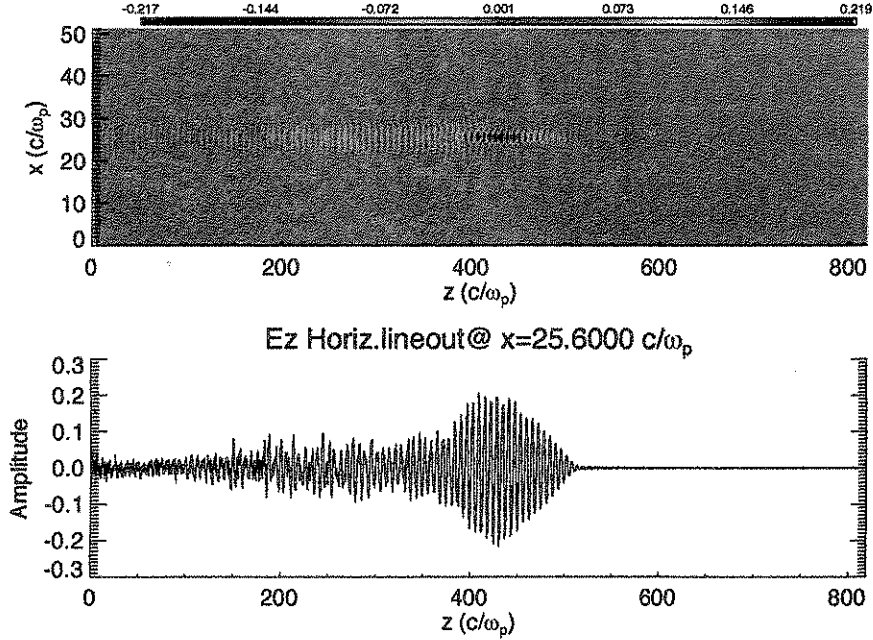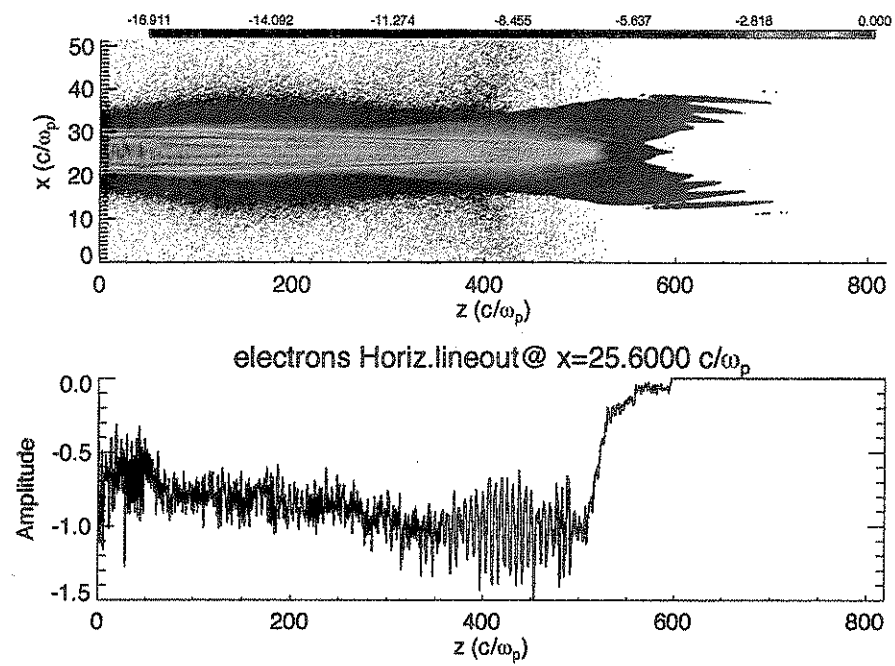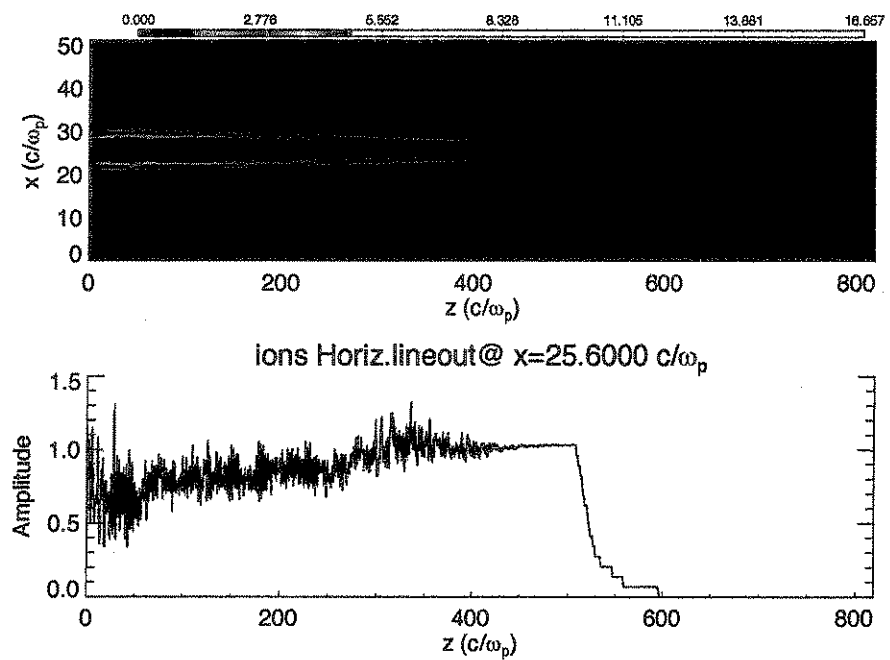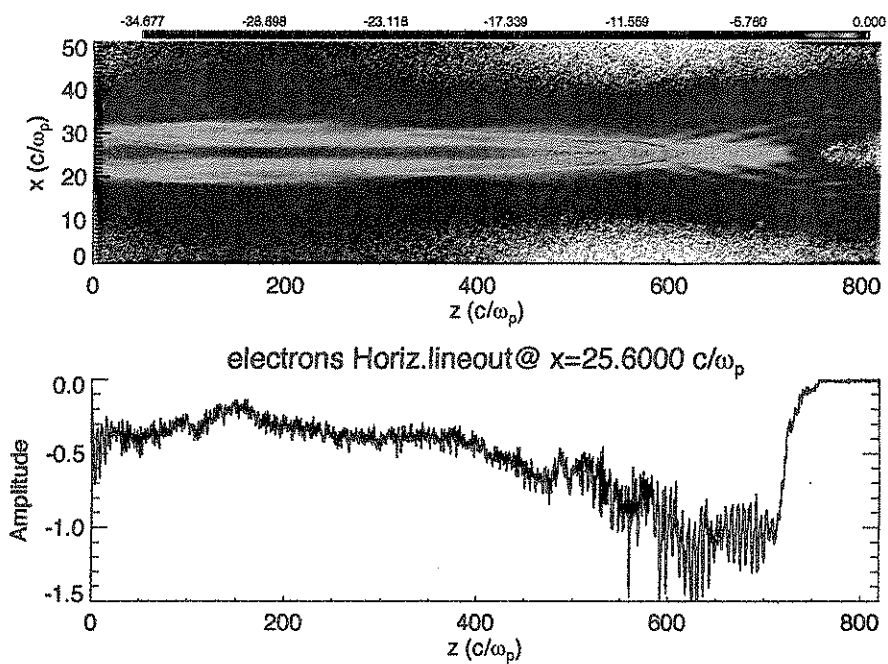Figure 4.36: Electron density and line-out for $t = 400$ ps (f/18.2).
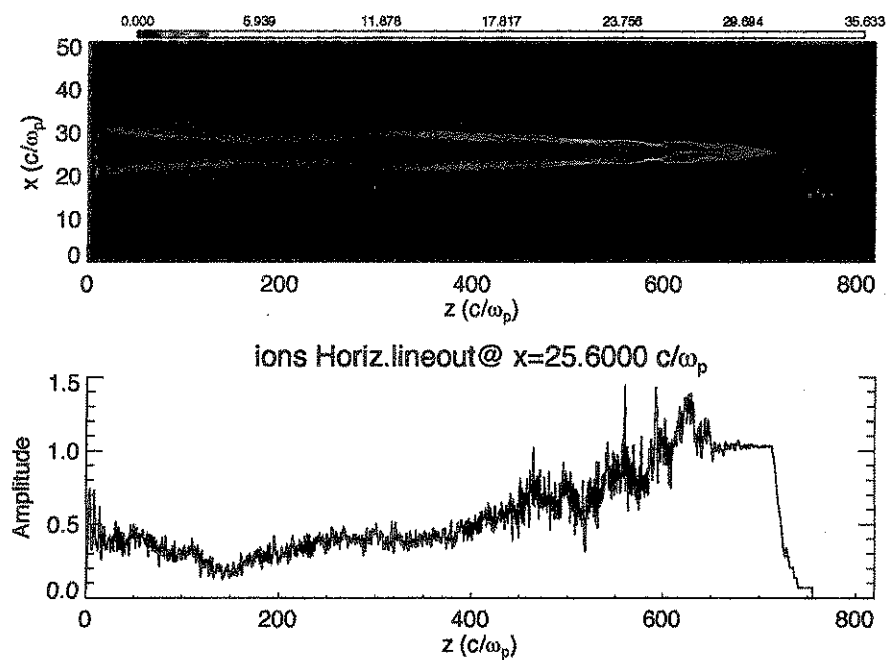
Figure 4.37: Ion density and line-out for $t = 400$ ps (f/18.2).

91
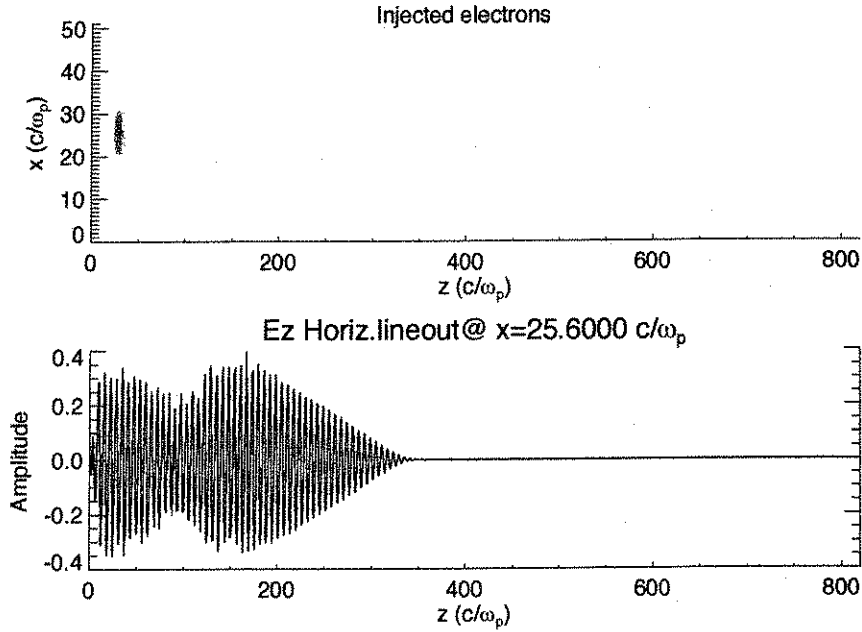
Figure 4.38: Injected electrons and line-out of E_z for t =135 ps (f/18.2).

ps in the simulation to determine what level of acceleration could be possible at later injection times. This electron bunch goes through the plasma when there is a significantly smaller amplitude plasma wave and reached a peak P_z of only ~35 mc at the end of the simulation. The level of electron acceleration appears to be insensitive to changes of ±30 ps, based on the plasma wave amplitude at those times. Increasing the background density may help maintain the resonant density over a longer region, thereby increasing the interaction length and the overall energy gain for both injected electron bunches.

Figures 4.43(a) and 4.44(a) present electron phase space plots of the longitudinal momentum, P_z, of the electrons in the first injected electron bunch versus longitudinal position z for two times in the simulation. The electron energy, E_e, is related to the longitudinal momentum by $E_e = mc^2(P_z - 1)$, where mc^2=0.511 MeV is the electron rest mass energy and P_z is normalized to mc. The electrons
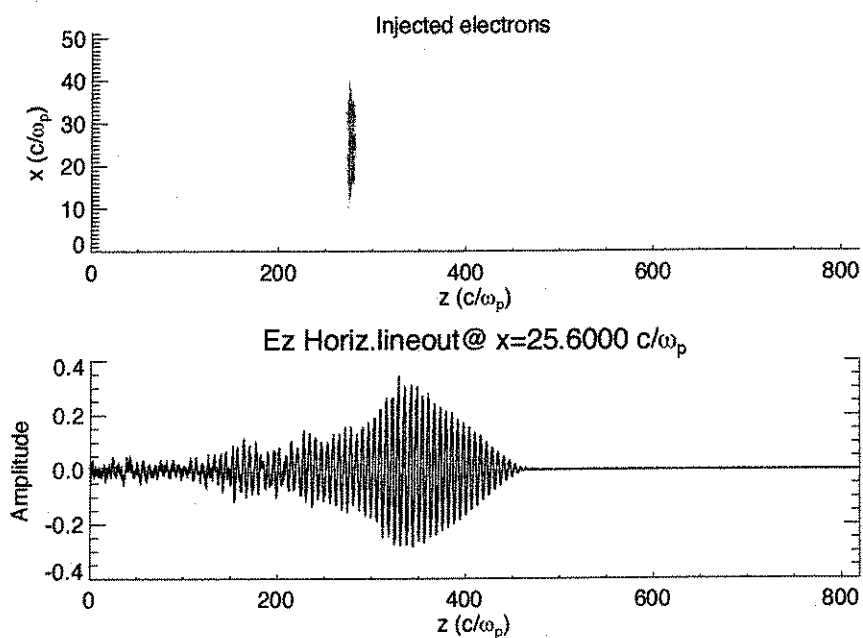
Figure 4.39: Injected electrons and line-out of E_z for $t = 180$ ps (f/18.2).
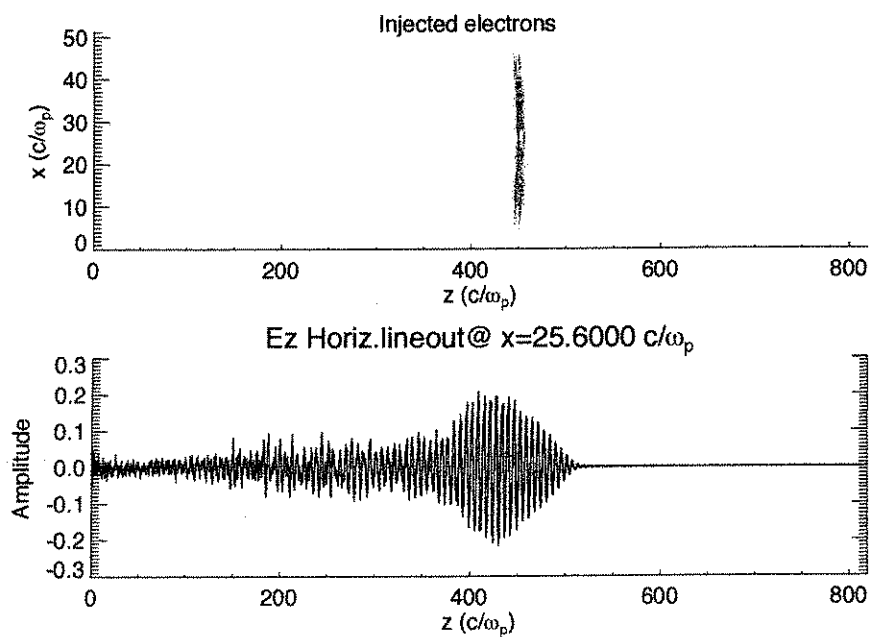
Figure 4.40: Injected electrons and line-out of E_z for $t = 211.5$ ps (f/18.2).
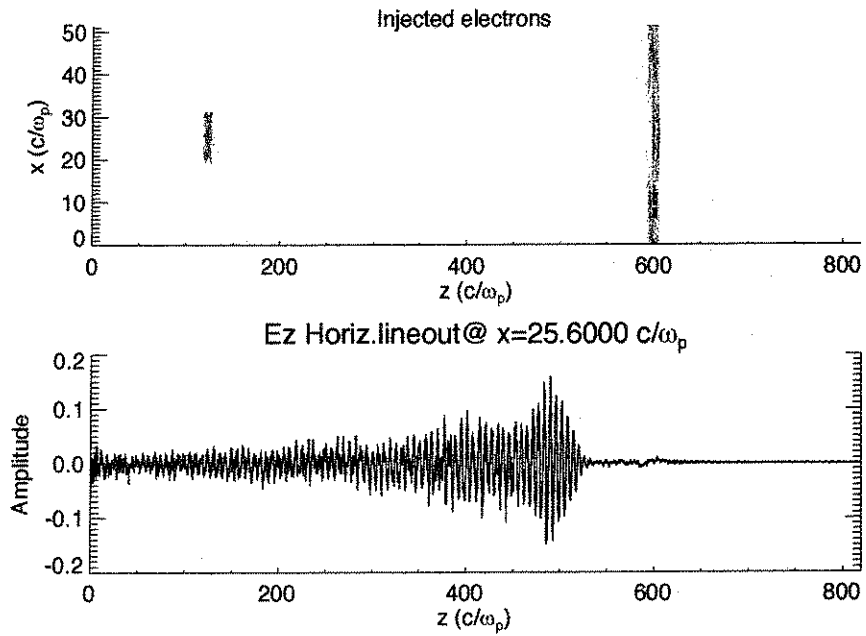
Figure 4.41: Injected electrons and line-out of E_z for $t = 238.5$ ps (f/18.2).
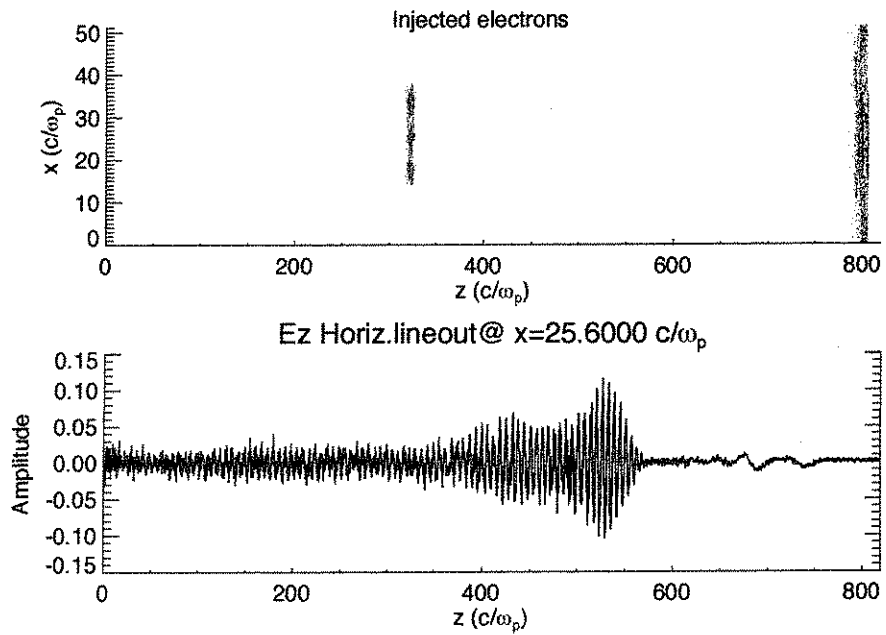
Figure 4.42: Injected electrons and line-out of E_z for $t = 274.5$ ps (f/18.2).

experience little energy gain after they have propagated through the center of the simulation box, since the plasma wave is relatively small or non-existent after that point. Figures 4.43(b) and 4.44(b) give phase space plots of P_z of the electrons versus the transverse position x. They illustrate that the high energy electrons are primarily on axis (x=25 c/ω_p), and as they propagate out of the plasma they are transversely blown. Some of the high energy particles still remain near the axis of propagation, but are much fewer in number.

The electron energy spectrum obtained from the first injected electron bunch at the end of the simulation box, shown in Figure 4.45, shows that the spectrum of electrons in the simulation is similar in appearance to the one obtained from the experiment in Figure 3.17. However, in the experimental plot, the number of high energy particles drops more quickly. This may be the result of not collecting all of the high energy particles in the experiment, and could be improved by adding electron beam focusing elements nearer to the end of the laser ionized plasma. Figure 4.46 is a plot of the peak on axis longitudinal plasma wave amplitude over the entire simulation and the peak value of P_z for the injected electron beam. A slight adjustment of the injection time ($\sim$50 ps earlier) in the simulation may result in some increase in the overall energy gain of the injected simulation electrons, but overall the experimental results compare well to these simulation results.

4.6 Conclusions on Plasma Beat-Wave Acceleration Experiments and Simulations

The experimental results and the modeling of the experiment indicate that for the f/2 case, the transverse fields cause blow-out of the plasma, and is one of
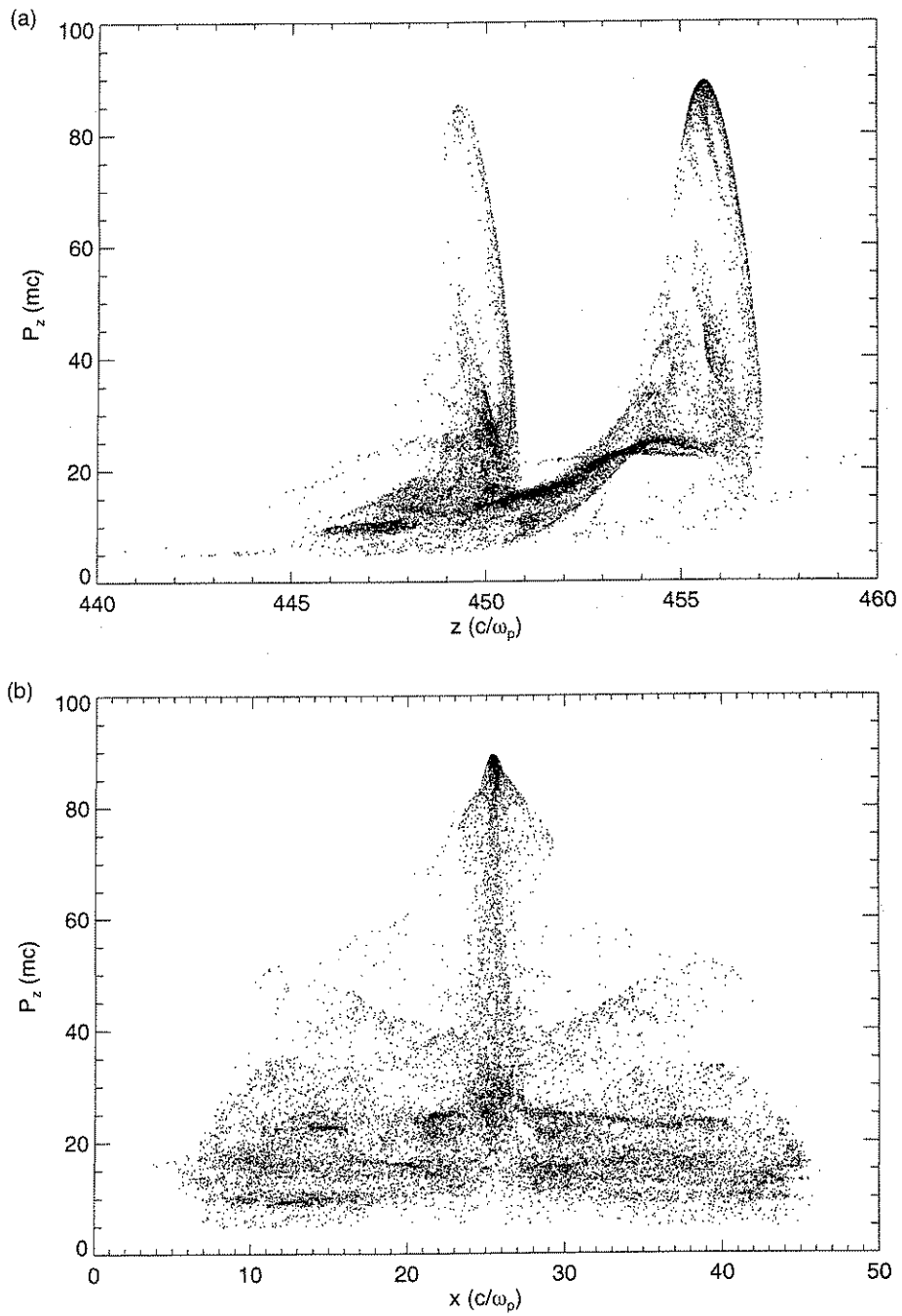
Figure 4.43: Plot (a) is the longitudinal momentum P_z versus z and (b) P_z versus the transverse coordinate x after a simulation time of $t = 211.5$ ps (f/18.2 case).
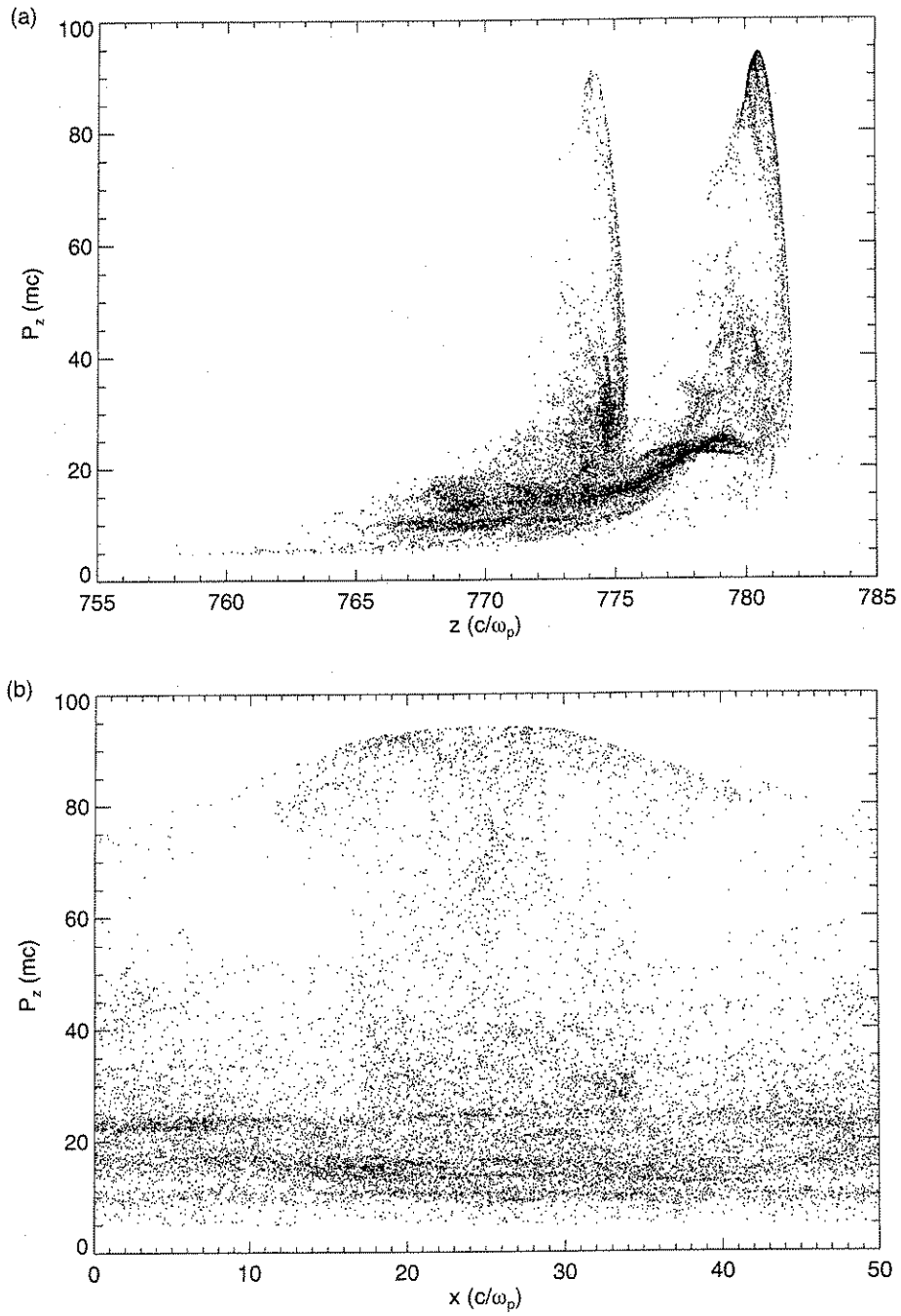
Figure 4.44: Plot (a) is the longitudinal momentum P_z versus z and (b) P_z versus the transverse coordinate x after a simulation time of $t = 274.5$ ps (f/18.2 case).
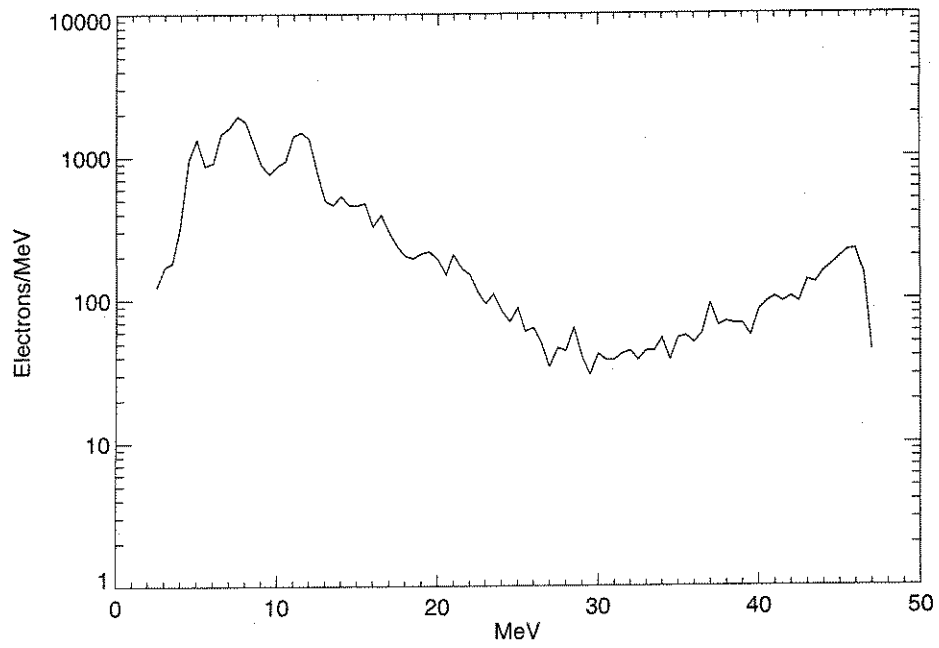
Figure 4.45: Electron energy spectrum in Electrons/MeV for the injected simulation particles as they exit the simulation box, $t = 274.5$ ps (f/18.2).
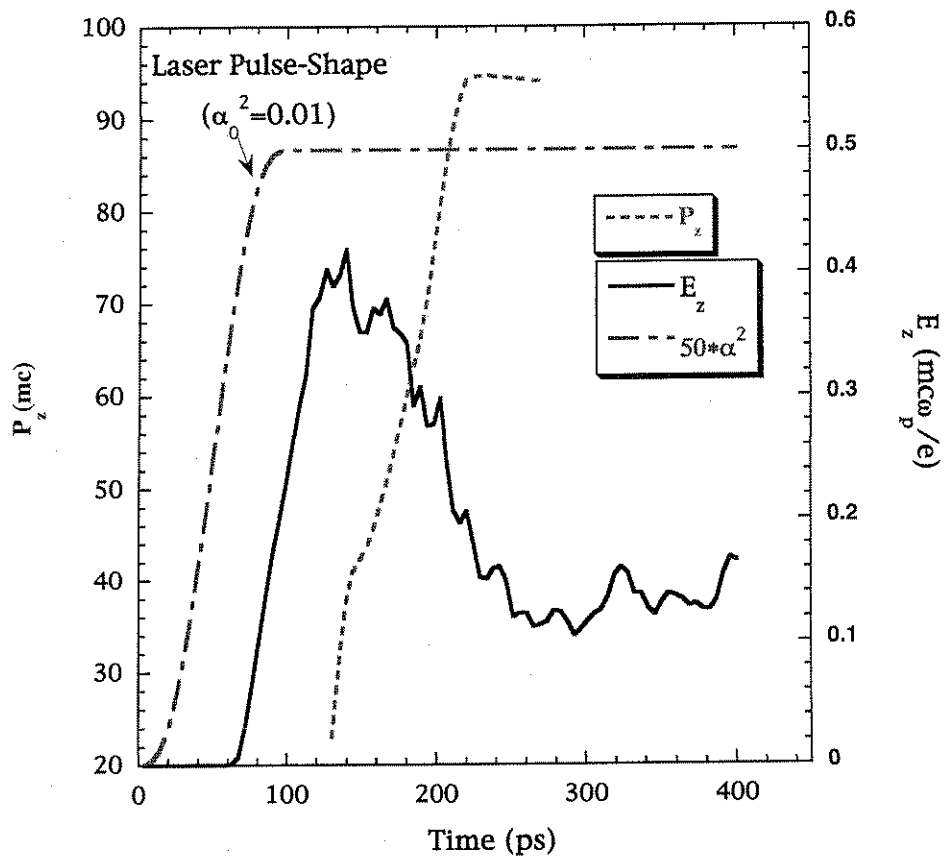
Figure 4.46: The peak on axis value of $E_z(t)$ and the peak P_z of the injected electron beam both plotted versus simulation time (f/18.2 case).

the limiting factors in the acceleration of injected particles. This results not only in a reduction of the plasma wave amplitude at the laser focus, but also in the deflection of beam electrons which is evident in the experiment. For f/18 focusing case, the intensity of the laser and ionization induced refraction of the laser beam may be the limiting factors in producing large amplitude waves for electron acceleration experiments. The relativistic plasma wave amplitudes are consistent with the phase space plots for accelerated electrons produced by injecting an electron bunch in the simulation. For experimental parameters an accelerating gradient of ~ 1.3 GeV/m could be achieved for the f/18 focusing geometry. The f/18 focusing geometry produces a more uniform accelerating structure than the f/2 focusing geometry and shows promise for future experiments.

An alternate approach to increasing the acceleration length would be to employ preformed plasma channels to guide the laser beam. The next chapter will discuss simulations on the acceleration of particles using such preformed plasma channels for experimental parameters achievable with the recent advancements in laser technology.

CHAPTER 5

Simulations on Guiding of Femtosecond Laser Pulses in Preformed Plasma Channels for Acceleration of Self-Trapped Electrons

5.1 Femtosecond Laser Pulse Propagation

There has been considerable recent interest in the guiding of femtosecond laser pulses at high intensities ($\sim5\times10^{18}$ W/cm^2) for applications in laser plasma acceleration [3, 34]. PIC simulations are done in 2-D for laser pulse lengths corresponding to three plasma acceleration schemes in preformed plasma channels. This first case discussed here is the resonant laser wake-field (LWF) excitation of plasma waves, where the laser pulse length is approximately equal to half a plasma period; $\tau \approx \pi\omega_p^{-1}$. The second scheme studied is the resonant beat-wave (BW) excitation of plasma waves in which a two-frequency laser has a frequency separation approximately equal to the plasma frequency and a corresponding beat period equal to the plasma period; $\Delta\omega = \omega_2 - \omega_1 \approx \omega_p$ and $\Delta\tau \approx 2\pi\omega_p^{-1}$. Finally, plasma waves will be excited through the Raman forward scattering instability (also called the self-modulated laser wake-field or SMLWF) with a laser pulse that self-modulates with a characteristic time $\Delta\tau \approx \pi\omega_p^{-1}$, and where the laser pulse length is significantly longer than the resonant wake-field case. All three of these regimes have been studied extensively and were first discussed by Tajima

and Dawson [1]. The optimum conditions for exciting large amplitude relativistic plasma waves to self-trap and accelerate electrons for all three methods will also be discussed. Simulations show that by guiding of intense laser pulses in plasma channels large amplitude wake-fields are excited. These wake-fields can self-trap and accelerate electrons to highly relativistic velocities.

Currently available laser technology has allowed the exploration of new parameter regimes for the excitation of plasma waves. Table-top terawatt, or T^3, lasers are capable of producing intensities on the order of 5×10^{18} W/cm^2 and pulse lengths as short as 50 fs at a wavelength of ~ 0.8 μm. Although such high power lasers allow the excitation of large amplitude plasma waves, the Rayleigh length $Z_R = \pi w_0^2 / \lambda$, is generally on the order of a few hundred microns, for example a spot size w_0 of ~ 7 μm, $Z_R = 200$ μm. This limits the effective acceleration length and therefore the energy gain, so a variety of techniques have been proposed to propagate laser pulses over distances greater than Z_R [35]. One promising method of producing large amplitude plasma waves over distances larger than the characteristic Rayleigh length is by guiding multi-terawatt femtosecond laser pulses in preformed plasma channels. In a plasma channel guiding takes place if there is a radial index of refraction gradient $\partial \eta / \partial r$ that can balance the divergence of the laser beam.

The results presented will utilize the simulation codes TurboWAVE [4] and OSIRIS [36] explicitly resolving the the frequency of the laser pulses. Both codes are capable of modeling high power laser pulse propagation in preformed plasma channels and are used in a Cartesian geometry in two dimensions (slab geometry) with a moving simulation window. TurboWAVE was used in the previous chapter for the simulation for beat-wave excitation of plasma waves which propagated a shorter distance, and where the laser pulse did not experience significant phase

Run	$dx(c/\omega_{pn})$	$dz(c/\omega_{pn})$	$dt(\omega_{pn}^{-1})$	x×z-cells	Steps	a_0
LWF.1	0.1	0.007	0.0067	256×3648	300,000	3.0
LWF.2	0.1	0.007	0.0067	256×3648	300,000	2.0
BW.1	0.2	0.006	0.003	128×8192	105,000	1.0, 1.0
BW.2	0.2	0.006	0.003	128×8192	15,000	0.75, 0.75
BW.3	0.2	0.006	0.003	128×8192	30,000	0.5, 0.5
SMLWF.1	0.1	0.007	0.0067	256×3712	288,000	2.0

Table 5.1: Simulations for Guiding Intense Laser Pulses in Plasma Channels

modulation and spatial break-up, unlike the LWF and SMLWF cases. For this reason OSIRIS is utilized for the LWF and the SMLWF simulations. A summary of the simulations performed is given in Table 5.1 with a density of $n = 10^{18}$ cm^{-3} used as a normalization in all cases, corresponding to a $c/\omega_{pn} \approx 5.3$ μm, where $\omega_{pn} = (4\pi n e^2/m)^{1/2}$. The rest of this chapter will concentrate on runs LWF.1, BW.1, and SMLWF.1 which produced the most promising results. Simulation LWF.2 trapped particles but did not accelerate them to as high energies as LWF.1. Of the three beat-wave simulations, BW.1 produced the best results and therefore those results are presented in this chapter.

5.2 Basic Equations and Guiding in a Plasma Channel

The guiding of intense laser pulses is closely related to the self-focusing effect [37] in nonlinear optics. The starting point in describing the propagation of intense laser pulses is the nonlinear wave equation,

$$\nabla^2 \mathbf{E} - \frac{\partial^2}{c^2 \partial t^2} \left[(\eta_0 + \Delta\eta)^2 \mathbf{E} \right] = 0, \tag{5.1}$$

where $\Delta\eta$ is the nonlinear index of refraction corresponding to both the field induced index change and the parabolic index of refraction gradient used in the simulations presented here. The index of refraction can be written as $\eta = \eta_0 + \Delta\eta = \eta_0 + \eta_2|E|^2 - \Delta\eta_p w^2/w_0^2$, where η_0 is the vacuum index and $\Delta\eta_p$ and w_0 are constants. Using the wave equation along with the paraxial ray approximation, the slowly varying amplitude approximation [37], and by transforming to the reduced time variable $\xi = t - z/v_g$ the paraxial wave equation is obtained:

$$\left(i2k\frac{\partial}{\partial z} + \nabla_\perp^2\right)\tilde{E} = -2k^2\left(\frac{\Delta\eta}{\eta_0}\right)\tilde{E}, \tag{5.2}$$

where k is equal to ω_L/c and ω_L is the laser frequency. Separating $\tilde{E}$ into amplitude and phase terms with $\tilde{E} = \tilde{E}_0 e^{i\phi}$, two conditions describing the balance between self-focusing and diffraction in the guiding medium are obtained:

$$k\frac{\partial}{\partial z}\tilde{E}^2 = -\nabla_\perp \cdot (\tilde{E}_0^2 \nabla_\perp \phi) \tag{5.3}$$

$$\frac{\partial\phi}{\partial z} + \frac{1}{2k}(\nabla_\perp\phi)^2 - \frac{k}{2}\left(2\frac{\Delta\eta}{\eta_0} + \frac{\nabla_\perp^2\tilde{E}_0}{k^2\tilde{E}_0}\right) = 0. \tag{5.4}$$

Equation 5.4 can be thought of as a Hamiltonian expression, $H = p^2/2m + V$, from which an effective potential [37],

$$V = -\frac{k}{2}\left(2\frac{\Delta\eta}{\eta_0} + \frac{\nabla_\perp^2\tilde{E}_0}{k^2\tilde{E}_0}\right), \tag{5.5}$$

can be taken. From this expression a relationship for the amplitude of the ray vector r as a function of z is obtained

$$\frac{d^2r}{dz^2} = -\frac{1}{k}\frac{\partial V}{\partial r} = \frac{1}{2}\frac{\partial}{\partial r}\left(2\frac{\Delta\eta}{\eta_0} + \frac{\nabla_\perp^2\tilde{E}_0}{k^2\tilde{E}_0}\right). \tag{5.6}$$

An effective potential which describes the balance between diffraction and self-focusing can then be derived for a Gaussian profile with a radius w:

$$V \simeq -k\left(\frac{\Delta\eta}{\eta_0} - \frac{1}{k^2w^2}\right). \tag{5.7}$$

This analysis gives a value for the input spot size corresponding to a particular index of refraction gradient in a medium resulting in propagation with minimal change in the laser beam profile. Inserting the value of $\Delta\eta$ into Equation 5.7 gives the following:

$$V \simeq \frac{1}{Z_R w^2/w_0^2}\left(1 + \frac{P_L}{P_c} - \frac{\Delta\eta_p}{\Delta\eta_c}w^4\right),\qquad(5.8)$$

where the laser power is $P_L = \pi w_0^2|\tilde{E}_0|^2/2$, the critical power $P_c = \lambda^2/4\pi\eta_0\eta_2$, and $\Delta\eta_c = \lambda^2/2\pi^2\eta_0 w_0^2$ is the critical channel depth for a parabolic profile. These are important parameters in the guiding of intense laser pulses. The critical power for relativistic self-focusing in a plasma can be written as $P_c \simeq 17.4(\lambda_p/\lambda)^2$ GW. Using the expression for the critical channel depth one can estimate the plasma density variation necessary to guide a laser pulse in a plasma.

An expression for the density in a parabolic plasma channel can be written as

$$n = n_0\left[1 + \frac{\Delta n}{n_0}\left(\frac{w}{R_{ch}}\right)^2\right],\qquad(5.9)$$

where w is the radius in the beam, R_{ch} is the radius of the channel, n_0 is the plasma density at the center of the channel, and $\Delta n/n_0$ is the density variation between the center and wall of the channel. The critical value of the density variation, which is the minimum variation to guide the laser pulse, can be calculated to be

$$\frac{\Delta n_c}{n_0} = \left(\frac{\lambda_p}{\pi w_0}\right)^2,\qquad(5.10)$$

where λ_p is the plasma wavelength and w_0 is the spot size of the laser [35]. The value of the density variation must be $\sim\Delta n_c/n_0$ for the laser to be guided.

To optimize the density for a given laser pulse length and wavelength such that the largest amplitude wake would be produced, a series of 2-D simulations varying n_0 from 0.5×10^{18} cm^{-3} to 8×10^{18} cm^{-3} were performed. A Gaussian
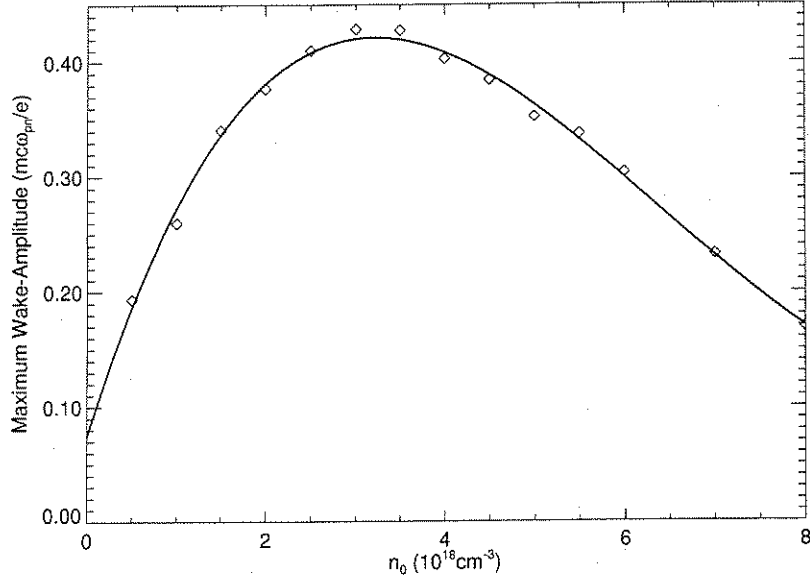
Figure 5.1: Plot of the peak wake-amplitude on axis versus density, n_0, for a 50 fs laser pulse.

transverse profile of the laser intensity is used for all simulations presented in this chapter. The laser pulse utilized has a 0.8 μm wavelength with a 50 fs pulse-length (FWHM) and is propagated approximately two Rayleigh lengths in a preformed plasma channel. The temporal shape of the laser pulse is defined by $f(x) = 10x^3 - 15x^4 + 6x^5$, where $x = t/\tau$ and τ is the rise and fall; this is to approximate a gaussian laser pulse [4, 36]. Figure 5.1 shows the density producing the largest amplitude wake is $n_0 \approx 3 \times 10^{18}$ cm^{-3} for $a_0 = 0.8 mc\omega_L/e$, where a_0 is the normalized laser vector potential (the curvefit is a polynomial fit of the data). A value of 0.8 $mc\omega_L/e$ is used to stay below the wave-breaking amplitude so a smooth resonance curve could be produced. The value of half a plasma period required, $\pi\omega_p^{-1}$, to resonantly drive a wake-field is ~32 fs for $n_0 = 3 \times 10^{18}$ cm^{-3}.

The size of the laser beam used in the simulations is matched to the size of

the channel, where the laser spot size, w_0, is ~ 7 μm and R_{ch} is ~ 10 μm. The matched beam size is given by

$$w_m = \left(\frac{R_{ch}}{k_p}\right)^{1/2},$$

(5.11)

where k_p is ω_p/c [35]. The optimum density variation for resonant laser wake-field driving in these simulations was found to be $\sim 2\Delta n_c/n_0$, where $\lambda_p \approx 19$ μm.

5.3 Resonant Laser Wake-field Production in a Plasma Channel

After optimizing the channel characteristics for laser propagation, a simulation is performed using OSIRIS modeling the propagation of a 50 fs laser pulse with $a_0 = 3.0$ $mc\omega_L/e$ (LWF.1). This value of a_0 corresponds to 30 TW of power ($P_c \approx 10$ TW), inside a preformed channel for a distance of ~ 1 cm (~ 60 Z_R). The simulation box size used is 44 $c/\omega_p \times 44$ c/ω_p, corresponding to 136 μm$\times$136 μm. All scales and field quantities for the resonant wake-field and beat-wave simulations will be presented in normalized units with $c/\omega_p \approx 3$ μm for an on axis channel density of $n_0 = 3.0 \times 10^{18}$ cm^{-3}. This simulation demonstrated the production of a wake-field large enough to self-trap and accelerate electrons to highly relativistic velocities. In Figures 5.2(a) and 5.2(b), intensity plots of the longitudinal wake-field, E_z, and the transverse laser-field, E_x, are shown after the laser has propagated 2.7 mm. The same plots are presented after 7.5 mm of propagation in Figures 5.2(c) and 5.2(d). The large wake-field amplitudes produced in this simulation, peaking at 2.6 $mc\omega_p/e$ (4.5 GeV/cm) on axis (Figure 5.4), trap and accelerate background plasma electrons (the average accelerating gradient is ~ 0.8 GeV/cm over 1 cm). Slowing of the group velocity of the laser pulse causes the peak of the laser pulse to occur later in time which causes the
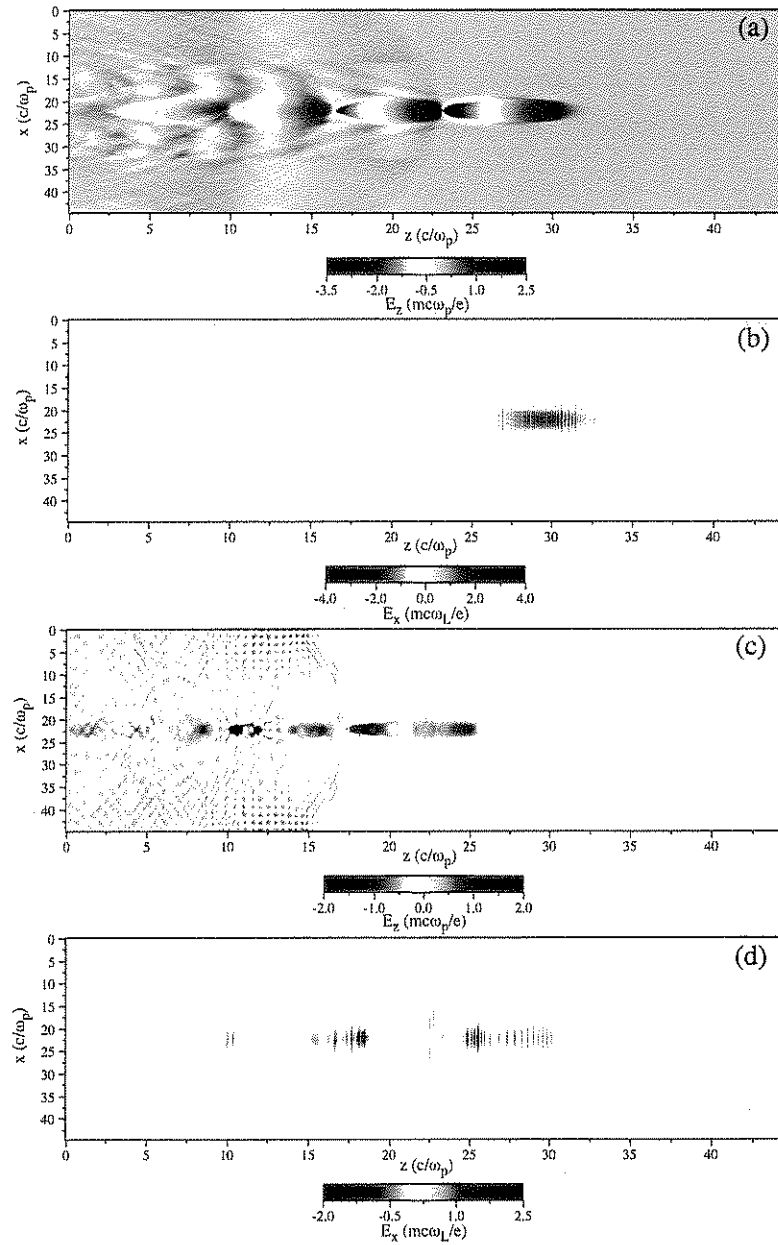
Figure 5.2: Plots of the wake-amplitude, E_z (a), and the laser-field amplitude, E_x (b), after 2.7 mm; and E_z (c) and E_x (d) after 7.5 mm (LWF.1).

wake also to be driven later as seen in Figures 5.2(c) and 5.2(d). The frequency spectrum of the 50 fs transform limited laser pulse, initially has a narrow peak at the laser frequency with $\Delta\omega/\omega_L \simeq 3\%$, and then broadens at the end of the simulation where $\Delta\omega/\omega_L > 50\%$. This is a manifestation of what is shown in Figure 5.2(d) in which the extensive break-up, phase modulation, and depletion of the laser-field is apparent and eventually, as a whole, limit the wake amplitude later in the simulation.

In Figure 5.3(a) and 5.3(b), phase space plots of the accelerated electrons give P_z versus position in the moving window after 7.5 mm and 11 mm of propagation inside the plasma channel. They show that initially the most energetic electrons are in one accelerating bucket at $\sim 23 \ c/\omega_p$, and then later a second bucket at ~ 19 c/ω_p has the most energetic electrons. Looking at the electron phase space with longitudinal momentum plotted versus the transverse coordinate x, a distinct beam can be seen at the center of the channel ($22c/\omega_p$) as shown in Figure 5.3(c). This illustrates the possibility of creating a well defined highly relativistic electron bunch by exciting large amplitude laser wake-fields in plasma channels. The background of high energy electrons outside of the channel is due in part to the periodic boundary condition of the simulation which allows particles reentering the system to still have a significant longitudinal momentum. By looking at the electron density in the simulation window it appears that the trapped electrons are originally at the walls of the channel and are then pushed into the center of the channel where they are accelerated. The number of trapped particles is relatively small when compared to the background plasma density; $\sim 0.01\%$ of the plasma electrons in the channel are trapped and accelerated.

Initially, the laser pulse amplitude goes through oscillations in the channel ($0 < z < 2$ mm) and then as the laser beam focuses the amplitude reaches a
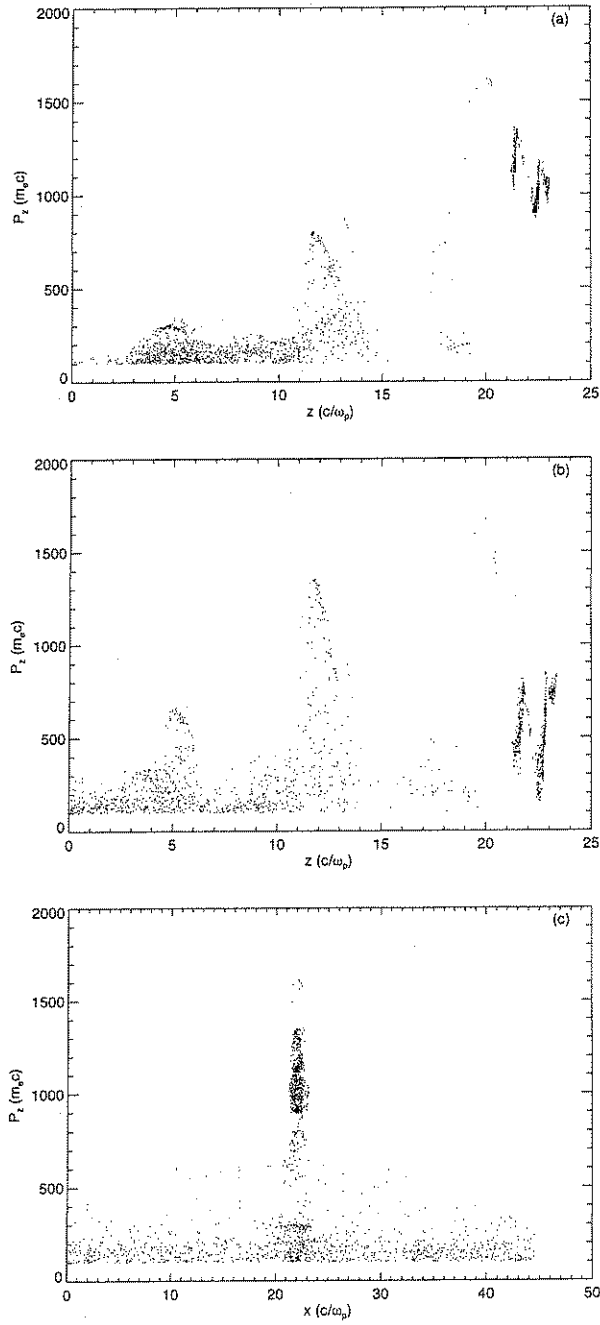
Figure 5.3: In (a) and (b) phase space plots or the resonant wake-field case at 7.5 mm and 11 mm of P_z versus z are shown, and in (c) there is a plot of P_z versus x after 7.5 mm (note that the channel width is $44c/\omega_p$).

110

peak value of $\sim 4.3 \; mc\omega_L/e$ ($z \approx 3.7$ mm) as shown in Figure 5.4(a). The period of these oscillations is approximately 400 μm which is equal to $2Z_R$. In Figure 5.4(b), the dashed curve gives the peak on axis wake amplitude, E_z, as a function of propagation distance. The two peaks in the plot of E_z reflect the two stage acceleration process produced in the simulation, where two different accelerating buckets reach a maximum at different times. Also plotted in Figure 5.4 is the peak longitudinal electron momentum, P_z, versus propagation distance (again the electron energy $E_e = mc^2(P_z - 1)$). After propagating 4 mm, and then again at 6 mm, the acceleration process is enhanced, as seen from the local maxima of E_z. Electron acceleration roughly to 800 MeV is achieved in this simulation after ~ 11 mm of propagation and is limited by depletion of the pump laser pulse which experiences extensive spatial break-up and phase modulation. This simulation shows that the laser pulse can be propagated much further than the Rayleigh length, approximately $60Z_R$, which is a distance on the order of the dephasing length, $L_{deph} = \lambda_p^3/\lambda^2 \approx 11$ mm [7]. This simulation shows that a net energy gain of ~ 1 GeV could potentially be achieved using LWF acceleration.

5.4 Beat-Wave Excitation of a Wake-Field in a Plasma Channel

It may be possible to achieve similar levels of acceleration as those achieved in the resonant wake-field case above with less intense, longer pulses through beat-wave excitation of plasma waves. In the following simulation (BW.1), the same channel profile is used to guide an intense, two-frequency laser pulse with the same initial spot size, w_0, of ~ 7 μm. A two frequency laser pulse with $\omega_{1,2} = \omega_L \pm \Delta\omega$ is used with a frequency separation, $\Delta\omega$, that corresponds to the same plasma frequency, ω_p, as for the resonant laser wake-field case ($n_0 = 3.0 \times 10^{18}$

Figure 5.4: In (a) the normalized laser vector potential as a function of propagation distance is plotted and in (b) the wake-amplitude E_z and the maximum P_z versus propagation distance are presented.

cm^{-3}). The laser pulse used in the simulation has a 360 fs rise-time, a 900 fs fall-time, and an $a_0 = 1.0$ $mc\omega_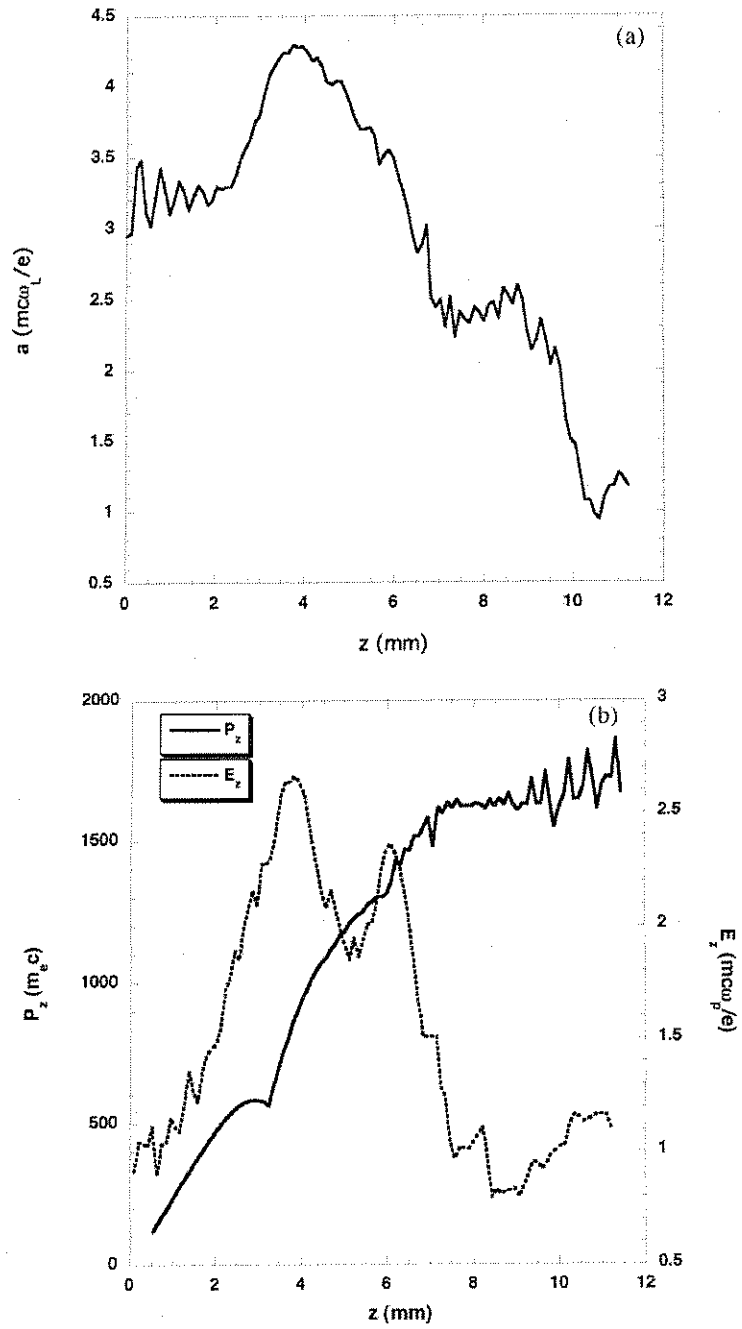L/e$ for each laser line. Images of the wake-field E_z along with the corresponding laser-field amplitude E_x normalized to $mc\omega_L/e$ after 0.5 mm of propagation are shown in Figures 5.5(a) and 5.5(b). The images of the wake-field and laser-field in Figures 5.5(c) and 5.5(d) illustrate the break-up and hosing of the laser beam inside the plasma channel [38], which are two of the limiting factors in the acceleration process. It is also clear that there is significant beam loading on the wake-field caused by the large number of self-trapped particles. The longitudinal positions where the number of electrons are largest correspond to where the wake-field, E_z, is smallest. The beam loading of the wake is especially apparent in the simulation window between ~$30c/\omega_p$ and $55c/\omega_p$.

The plasma electron phase space plots in Figures 5.6(a) and 5.6(b) show accelerated electrons after the laser has propagated 0.5 mm and 1.7 mm inside the plasma channel. The electrons are visible in each accelerating bucket, separated by $\Delta z = \lambda_p$, and demonstrate that most of the wake-field buckets participate in the acceleration process. The group velocity dispersion observed in the resonant wake-field case is also observed in this simulation, and as the laser and wake-field move backward in the simulation window more electrons are trapped between the initial positions of the accelerating buckets. The peak value of P_z for an electron in this simulation is ~$200mc$ (Figure 5.6(b) at $z \approx 350c/\omega_p$), which corresponds to an energy of approximately 100 MeV. The corresponding accelerating gradient is approximately 0.6 GeV/cm in this case, comparable to the gradient obtained in the previous case. Approximately 3% of the simulation electrons inside the channel are trapped and accelerated, a significantly larger percentage than in the resonant wake-field case. The wake amplitude at the end of the simulation is less than 50% of the cold wave-breaking amplitude $mc\omega_p/e$

113
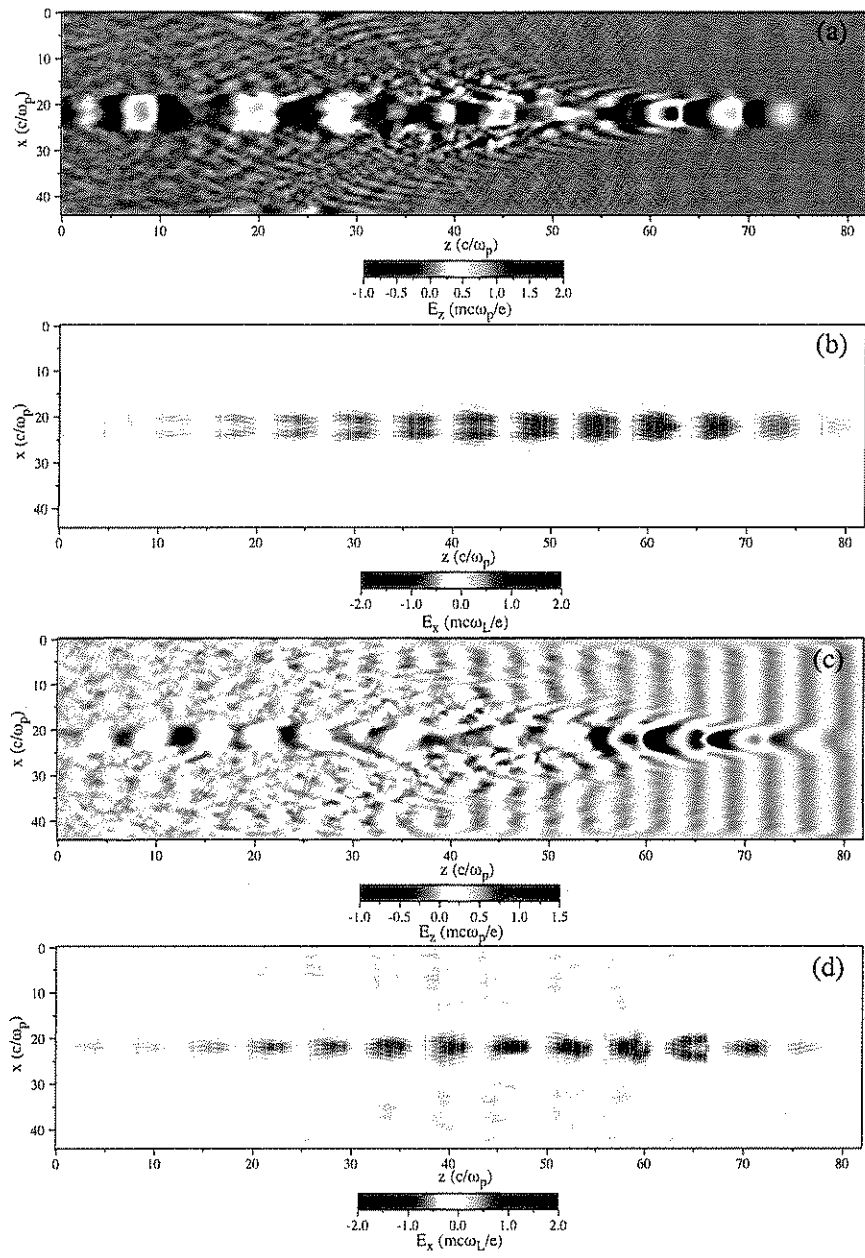
Figure 5.5: E_z (a) and E_x (b) after 0.5 mm with E_z (c) and E_x (d) after 1.7 mm for a beat-wave driven plasma wave in a channel (BW.1).
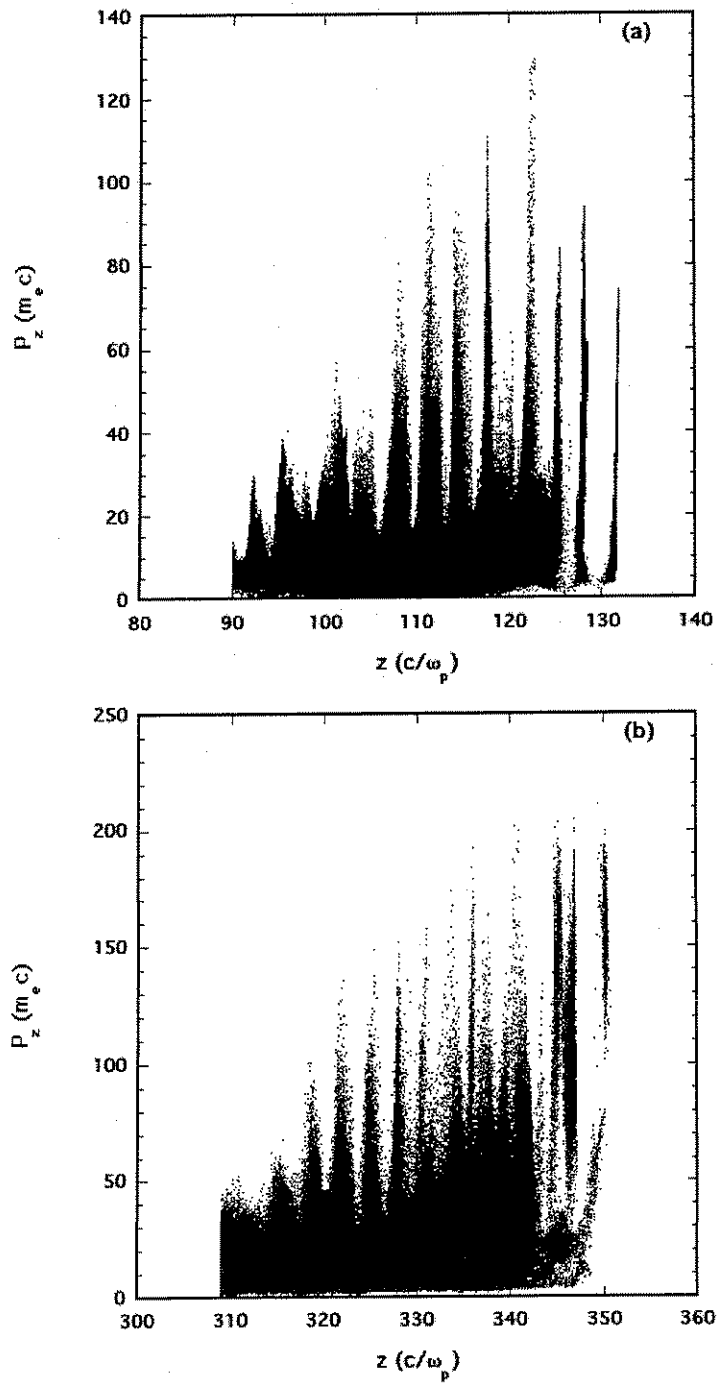
Figure 5.6: Phase space plot at (a) 0.5 mm and (b) 1.7 mm of propagation (BW.1).
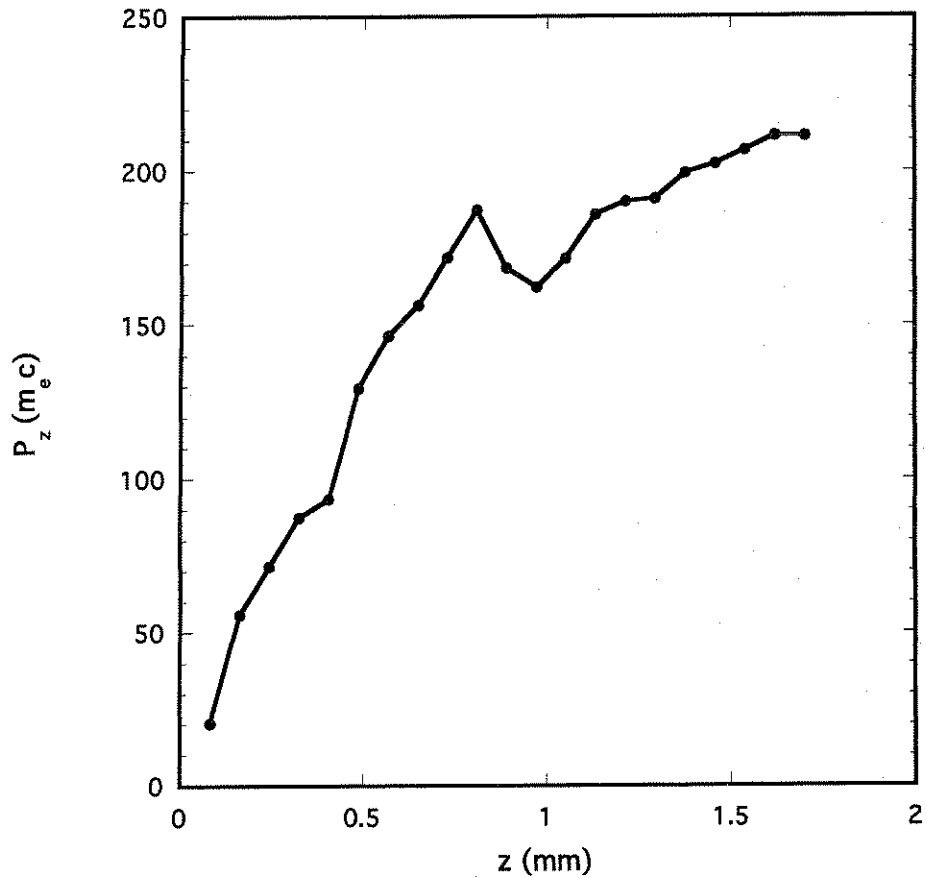
Figure 5.7: Plot of the maximum P_z versus propagation distance for the BW.1 simulation.

and decreases monotonically as the laser propagates through the channel. The decrease in the wake-amplitude can be attributed to depletion of the pump laser, and is reflected in the saturation of the energy gain in Figure 5.7. Although the final energy gain that the electrons achieve is not as large as in the resonant wake-field case, a smaller laser intensity and a longer laser pulse length can be used with a similar accelerating gradient. Increasing the length of the channel in this simulation would not have increased the energy gain significantly, as evidenced by the plot in Figure 5.7.

116

5.5 Wake-field Production through Raman Forward Scattering of a Laser Pulse in a Plasma Channel

The last acceleration scheme discussed in this chapter utilizes a much larger plasma density than those discussed above. To excite large amplitude waves through the Raman forward scattering instability it is desirable to have a plasma density considerably higher than for the resonant wake-field case. A large amplitude SMLWF is simulated for a 0.8 μm wavelength laser and for a laser beam with the same spot size as used above ($w_0 \approx 7\mu$m and $a_0 = 2.0mc\omega_L/e$). To modulate the 160 fs laser pulse that is used into as many as 6 periods requires a plasma density of $\sim 5 \times 10^{18}$ cm^{-3} corresponding to $\pi\omega_p^{-1} \approx 25$ fs. In Figure 5.8, a plot of wake-field, E_z, and laser-field, E_x, after 2.6 mm and 5.2 mm of propagation are presented with $c/\omega_p \approx 2.4$ μm for $n_0 = 5 \times 10^{18}$ cm^{-3}. A well defined longitudinal wake-field is not produced until the laser has propagated ~ 5 mm into the channel.

The phase space plots for this simulation (SMLWF.1), given in Figure 5.9, illustrate that the number of trapped electrons is not as large as in the BW.1 case, but is comparable to the LWF.1 simulation. Although the percentage of trapped particles is also $\sim 0.01\%$, since the density is higher, the overall number of trapped particles is larger (~ 5000). After 6.5 mm of propagation (Figure 5.9(a)), there are only three buckets that have trapped and accelerated electrons, and after ~ 9 mm (Figure 5.9(b)) the most energetic electrons reach ~ 1200 mc. Figure 5.10 gives the peak value of P_z versus z and shows that after ~ 9 mm the acceleration stops and the particles are decelerated. The average accelerating gradient is ~ 0.67 GeV/m for a 9 mm distance, slightly higher than the BW.1 simulation. The laser-field after 9.0 mm of propagation is nearly depleted and does not drive a large amplitude wake-field. The phase modulation and slowing

117
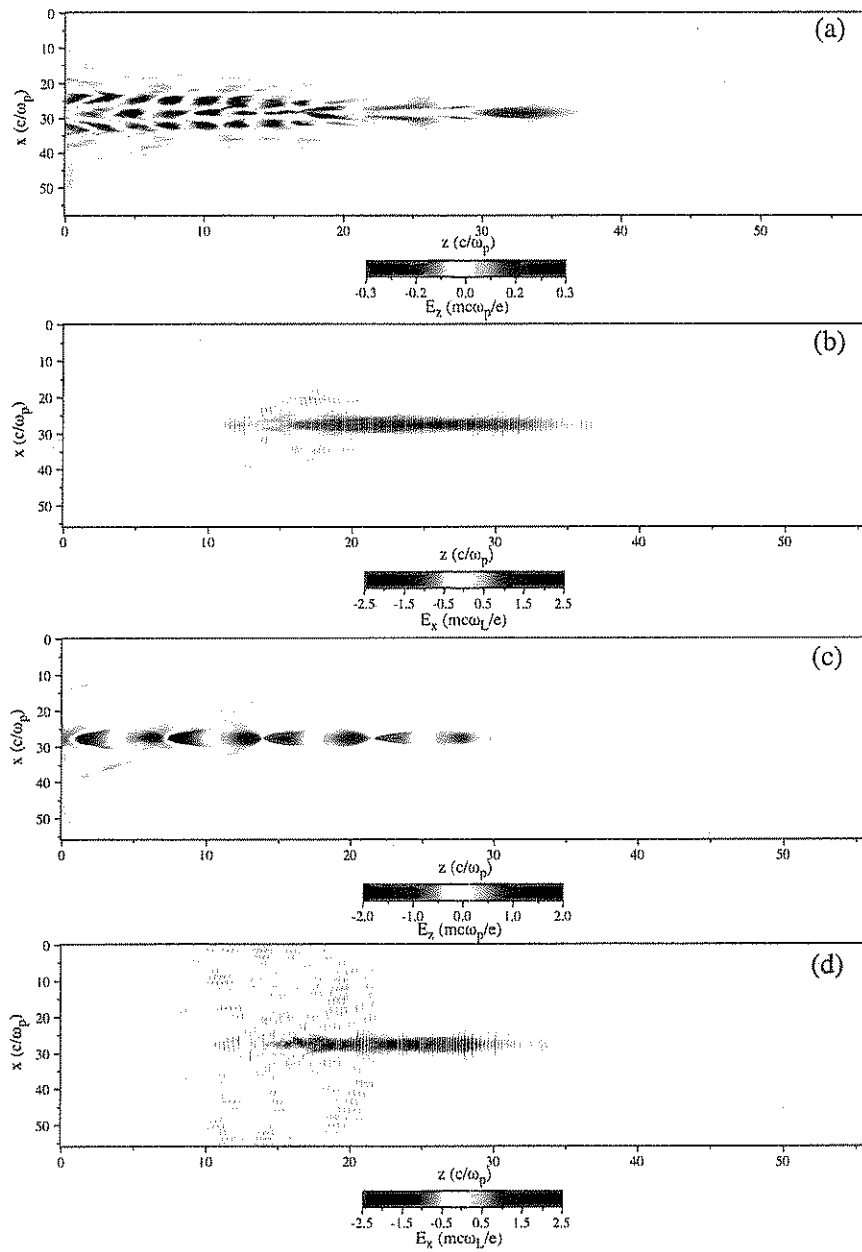
Figure 5.8: Plots of the wake-amplitude, E_z (a), and the laser-field amplitude, E_x (b), after 2.6 mm with E_z (c) and E_x (d) after 5.2 mm (SMLWF.1).
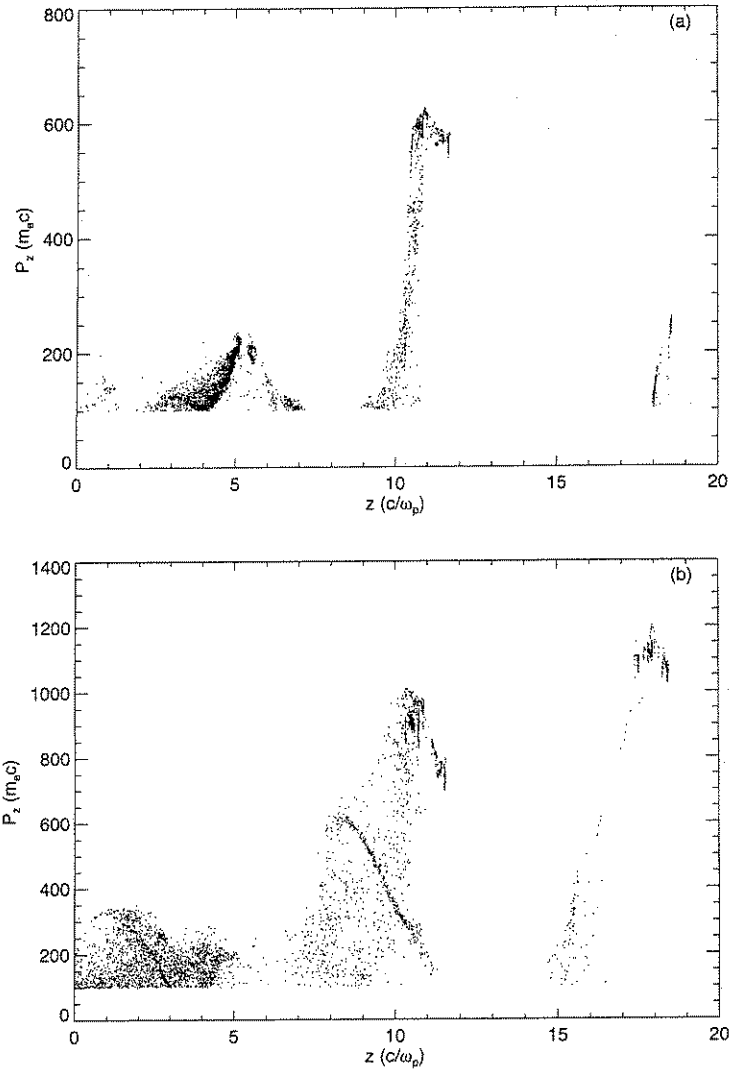
Figure 5.9: Phase space plot at 6.5 mm (a) and 9.0 mm (b) of propagation (SMLWF.1).
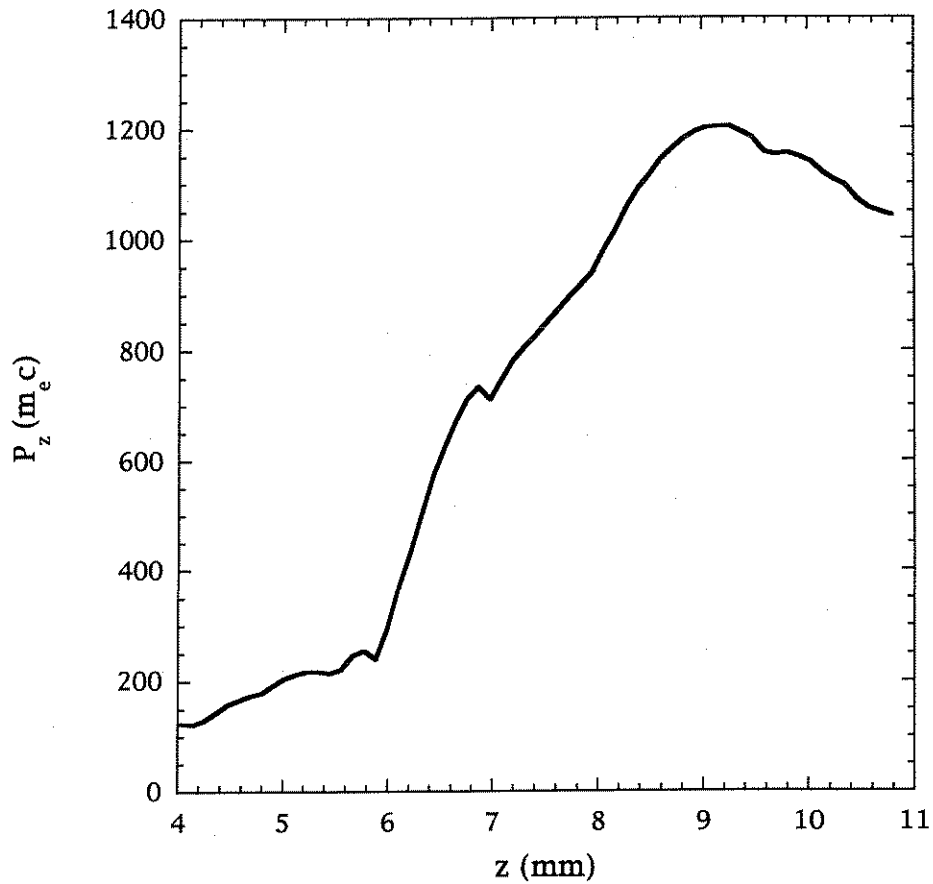
Figure 5.10: Plot of the maximum P_z versus propagation distance (SMLWF.1).

of the group velocity of the laser pulse, observed in the previous simulations, also occurs in this case. In this simulation, the process of electron acceleration begins more slowly than the other two cases and occurs mainly after $\sim$4 mm of propagation. This is attributable to the time/distance necessary for the growth of the Raman scattering instability, which now has to grow from noise [31].

5.6 Conclusions on Femtosecond Laser Pulse Guiding for Electron Acceleration

Experiments in the resonant wake-field, beat-wave, or self-modulated regimes can be performed using the laser pulse lengths and intensities utilized in the simulations presented here since all are attainable by current T^3 laser technology. From the simulation results, it is clear that all three acceleration schemes show promise of achieving electron energies in the 100 MeV–1 GeV range within $\sim$1 cm of propagation. The average accelerating gradients achieved in the simulations are on the order of 0.8 GeV/cm for the resonant wake-field case, 0.6 GeV/cm for the beat-wave simulation, and for the SMLWF case, an average gradient of 0.67 GeV/cm is obtained. In all of the simulations presented here, group velocity dispersion and distortion of the laser pulse envelope are the key features of the acceleration process in a plasma channel that eventually limit the acceleration. The simulation results show that although the largest energy gain is achieved for the LWF.1 case, a comparable accelerating gradient is achieved in both the BW and SMLWF simulations. For both the BW and SMLWF cases the laser intensity and pulse length requirements are not as difficult to achieve, but the overall results of were not as good as for LWF case. For both BW and SMLWF acceleration, the laser pulse length is of great importance in determining the optimum driving conditions for a wake-field and requires further study.

CHAPTER 6

Conclusions

In this thesis, the experimental work leading to the acceleration of relativistic electrons from an energy of $\sim$12 MeV to $\sim$50 MeV, using the plasma beat-wave acceleration technique, has been described. The $\sim$1 TW, two-frequency CO_2 laser system, needed to perform the experiments described here, was developed from scratch in the Neptune Laboratory. The plasmas utilized in the experiment were produced through tunneling ionization of hydrogen gas at pressures corresponding to densities for resonant driving of relativistic plasma waves. Two different focusing geometries were utilized for this purpose, one with an f/2 focusing optic, and the other with an f/18 focusing optic. For the f/2 focusing geometry, using the Thomson scattering diagnostic, a resonant density of $\sim$25% above the nominal value of 9.4×10^{15} cm^{-3} (corresponding to $\Delta\omega = \omega_2 - \omega_1 = \omega_p$) was determined. The resonant density for the acceleration experiments using the f/18 focusing geometery was determined in simulations and experiments to be $\sim$10 % above the nominal value of the resonant density.

Using the f/2 focusing geometry a laser spot size, w_0, of $\sim$50 μm and a laser intensity of $\sim$10^{15} W/cm^2 could be achieved at the interaction point. This focusing geometry had a limited interaction region due to the relatively short Rayleigh range, $2Z_R \approx$1.6 mm. Although the setup with an f/2 focusing optic excited large amplitude plasma waves, which were detected using the Thomson scattering diagnostic, no acceleration of the externally injected electron beam

was observed. This can be partly attributed to the large transverse electric fields produced in the plasma accelerating structure, and was demonstrated by the transverse deflection of the injected electron beam by the plasma wave. The setup using the f/18 focusing geometry was able to produce a laser spot size and intensity of $\sim$50 μm and $\sim$4$\times$10^{14} W/cm^2, respectively. The plasma accelerating structure for this setup was approximately 2.5 cm in length, considerably longer than for the f/2 case. Using this focusing geometry and $\sim$400 ps FWHM laser pulses, electrons were accelerated out to $\sim$50 MeV corresponding to a net energy gain of $\sim$38 MeV. This is the largest energy gain ever recorded using a beat-wave accelerating structure. These experimental results also correlate well the simulation results.

Particle-in-cell (PIC) simulations were performed in 2-D to model the experiment using the code TurboWAVE. The simulation results were in qualitative and quantitative agreement with the features observed in the experiment. The simulations performed for the f/2 focusing geometry showed that the transverse electric fields caused large transverse motion of plasma electrons and ions, which disrupted the plasma wave. Although the longitudinal electric field in the simulation, E_z, reached a peak amplitude of $\sim$0.4 $mc\omega_p/e$, the transverse field amplitude was $\sim$0.2 $mc\omega_p/e$ at the laser focus. These simulations provided a better understanding of the experimental issues that hindered the electron acceleration process. The simulations for the f/18 focusing geometry demonstrated that the transverse fields were approximately 10 times smaller than those for the f/2 case. The simulations also showed an upstream shift of the plasma generated through tunneling ionization for the f/18 case, something that was also observed in the experiment. This shift was caused by ionization induced refraction and limited the effective length of the plasma accelerating structure for a $\sim$120 ps laser pulse. However, by using a longer $\sim$400 ps laser pulse, transverse ion motion led the for-

mation of a plasma channel with a minimum density on axis. This plasma channel then allowed self-guiding of the laser beam and compensated for the refraction induced by ionization. This lengthening of the plasma allowed for a longer effective interaction length (product of the accelerating electric field and the length) between the injected electrons and the plasma wave; this effect allowed for the acceleration of injected electrons to $\sim$50 MeV. The injection of electrons into the accelerating structure was also modeled in the simulation and the results were in good agreement with the experiment. The simulations predicted the same accelerating gradient of $\sim$1.3 GeV/m, that was deduced from the experimental results, assuming an acceleration length of 2.5 cm.

2-D simulations were also carried out to model three laser acceleration schemes using shorter ($\sim$50–500 fs), more intense ($>5\times10^{18}$ W/cm^2), 0.8 μm laser pulses guided in preformed plasma channels. The simulations were performed using the PIC code OSIRIS, as well as TurboWAVE. The laser wake-field acceleration, plasma beat-wave acceleration, and self-modulated laser wake-field acceleration schemes were studied. The simulation parameters were optimized to produce the largest amplitude wake-field for the laser wake-field case, and a resonant density was determined for a $\sim$50 fs FWHM laser pulse to be $\sim$3$\times10^{18}$ cm^{-3}. The results presented demonstrated the guiding of the laser beam and acceleration of self-trapped plasma electrons over a distance of $\sim$11 mm, with a final peak electron energy of $\sim$800 MeV. The extensive phase modulation and slowing of the group velocity of the laser pulse eventually limited the acceleration.

The simulation presented for beat-wave acceleration scheme modeled the guiding of a laser pulse with a 360 fs rise-time and 900 fs fall-time, and a frequency separation corresponding to a density of $\sim$3$\times10^{18}$ cm^{-3}. This simulation also showed the acceleration of self-trapped particles, but only out to an energy of

~100 MeV in ~1.7 mm. This simulation trapped a significant portion of the background plasma electrons, and it was the resulting beam loading effects on the plasma wave that limited the acceleration process.

The simulation results for self-modulated laser wake-field case was for a ~160 fs laser pulse at a density of $\sim 5 \times 10^{18}$ cm^{-3}. This simulation guided the laser beam, but the acceleration process was slower than in the other two cases possibly due to the time necessary for growth of the forward Raman scattering instability. The peak electron energy achieved was ~600 MeV over a distance of ~9 mm. In all three schemes, depletion of the laser pulse, caused by phase modulation of the laser pulse and group velocity dispersion, played a role in limiting the final energy gain. Nonetheless, these results hold promise for the acceleration of electrons to GeV levels in future experiments, through the excitation of large amplitude plasma waves by guiding intense femtosecond laser pulses in preformed plasma channels.

APPENDIX A

Details on Electron Detection

A.1 Electron Spectrometer Setup

In this appendix information about the electron spectrometer diagnostic and the surface barrier detector setup is presented along with a brief description of the data acquisition setup. The silicon surface barrier detectors (SBDs) utilized are 1 mm thick and through deposition of a portion electron energy within the semiconductor produce a change in the voltage that is amplified and measured to determine the number of electrons that pass through the detector. The value of dE/dx for silicon is $\sim$0.3 KeV/μm for energies >1 MeV, so to produce the highest signal level it is necessary to use a thick detector. The sensitivity of the SBD detection system is dependent on the type of preamplifier used with the detectors. The two types utilized were the EG&G 142A and the EG&G 113 preamplifiers, both set with a voltage bias of approximately -300 V. The signals produced by these detectors were read by oscilloscope channels or channels on a transient recorder. The detector setup using these two preamplifiers is drawn in Figures A.1 and A.2 (not drawn are 75 μm aluminum foil used to filter stray visible light).

The phosphor screens at the IP were used to observe both acceleration of electrons near E_0 as well as any transverse effects on the electron beam. The setup involved using a 12-bit Photometrics Star1 CCD camera that measured the
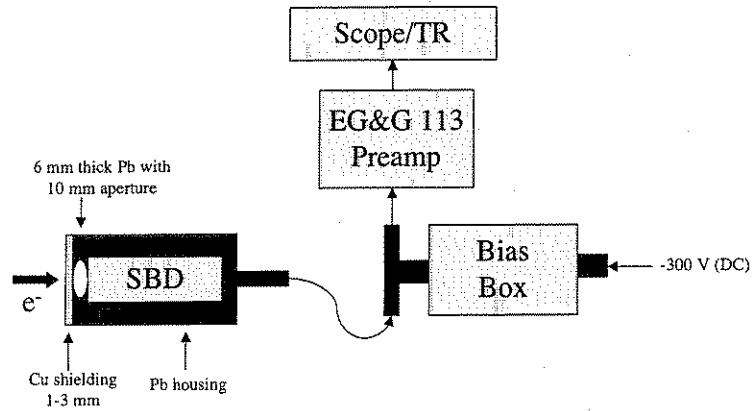
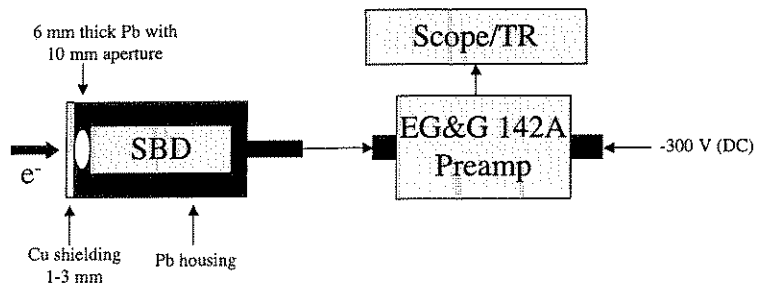Figure A.1: SBD setup using the EG&G 113 preamplifier.

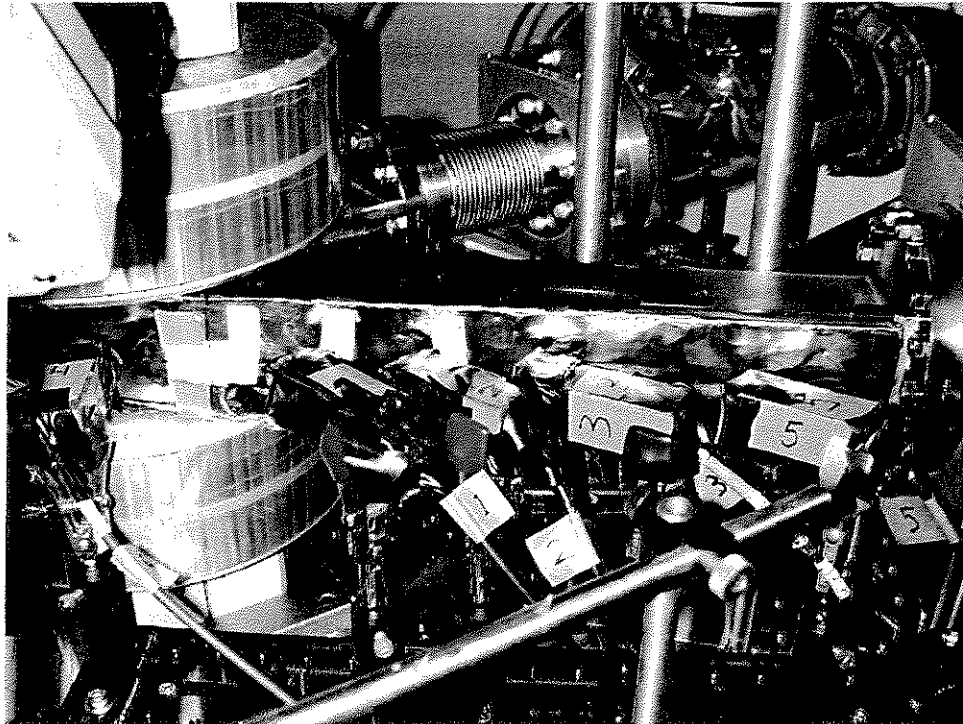Figure A.2: SBD setup using the EG&G 142A preamplifier.

Figure A.3: SBD setup for f/2 focusing geometry (see Figure 3.4).

fluorescence produced by electrons passing through two different phosphors at the exit plane of the electron spectrometer. Figure A.3 is a photograph of the electron spectrometer setup for the f/2 focusing geometry. The main electron beam at E_0 exits the spectrometer near the dashed line which is on a piece of Mylar$^{\text{TM}}$coated with fluorescent paint, and the accelerated electrons then go through a more sensitive TRIMAX phosphor made of Gd_2O_2S:Tb. This allowed visualization of both the main electron beam with a very high charge and the relatively low charge present in the accelerated spectrum. The photograph in Figure A.4 is a top view of a similar setup that illustrates the relative detector positions around the electron spectrometer for the experiments for the f/18 focusing geometry (the Star1 CCD is visible near the left corner of the photograph).
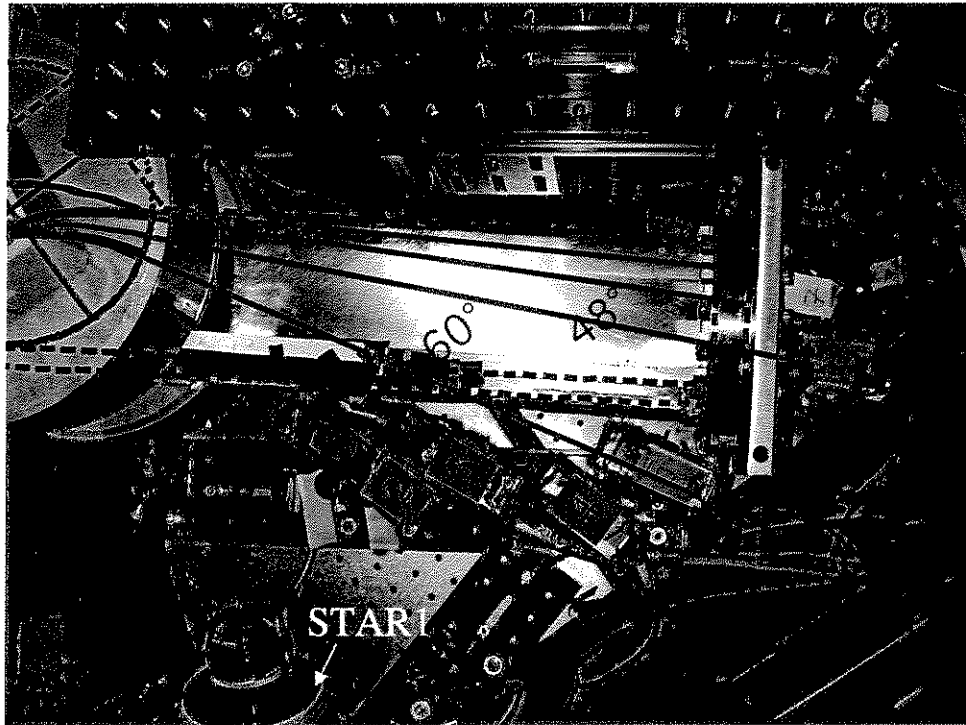
Figure A.4: SBD setup for f/18 focusing geometry.

A.2   Distinguishing X-ray noise from electron signals

It is important to note that the copper filters used did not decrease the level of signal produced by high energy electrons, but served as a very effective filter for low energy X-rays. Figure A.5 illustrates that for the low energy X-ray photons produced in the experiment, from 0.004–0.1 MeV, there is a finite probability of detection in the SBD. For X-ray photon energies greater than 0.1 MeV the probability of detecting the X-rays approaches zero. Figure A.6 shows that by using copper filters to shield the detectors, the X-rays flux is greatly attenuated below 0.1 MeV. The amount of energy deposited by any high energy X-ray photons is extremely small since dE/dx in silicon for X-ray photons with those energies is $\sim$.004 keV/μm ($\ll$0.3 KeV/μm for electrons). Figure A.7 shows the transmission of electrons versus electron energy in copper, for the different thicknesses used in the experiment. The effect of the copper on the electrons above $\sim$12 MeV is negligible. All of the transmission data is calculated using tables available from a NIST (National Institute of Standards) table which gives values of μ_{en}/ρ at different energies for copper and other materials. Here μ_{en}/ρ is the mass energy-absorption coefficient coefficient with units of cm^2/g. The transmission of a material with density ρ and thickness x is given by: $I/I_0 = \exp(-\mu_{en}/\rho \cdot \rho \cdot x)$.
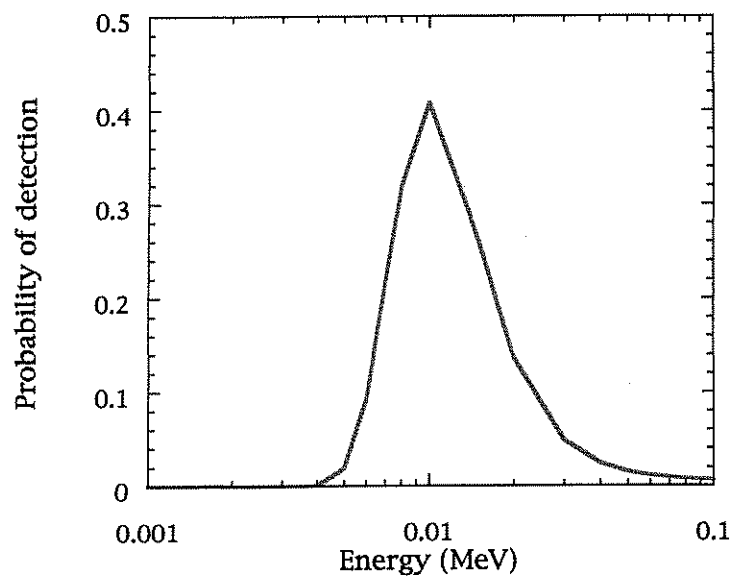
Figure A.5: A plot of the detection probability of X-rays through a 150 μm depletion layer of silicon as a function of X-ray photon energy.
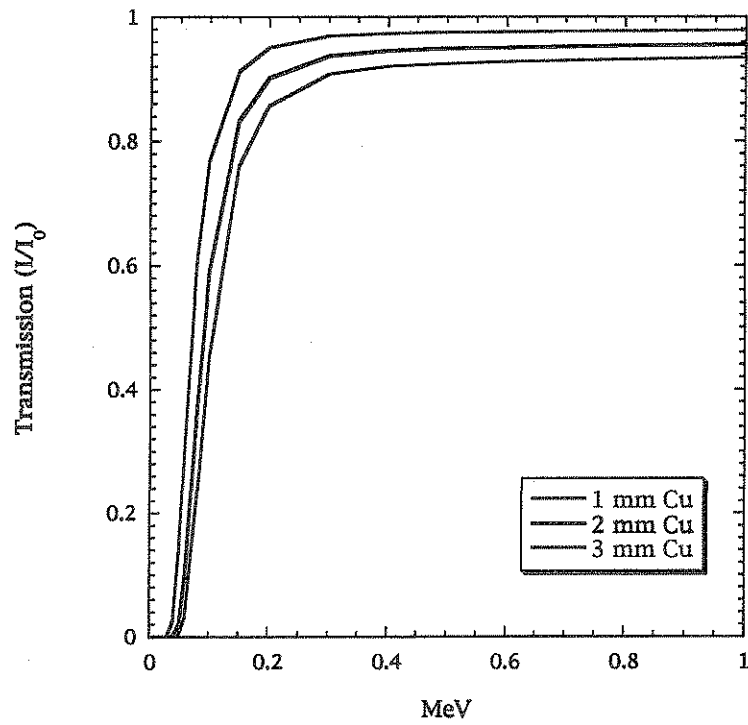
Figure A.6: A plot of the transmission of X-rays through 1–3 mm thick copper as a function of X-ray photon energy.
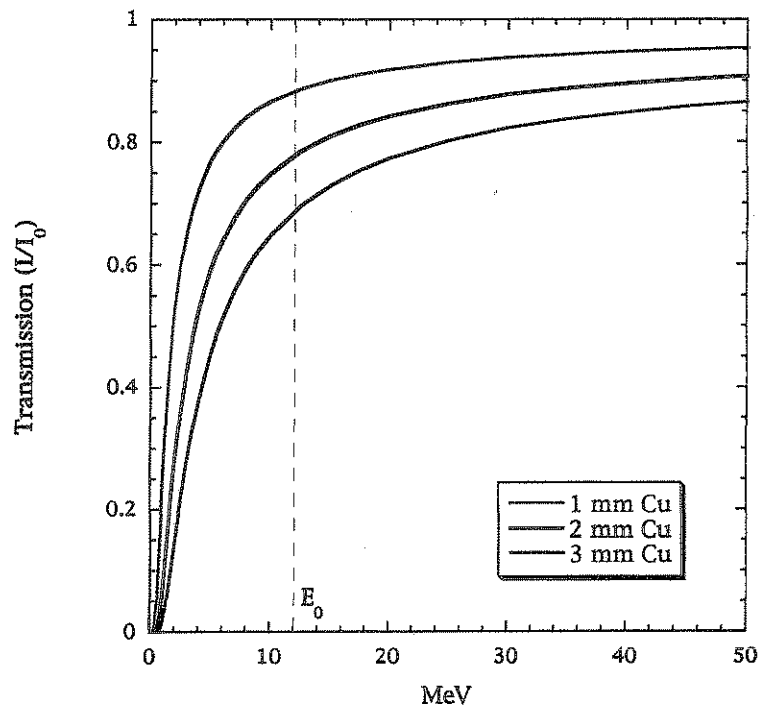
Figure A.7: A plot of the transmission of electrons through 1–3 mm thick copper as a function of electron energy.

REFERENCES

[1] T. Tajima and J. M. Dawson. Laser Electron Accelerator. *Phys. Rev. Lett.*, 43:267–270, 1979.

[2] C. E. Clayton, K. A. Marsh, A. Dyson, M. Everett, A. Lal, W. P. Leemans, R. Williams, and C. Joshi. Ultrahigh-Gradient Acceleration of Injected Electrons by Laser-Excited Relativistic Plasma Waves. *Phys. Rev. Lett.*, 70:37–40, 1993.

[3] P. Sprangle, E. Esarey, J. Krall, and F. Joyce. Propagation and Guiding of Intense Laser Pulses in Plasmas. *Phys. Rev. Lett.*, 69:2200–2203, 1992.

[4] D. F. Gordon, W. B. Mori, and T. M. Antonsen, Jr. A Ponderomotive Guiding Center Particle-in-Cell Code for Efficient Modeling of Laser-Plasma Interactions. *IEEE Trans. on Plasma Sci.*, 28:1135–1143, 2000.

[5] A. K. Lal. *Spatial and Temporal Dynamics of Relativistic Plasma Beat Waves*. Ph.D. Thesis, UCLA, 1996.

[6] F. F. Chen. *Introduction to Plasma Physics and Controlled Fusion*. Plenum Press, New York, New York, 1984.

[7] S. V. Bulanov, I. N. Inovenkov, V. I. Kirsanov, N. M. Naumova, and A. S. Sakharov. Nonlinear depletion of ultrashort and relativistically strong laser pulses in an underdense plasma. *Phys. Fluids B*, 4:1935–1942, 1992.

[8] Rosenbluth and Liu. Excitation of plasma waves by two laser beams. *Phys. Rev. Lett.*, 29:701–705, 1972.

[9] L. V. Keldysh. Ionization in the Field of a Strong Electromagnetic Wave. *Soviet Phys. JETP*, 20:1307–1314, 1965.

[10] W. P. Leemans. *Topics in High Intensity Laser-Plasma Interactions*. Ph.D. Thesis, UCLA, 1991.

[11] L.D. Landau and E.M. Lifshitz. *Quantum Mechanics*. (Pergamon, New York), 2nd edition, 1965.

[12] M. J. Everett. *The Physics of Beat Excited Plasmas*. Ph.D. Thesis, UCLA, 1994.

[13] Y. Kitagawa, T. Matsumoto, T. Minamihata, K. Sawai, K. Matsuo, K. Mima, K. Nishihara, H. Azechi, K. A. Tanaka, H. Takabe, and S. Nakai.

Beat-wave excitation of plasma wave and observation of accelerated electrons. *Phys. Rev. Lett.*, 68:48–51, 1992.

[14] F. Amiranoff, D. Bernard, B. Cros, F. Jacquet, G. Matthieussent, P. Mine, P. Mora, J. Morillo, F. Moulin, A. E. Specka, and C. Stenz. Electron acceleration in Nd-laser plasma beat-wave experiments. *Phys. Rev. Lett.*, 74:5200–5203, 1995.

[15] S. Ya. Tochitsky, R. Narang, C. V. Filip, C. E. Clayton, K. A. Marsh, and C. Joshi. Generation of 160-ps terawatt-power CO_2 laser pulses. *Opt. Lett.*, 94:262, 1999.

[16] C. M. Tang, P. Sprangle, and R. N. Sudan. Dynamics of space-charge waves in the laser beat wave accelerator. *Phys. of Fluids*, 28:1974–1983, 1985.

[17] E. S. Dodd. *Laser-Plasma Interactions Used for the Acceleration of Electrons.* Ph.D. Thesis, University of Michigan, 1999.

[18] R. Narang. *Production of Picosecond Two-wavelength CO_2 Laser Pulses using Semiconductor Switching.* M.S. Thesis, UCLA, 1998.

[19] C. V. Filip. *Regenerative Amplification and Injection Mode-Locking of Picosecond Two-wavelength CO_2 Laser Pulses.* M.S. Thesis, UCLA, 1999.

[20] S. Ya. Tochitsky, C. V. Filip, R. Narang, C. E. Clayton, K. A. Marsh, and C. Joshi. Efficient shortening of self-chirped picosecond pulses in a high-power CO_2 amplifier. *Opt. Lett.*, 26:813–815, 2001.

[21] S. Augst, D. Strickland, D. D. Meyerhofer, S. L. Chin, and J. H. Eberly. Tunneling Ionization of Noble Gases in a High-Intensity Laser Field. *Phys. Rev. Lett.*, 63:2212–2215, 1989.

[22] R. Narang, C. V. Filip, S. Ya. Tochitsky, D. Gordon, C. E. Clayton, K. A. Marsh, and C. Joshi. Characteristics of plasmas produced by double beat wave interaction in the Neptune facility at UCLA. *Proceedings of the 2001 Particle Accelerator Conference*, 2001.

[23] C. V. Filip. *Resonant and Non-resonant Beat-wave Excitation of Relativistic Plasma Waves.* Ph.D. Thesis, UCLA, 2003.

[24] S. G. Anderson, M. Loh, P. Musumeci, J. B. Rosenzweig, H. Suk, and M. C. Thompson. Commissioning and Measurements of the Neptune Photoinjector. *Advanced Accelerator Concepts: Ninth Workshop*, pages 487–499, 2001.

[25] T. W. Johnston and J. M. Dawson. Correct values for high-frequency power absorption by inverse bremsstrahlung in plasmas. *Phys. Fluids.*, 16:722, 1973.

[26] C. E. Clayton, K. A. Marsh, C. Joshi, C. B. Darrow, A. E. Dangor, A. Modena, Z. Najmudin, and V. Malka. A Broadband Electron Spectrometer and Electron Detectors for Laser Accelerator Experiments. *Proc. of the 1995 Part. Accel. Conf.*, pages 637–639, 1995.

[27] A. Septier. *Applied Charged Particle Optics.* Chapter 4.2: Deflecting Magnets, by H. A. Enge, Academic Press, New York, 1983.

[28] C. E. Clayton, C. Joshi, and J. Rosenzwieg K. A. Marsh, C. Pellegrini. Second generation beatwave experiments at UCLA. *Nuclear Inst. & Meth. in Phys. Res. A*, 410:378–387, 1998.

[29] M. V. Ammosov, N. B. Delone, and V. P. Krainov. Tunnel ionization of complex atoms and of atomic ions in an alternating electromagnetic field. *Sov. Phys. JETP*, 64:1191–1194, 1986.

[30] K-C. Tzeng and W. B. Mori. Suppression of electron ponderomotive blowout and relativistic self-focusing by the occurrence of Raman scattering and plasma heating. *Phys. Rev. Lett.*, 81:104–107, 1998.

[31] C. D. Decker, W. B. Mori, T. C. Katsouleas, and D. E. Hinkel. Spatial temporal theory of Raman forward scattering. *Physics of Plasmas*, 3:1360–1372, 1996.

[32] R. Fedele, U. de Angelis, and T. C. Katsouleas. Generation of radial fields in the beat-wave accelerator for Gaussian pump profiles. *Phys. Rev. A*, 33:4412–4414, 1986.

[33] C. D. Decker, W. B. Mori, K-C. Tzeng, and T. C. Katsouleas. Modeling single-frequency laser-plasma acceleration using particle-in-cell simulations: the physics of beam breakup. *IEEE Trans. on Plasma Sci.*, 24:379–392, 1996.

[34] J. Fuchs, G. Malka, J. C. Adam, F. Amiranoff, S. D. Baton, N. Blanchot, A. Héron, G. Laval, J. L. Miquel, P. Mora, H. Pépin, and C. Rousseaux. Dynamics of Subpicosecond Relativistic Laser Pulse Self-Channeling in an Underdense Preformed Plasma. *Phys. Rev. Lett.*, 80:1658–1661, 1998.

[35] E. Esarey, P. Sprangle, J. Krall, and A. Ting. Self-Focusing and Guiding of Short Laser Pulses in Ionizing Gases and Plasmas. *IEEE J. of Quantum Electron.*, 33:1879–1914, 1997.

[36] R. G. Hemker, F. S. Tsung, V. K. Decyk, W. B. Mori, S. Lee, and T. Katsouleas. Development of a parallel code for modeling plasma based accelerators. *Proc. of the 1999 Part. Accel. Conf.*, 5:3672–3674, 1999.

[37] Y.R. Shen. *The Principles of Nonlinear Optics*. John Wiley & Sons, Inc., 1984.

[38] C. Ren and W. B. Mori. Physical Picture for the laser hosing instability in a plasma. *Physics of Plasmas*, 8:3118–3119, 2001.